AN ABSTRACT OF THE DISSERTATION OF

Maoyu Wang for the degree of Doctor of Philosophy in Chemical Engineering presented on December 03, 2021.

Title: Design Principles of Transition Metal X-ide Catalysts for Electrochemical Oxygen Reduction and Evolution Reactions: *In-Situ* X-ray Spectroscopy Studies

Abstract approved: ____

Zhenxing Feng

Hydrogen is the green fuel that can be produced from water through electrolysis and used via hydrogen fuel cells to generate electricity with zero carbon dioxide emission. The commercialization of electrolyzers and fuel cells is the critical step to achieving global carbon neutrality. However, it is severely hampered by the low efficiency in associated reactions, particularly the oxygen evolution reaction (OER) and the oxygen reduction reaction (ORR) for the two devices, respectively. Highly efficient electrocatalysts are required to overcome the slow kinetics in the two reactions, but the state-of-the-art electrocatalysts are mostly based on noble metal or noble metal oxides such as Pt, IrO_2, and RuO_2. Therefore, many efforts have been devoted to finding cost-effective and highly active electrocatalysts for ORR and OER. The two most efficient methods are either maximizing noble metal's activity (e.g., single atom catalysts) or replacing noble metal with low-cost transition metals. This Ph.D. thesis is focused on electrocatalysts containing transition metals, so-called transition metal X-ides (X = C, N, O, S, Se, etc.). Besides the electrochemical characterization of catalysts' activity, selectivity and stability, we apply synchrotron X-ray absorption spectroscopy (XAS) at hard X-ray (incident X-ray energy

higher than 5 keV) and soft X-ray (incident X-ray energy lower than 2 keV) regions to study the electrocatalysts' chemical properties (oxidization state, electronic structure, and local structure), particularly *in-situ*/*operando* XAS to characterize the chemical properties change under the catalytic reaction conditions. Those findings revealed the structure-property and catalytic performance relationship.

Two kinds of materials were chosen as the representative catalysts to build a systematic study. Perovskite $LaCoO_3$, one of the transition metal oxides with moderate stability, has shown the approximate ORR and OER performance compared with standards. It was found that the electron number at the e_g orbital can be the characteristic parameter to determine theactivity of this type of electrocatalyst. To verify and extend the theory, we substituted Co with Fe in $LaCoO_3$ to tune the electronic structure, and subsequently changed not only the ORR activity but also selectivity. The soft XAS pointed out the metal-oxygen bonding hybridization and 3d transition metal electron distribution could further influence the catalytic performance in addition to metal d-band e_g theory. Later, the $LaCoO_3$ with co-substituted Fe and P was studied to confirm that the metal-oxygen bonding hybridization and electronic structure in the octahedral units would also influence the OER catalytic activity. In addition, the combination of hard and soft XAS further pointed out the hybridization between oxygen p-band and 3d transition metal e_g orbit could be more critical than the general metal-oxygen hybridization for OER performance. The second material Co_9S_8, a representative material of transition metal X-ides that are unstable in reaction and experience restructuring throughout the reaction, has shown better OER performance than benchmark RuO_2. The combination of *operando* hard XAS, *operando* Raman spectroscopy, and density of function theory suggested that the Co_9S_8 would completely restructure to form edge-sharing octahedral CoO_6 units during OER, which is the truly active phase. The edge-sharing

octahedral is hypothesized as the active center for restructuring-induced electrocatalysts, which was further verified by atomically dispersed Ir catalysts anchored on amorphous CoO for OER. The electronic structure of these catalyst materials can be altered to achieve the best OER activity by varying the composition of edge-sharing octahedral units. Through our comprehensive studies, we provide new approaches to develop high-performance ORR and OER electrocatalysts for accelerating the development of renewable energy systems.

Design Principles of Transition Metal X-ide Catalysts for Electrochemical Oxygen Reduction and Evolution Reactions: *In-Situ* X-ray Spectroscopy Studies

by
Maoyu Wang

A DISSERTATION

submitted to

Oregon State University

in partial fulfillment of
the requirements for the
degree of

Doctor of Philosophy

Presented December 03, 2021
Commencement June 2022

Doctor of Philosophy dissertation of Maoyu Wang presented on December 03, 2021

APPROVED:

Major Professor, representing Chemical Engineering

Head of the School of Chemical, Biological, and Environmental Engineering

Dean of the Graduate School

I understand that my dissertation will become part of the permanent collection of Oregon State University libraries. My signature below authorizes release of my dissertation to any reader upon request.

Maoyu Wang, Author

ACKNOWLEDGEMENTS

I would like to express my sincere gratitude to my advisor Prof. Zhenxing Feng. He supports my Ph.D. research by teaching me research and writing skills and sets an excellent example of diligence, serious research attitude, and non-stop learning. Without his training, advice, and encouragement, I would not make significant progress throughout my Ph.D. studies.

I would like to express my appreciation to Dr. Binghong Han, who taught me electrochemical characterization skills. I would like to thank Dr. Qing Ma, Dr. George E. Sterbinsky, Dr. Alpha T N'Diaye for their help on the XAS measurements and explanations. I would like to express my sincere appreciation to all my collaborators for their help and support.

I would like to express my sincere appreciation to my committee members, Prof. Líney Árnadóttir, Prof. Chih-hung Chang, Prof. Gregory S. Herman, and Prof. Liu Hong. Thank you for being my committee members and for great suggestions for my research.

I would like to thank everyone in the Feng's group, particularly Brian Allen Muhich, who helps me a lot with electrochemical measurements. Members in Feng group are always available to discuss my research and help me deal with difficult situations.

I would like to thank my mother Jirong Gao, my father Rongqing Wang, and my wife Liwei Zhang for supporting me and encouraging me. I would also like to thank my roommates Fei Long, Jun Yang and Yan Wang to help overcome some hard time especially during COVID pandemic period.

This work was financially supported by Oregon State University and National Science Foundation (CBET-2016192, CBET-1949870, and ECC-2025489). The soft X-ray absorption spectroscopy was performed at Advanced Light Source, which is an Office of Science User

Facility operated for the U.S. DOE Office of Science by Lawrence Berkeley National Laboratory and supported by the DOE under Contract No. DEAC02-05CH11231. The synchrotron X-ray characterization is supported by the National Science Foundation (CBET-1949870 and DMR-1832803). The hard XAS measurements were done at Advanced Photon Source (APS) of Argonne National Laboratory (ANL) for synchrotron measurements is supported by Department of Energy under Contract No. DE-AC02-06CH11357.

CONTRIBUTION OF AUTHORS

The work presented in this dissertation could not have been achieved without the help of many great scientists. Prof. Zhenxing Feng advised me in all the materials synthesis, data analysis, result interpretation, writing and editing the manuscripts.

In chapter 3, Dr. Binghong Han guided me on how to run electrochemical measurements and analyze those measured data. Dr. Junjing Deng helps me with the X-ray imaging measurements. Yan Wang helps me with the XRD measurements and explanation. Marcos Lucero, Dr. Yubo Chen and Dr. Zhenzhen Yang helps me with the XPS measurements and analysis. Dr. Alpha T N'Diaye helps me with the soft XAS measurements. Prof. Zhichuan J. Xu provides contributions towards experimental design and interpretation of results.

In chapter 4, Brian Allen Muhich helps me with the electrochemical measurements. Dr. George E. Sterbinsky helps me with the operando XAS measurements. Kingsley Chukwuma Chukwu and Prof. Líney Árnadóttir provides guide in performing and explaining DFT calculations.

In chapter 5, Qingbo Wa and Prof. Xinwei Wang helps me with the materials synthesis, electrochemical tests and operando Raman measurements. Dr. Xiaowan Bai and Prof. Yuanyue Liu performs the DFT calculation based on our predicted model. Dr. Qing Ma and Dr. Hua Zhou helps me with the operando XAS measurements.

In chapter 6, Dr. Chao Cai and Prof. Meng Gu contributed to experiment design materials synthesis, electrochemical tests, and image (TEM and SEM) measurements. Dr. George E. Sterbinsky helps me with the operando XAS measurements.

TABLE OF CONTENTS

TABLE OF CONTENTS （Continued）

Page

TABLE OF CONTENTS (Continued)

LIST OF FIGURES

LIST OF FIGURES (Continued)

LIST OF FIGURES (Continued)

LIST OF FIGURES (Continued)

LIST OF FIGURES (Continued)

LIST OF TABLES

LIST OF TABLES (Continued)

Chapter 1. Introduction

In recent decades, the total carbon dioxide (CO_2) emission has kept increasing, leading to serious environmental problems.[1-3] The majority emission of CO_2 is from the combustion of fossil fuels, which has a limited amount.[4] The scarcity of fossil fuels and the terrible environmental situation drive the development of sustainable and green energy resources. Unlike fossil fuels, solar energy is inexhaustible. However, directly using solar energy has lower energy efficiency, which could not replace fossil fuel in our daily transportation. The energy conversion systems and energy storage systems based on the electrochemical reaction, which uses electricity generated from solar energy, have been considered promising solutions.[5-7] For example, the hydrogen-based fuel cell and metal-air batteries are the two most promised next-generation energy conversion systems, and the water electrolyzers are one credible energy conversion/storage system.[8-11] The oxygen-involved reactions, so-called oxygen reduction reaction (ORR) (Equation1.1), and oxygen evolution reaction (OER) (Equation 1.2), are the key-half electrocatalytic reaction involved in those three renewable energy systems.[10-12] Compared with another half-reaction (hydrogen oxidation and evolution reactions), both ORR and OER have low energy efficiency caused by the sluggish kinetics.[6, 13-16] That is why we need to investigate high catalytic active electrocatalyst. The traditional noble metal catalysts such as Pt, IrO_2, and RuO_2 show promised catalytic activity for ORR and OER. Still, the expensive noble metal hinders the commercialization of those energy systems.[17, 18] Hence, many efforts have been contributed to commercial-friendly and high catalytic active electrocatalyst.

Equation 1.1: $O_2 + 4\mathrm{H}^+ + 4\mathrm{e}^- \rightarrow 2\mathrm{H}_2O$

Equation 1.2: $2H_2O \rightarrow O_2 + 4\mathrm{H}^+ + 4\mathrm{e}^-$

Two methods to effectively solve those problems are either using low-cost transition metal (TM) to replace the noble metal or better utilizing the function of noble metals. For low-cost transition metal oxides, a wide range of materials such as high-entropy alloy, metal oxide, metal sulfide, nanoparticle, single atomic dispersed materials, and metal-organic framework have been applied to those electrochemical reactions.[19-22] For utilization of noble metal, the single atomic dispersed materials, high-entropy alloy, structure modified nanoparticle are some representative methods to increase the performance.[23, 24] Some materials already show reasonable performance in laboratory, and some hypotheses have been developed to explain the significant activity enhancement.[1, 23-25] However, there are still some mysteries to fully understand the truly active center in both ORR and OER and no consistent agreement on the characteristic parameters in determining catalysts' electrochemical properties. To perform mechanistic understanding, X-ray absorption spectroscopy (XAS) is a useful tool to investigate the change of oxidization state and local structure of materials, and *operando* experiments can provide time-resolved catalysts structural information. Therefore, we use both *ex-situ* and *in-situ/operando* XAS to observe the electrocatalyst reconstruction during the reaction to determine the real active site to provide deep insight for future material design.

In chapter 3, we designed a Fe substituted $LaCoO_3$ for ORR to tune the electronic structure of perovskite oxides. By using *ex-situ* XAS, we find that the modification of TM-oxygen (TMO) bonding hybridization and electronic structure of TM together can influence the ORR performance and even change the catalytic reaction pathway from 2 electron-transfer-reaction to 4 electron-transfer-reaction. In chapter 4, we further modified the Fe substituted $LaCoO_3$ by doping P to improve the OER performance. Combining *operando* XAS, X-ray diffraction (XRD), and density of function theory (DFT), we found that modification of TMO bonding hybridization could be critical to alternate the OER performance. In chapter 5, we focus the second type of electrocatalysts that are as stable as perovskite oxide in reaction. To further extend those theories into different TM compounds such as TM sulfide, we carried out *operando* Raman and XAS to study one of the representative materials named Co_9S_8. We found that the crystalline Co_9S_8 would restructure into CoO_x nanocluster during OER, which is the truly active site confirmed by DFT. The TMO bonding theory could be also applied to this case. Furthermore, we also explore whether our design principle for electrocatalysts could be applied in noble metals. In chapter 6, the Ir anchored CoO was designed for the study for utilization noble metal function. The Ir would form Ir-O-Co bonding, acting as an active center for OER, which shows excellent performance.

Chapter 2. X-ray Absorption Spectroscopy

2.1. Fundamentals of X-ray Absorption Spectroscopy

X-ray absorption spectroscopy (XAS) is a well-established analytical technique used for characterizing all kinds of chemicals in solid or liquid, crystalline or amorphous, bulk or nanoscale even single atom form.[26-28] It is widely used to analysis the electronic structure, local geometric structure, and oxidization state of detect materials.

When X-ray passing through a material, the intensity will be attenuated (Figure 2.1a). According to Beer's law, this attenuation can be characterized by the absorption coefficient based on Equation 2.1,

Equation 2.1: $I_t=I_0e^{-\mu(E)t}$

where I_0 is the incident X-ray intensity, I_t is the transmitted X-ray intensity, t is the sample thickness, and $\mu(E)$ is the absorption coefficient that is dependent on the photon energy.[26, 27, 29] XAS measures the energy-dependent fine structure of the X-ray absorption coefficient.[27-31] When the incident X-ray energy is lower than the binding energy of the electron in the element's orbital (say, s-orbital), the electrons are not excited to unoccupied state or the vacuum, and X-ray is not strongly absorbed, thus creating a flat region in the spectrum, which is called the pre-edge, as shown in Figure 2.1b.[26-29] Once the X-ray energies are high enough to excite core electrons to the unoccupied state (Figure 2.1c), X-ray is strongly absorbed and it leads to a large jump in the spectrum, which is called the X-ray absorption near edge structure (XANES) (Figure 2.1b). This region is sensitive to the oxidization state and electronic structure of the detected elements as the core electron energy is affected by the electron distribution in the valence state.[26-29] With the further increase of X-ray energies, the core electrons excited to continuum state (Figure 2.1c) form the outgoing and scattering wave interference with neighboring atoms (Figure 2.1d). The construction or deconstruction interference of the outgoing and scattering wave will form the wiggles in the extended X-ray absorption fine structure (EXAFS) region (Figure 2.1b), which reflects local atomic structure such as bond distance and coordination number.[32-34]

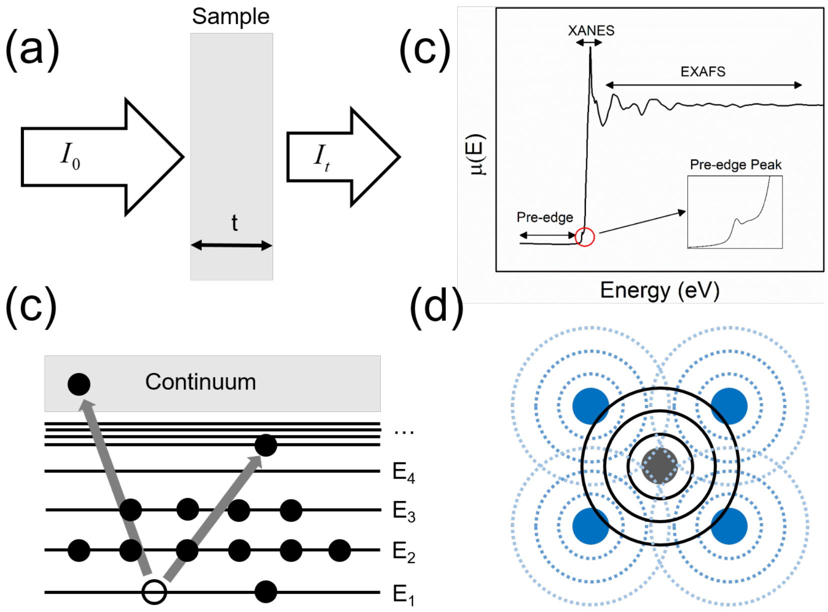

Figure 2.1 (a) schematic of incident and transmitted X-ray beam (b) schematic of XAS including the pre-edge, XANES and EXAFS regions (c) schematic of the X-ray absorption process and electron excited process, the black circle is electrons (d) schematic of interference pattern creating by the outgoing (solid black lines) and reflected (dashed blue lines) photoelectron waves between absorbing atom (grey) and its nearest atoms (purple)[35] Reprinted with permission from Ref. 35

2.2. Why choose *in-situ* operando XAS

There are three basic modes for XAS signal collections, namely transmission, fluorescence, and electron yield modes (Figure 2.2). Transmission mode measures the difference between incident and directly transmitted X-ray intensity (Figure 2.2a). Based on the Beer's law,[26-28] to enlarge the difference for high quality data, concentrated and homogenous samples are recommended. In contrast, fluorescence mode measures the emitted X-rays from the elements (Figure 2.2a). The intensity of this fluorescence is proportional to the absorption caused by the investigated element but could be affected by self-absorption effect. Thus, it is good for dilute and works for non-homogenous samples.[26-28] Instead of measuring the emitted fluorescence, we can also measure the emitted photoelectrons from sample itself. Because of the relative short mean free path of photoelectrons, this mode is surface sensitive,[26-28] while the two other modes are bulk sensitive. As XAS mainly probe the local structure, it can be used to measure many different materials including liquid and solid in either crystalline or amorphous structure, from bulk, nanoscale to even single atom.

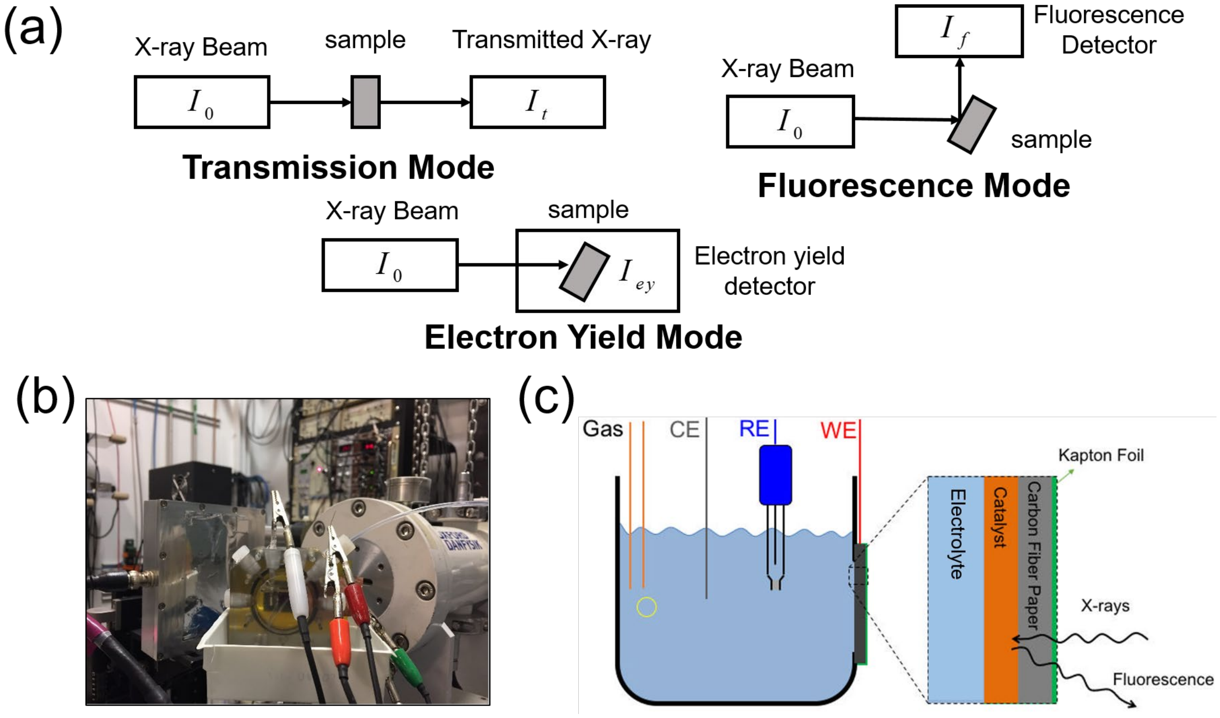

Figure 2.2 (a) Schematic of the experiment setup for three different XAS detection modes: transmission mode, fluorescence mode, and electron yield mode (b) Photo of the real electrochemical cell for in-situ XAS experiment setup[35] (c) Schematic structure of the electrochemical cell for in-situ XAS setup experiments[1] Reprinted with permission from Ref. 1 and 35

XAS requires synchrotron sources that can tune the X-ray energy easily. The fast development of synchrotron X-ray source (about 92 synchrotron sources around the world) have enabled the wide applications of XAS. Recently XAS can also be performed on the benchtop instrument, making it more accessible in the lab.[36, 37] In addition, the use of hard X-ray (energy higher than 5 keV) can be beneficial for *in-situ* measurements.[1, 38, 39] The advanced electrochemical cell design (Figure 2.2b, 2.2c) also simplifies the operation of *in-situ* XAS experiments. The well-designed cell has four necks used for the gas inlet, the gas outlet, the reference electrode, and the counter electrode. The gas inlet and outlet provides the possibility for gas involved reactions such as ORR and carbon dioxide reduction reaction (CO2RR). The front window is covered by the electrocatalyst as working electrode loaded on the carbon fiber paper, which is fixed by Kapton foil/tape to make sure no electrolyte leakage. Combined with the reference and counter electrode, it is built as a three-electrode reaction cell. Furthermore, around 10 ml liquid amount guarantees enough electrolyte for electrochemical reaction. However, the lab based-experiment is a little bit different from *in-situ* synchrotron experiment. In the lab, we used to apple linear sweep or cyclic voltammetry on the electrocatalyst by rotation disk electrode to characterize electrochemical performance, but those kinetics processes are hard to be detected by XAS to study the intermediate state. Hence, we applied a constant voltage or current on the reaction cell to achieve a thermodynamic steady-state, and XAS is carried out to measure the materials oxygen state and local structure under this state. Nowadays, the XAS is used not only to probe oxidization state and local structure but also to investigate nanocluster size, element site occupation in the crystal lattice, and atomic disperse molecular structure due to the well-developed XAS techniques and analysis software.

2.3. Conclusion

XAS is a unique characterization technique to understand materials oxidation state and local structure information. However, sometimes XAS cannot tell a lot useful information with other characterization. For example, XAS cannot distinguish the atoms with closet atomic numbers.

In addition, it is necessary to have well-defined standards to gain useful information from XAS, and sometimes the theoretical modeling is very helpful to analyze the XAS spectra for extracting useful electronic and atomic structure information. To conclude, XAS, particularly *in-situ* operando has become an important and useful tool to obtain oxidation state, electronic structure and local bonding environments, which are critical to investigate the electrocatalysts under the real reaction conditions.

Chapter 3. The Influence of Fe substitution into $LaCoO_3$-Electrocatalysts on Oxygen-Reduction Activity

The Influence of Fe substitution into $LaCoO_3$-Electrocatalysts on Oxygen-Reduction Activity

Maoyu Wang[a†], Binghong Han[b†], Junjing Deng[c], Yi Jiang[c], Mingyue Zhou[d], Marcos Lucero[a], Yan Wang[a], Yubo Chen[e], Zhenzhen Yang[b], Alpha T N'Diaye[f], Qing Wang[d], Zhichuan J. Xu[e], and Zhenxing Feng[a*]

[a] Department of Chemical, Biological and Environmental Engineering, Oregon State University, Corvallis, Oregon 97331, United States

[b] Chemical Sciences and Engineering Division, Argonne National Laboratory, Argonne, Illinois 60439, United States

[c] Advanced Photon Source, Argonne National Laboratory, Argonne, Illinois 60439, United States

[d] Department of Materials Science and Engineering, Faculty of Engineering, National University of Singapore, Singapore 117576, Singapore

[e] School of Materials Science and Engineering, Nanyang Technological University, Singapore 639798, Singapore

[f] Advanced Light Source, Lawrence Berkeley National Laboratory, Berkeley, California 94720, United States

†: Equally Contributed First Author

*: Corresponding Author

Reprinted with permission from ACS Appl. Mater. Interfaces, vol. 11, issue 6, pp. 5682-5686, 2019.

3.1. Abstract

The development of commercial-friendly and stable catalysts for oxygen reduction reaction (ORR) is critical for many energy conversion systems such as fuel cells and metal-air batteries. Many Co-based perovskite oxides such as $LaCoO_3$ have been discovered as the stable and active ORR catalysts, which can be good candidates to replace platinum (Pt). Although researchers have tried substituting various transition metals into the Co-based perovskite catalysts to improve the ORR performance, the influence of substitution on the ORR mechanism is rarely studied. In this paper, we explore the evolution of ORR mechanism after substituting Fe into $LaCoO_3$, using the combination of X-ray photoelectron spectroscopy, high-resolution X-ray microscopy, X-ray diffraction, surface-sensitive soft X-ray absorption spectroscopy characterization, and electrochemical tests. We observed enhanced catalytic activities and increased electron transfer numbers during the ORR in Co-rich perovskite, which are attributed to the optimized e_g filling numbers and the stronger hybridization of transition metal 3*d* and oxygen 2*p* bands. The discoveries in this paper provide deep insights into the ORR catalysis mechanism on metal oxides and new guidelines for the design of Pt-free ORR catalysts.

3.2. Introduction

Recent decades, the scarcity of fossil fuels and global warming drive the development in green and renewable energy resources. The energy conversion systems such as proton exchange membrane fuel cell (PEMFCs) and metal air batteries (MABs) have been considered as promising solutions.[15, 21, 40] However, the sluggish kinetics of oxygen reduction reaction (ORR) suspends the development of PEMFCs and MABs, and the traditional platinum-based ORR catalysts account for 20% of the total cost of commercial PEMFCs, which hampers the commercialization of those energy conversion systems.[41] Using transition-metal oxides, particularly the perovskite oxides, to catalyze ORR in alkaline solution provides an alternative commercial-friendly solution. Recently, many experimental and computational studies have been done to find the optimized perovskite oxides, such as $Ba_{0.5}Sr_{0.5}Co_{0.8}Fe_{0.2}O_{3-\delta}$,[41] to replace Pt-based ORR catalysts in alkaline media.[15, 42-44] Researchers have found that when the e_g filling number is close to 1, the perovskite oxides tend to have higher ORR activity, which provided guidelines to improve the ORR performance of perovskite catalysts by tuning their electronic structures.[15] However, the experimental determination of e_g filling number is nontrivial. Recently, substituting transition metals such as Fe into Co-based perovskites has been proved as an effective way to improve the ORR performance in alkaline electrolytes,[5, 15, 41]but the influence of metal substitutions in perovskite ORR catalysts on the evolution of electronic structures and ORR mechanisms still remains unclear.

In this work, we used Fe-substituted $LaCoO_3$ to systematically study the transition metal substitution effect on the electronic structures and its consequential influence on the ORR kinetics and catalysis mechanisms. A series of $LaCo_xFe_{1-x}O_3$ (x = 0, 0.4, 0.6, 1) was synthesized to tune the Co 3*d* band and Co (3*d*)-O (2*p*) hybridization, which were measured by the surface-sensitive soft X-ray absorption spectroscopy (XAS). We found the sluggish performance with Fe substitution can be attributed to the tuning of e_g orbit electron and transition Metal-Oxygen bond (M-O) covalency. Additionally, by using the rotation-speed dependent electrochemical tests, we analyzed the change of electron transfer numbers during ORR. Fe substitution caused more two-electron-transfer reaction that reduces O_2 to H_2O_2, compared with the four-electron-transfer reaction found on Co-rich surfaces that directly reduces O_2 to H_2O. The change of electron transfer number implies that the Fe substitution and the tuning of M-O covalency not only have large influence on the ORR kinetics, but also to the micro-kinetic reaction mechanisms.

3.3. Materials Characterization

The X-ray diffraction (XRD) patterns of $LaCo_xFe_{1-x}O_3$ are shown in Figure 3.1. The phase transition from rhombohedral perovskite to orthorhombic perovskite is clearly observed with more Fe doping. The $LaCoO_3$ and $LaFeO_3$ have pure rhombohedral and orthorhombic structures, respectively, compared with the reference patterns, while the $LaCo_{0.6}Fe_{0.4}O_3$ and $LaCo_{0.4}Fe_{0.6}O_3$ exhibit the mixed-phase structures. Such phase change after substitution is consistent with the previous report.[45] To examine the morphology and bulk composition, we chose simultaneous X-ray fluorescence and ptychographic measurements,[46, 47] as it is nondestructive, direct visualization with high resolution in composition and morphology, and can be applied for *in situ* measurements.[48] Figure 3.2 shows La, Co and Fe elemental maps of $LaCo_xFe_{1-x}O_3$ micro-particles with a spatial resolution of about 160 nm. The fluorescence results are mostly consistent with the percentage of stoichiometrically mixed La_2O_3, Fe_2O_3 and Co_3O_4 (see Table 3.3). The phase images of ptychographic reconstructions in Figure 3.2 show 2-dimensional projected electron density distribution of these particles with a significantly higher spatial resolution (~15 nm), which enables to reveal the internal structures within the particles. Our results suggest that all $LaCo_xFe_{1-x}O_3$ materials are synthesized in micron size with reasonable homogenous elemental distribution from surface to bulk. As far as we know, this is the first X-ray ptychorgraphy images for electrocatalysis applications. To quantify the surface area of $LaCo_xFe_{1-x}O_3$, the *Brunauer–Emmett–Teller* (BET) tests were carried out and the specific surface areas of these $LaCo_xFe_{1-x}O_3$ oxides are 0.18-0.57 m^2/g, as shown in Table 3.2, which are consistent with the µm-scale particle size observed in X-ray images. Since the reaction takes place on the surfaces of catalysts, the X-ray photoelectron spectroscopy (XPS) was used to confirm the surface stoichiometry, which is also closely correlated with the electrochemical performance. The XPS results in Table 3.1 show that the surface Co: Fe ratios of different samples are consistent with their bulk nomination Co: Fe ratios.

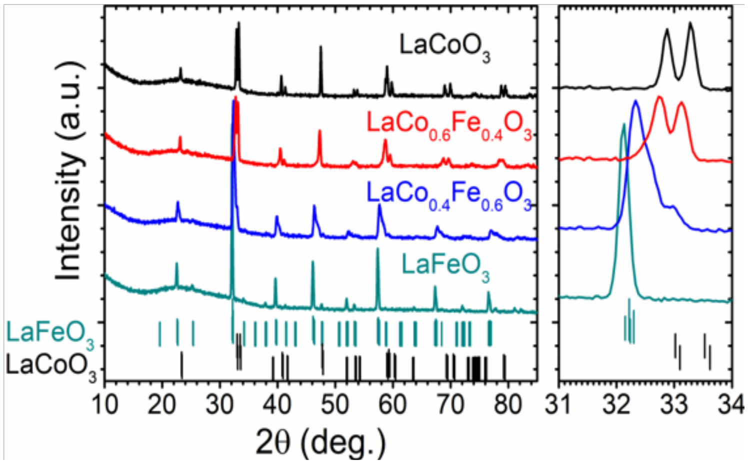

Figure 3.1 Powder X-ray diffraction patterns of $LaCo_xFe_{1-x}O_3$ (x=0, 0.4, 0.6, 1). The phase transitions from rhombohedral and orthorhombic structures with higher Fe substitution is observed in the zoom-in part.

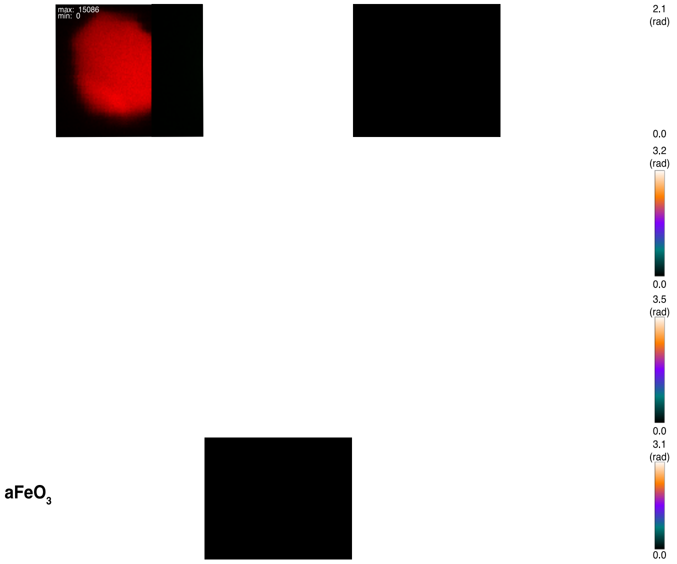

Figure 3.2 X-ray fluorescence and ptychographic images of $LaCo_xFe_{1-x}O_3$ (x=0, 0.4, 0.6, 1) particles to show the element distribution and morphology. The La L-edge, Co K-edge and Fe K-edge fluorescence were selectively monitored to obtain corresponding element distribution.

3.4. Electrochemical Performance

The ORR performance of $LaCo_xFe_{1-x}O_3$ was tested in 0.1M KOH solutions using the three-electrode rotating-disk method. The ORR currents of $LaCoO_3$ measured at different rotation speeds after background correction (see Figure 3.6) demonstrates the transportation limit (limiting current) has critical influence particularly under high ORR overpotentials. With the help of electron transfer number and Equation S3.3, which will be discussed in detail later, we can estimate the limiting current and therefore obtain the kinetic current $i_{kinetic}$ using Equation S3.2. The kinetic ORR currents density normalized by the BET surface areas of different $LaCo_xFe_{1-x}O_3$ are shown in Figures 3.3a and 3.3b,[49] where the IR correction has been employed to correct the voltage loss from Ohmic resistance. Both the polarization curves and Tafel plots show that the increase of Fe concentration caused the decrease of ORR catalytic activity. The overpotential increased by 46 mV at 2 mA/cm^2_{oxide} from $LaCoO_3$ to $LaFeO_3$ (Figure 3.3a). Despite the change in ORR activity, substituting Fe into $LaCoO_3$ did not cause obvious change in Tafel slopes, as shown in Figure 3.3b, demonstrating that the energy barriers of the rate-determine steps on different samples are similar during the ORR.

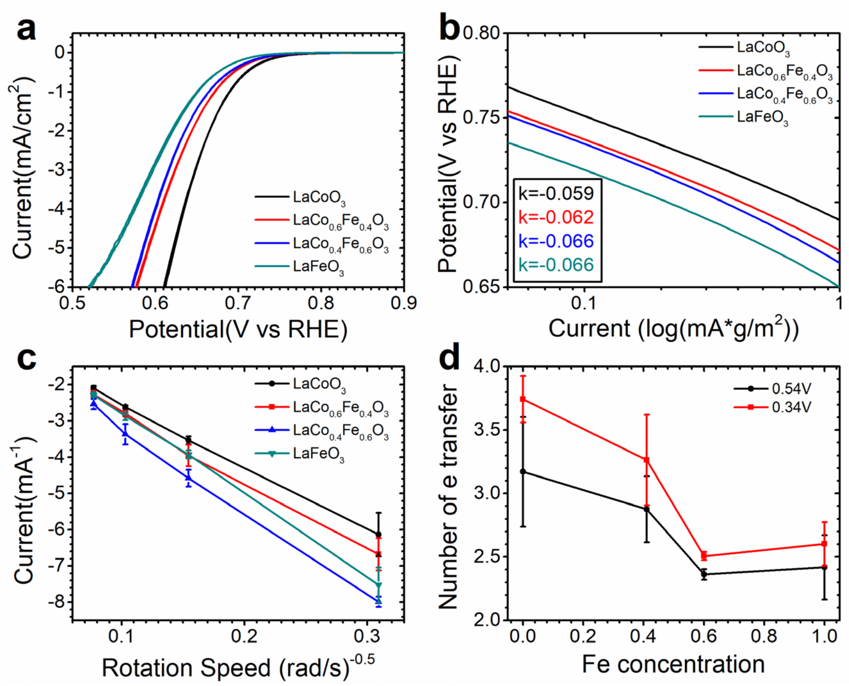

Figure 3.3 (a) Specific ORR activity of LaCo$_x$Fe$_{1-x}$O$_3$ (x= 0.0, 0.4, 0.6, 1) in O$_2$-saturated 0.1M KOH solutions at the rotation rate of 1600 rpm with the scan rate of 20 mV/s, where LaCoO$_3$ has the lowest overpotential. (b) ORR activity Tafel plots of LaCo$_x$Fe$_{1-x}$O$_3$ (x= 0.0, 0.4, 0.6, 1), using the same data shown in panel a. The insert box shows the Tafel slope of each material. (c) ORR current at 0.54 V vs. RHE corrected only by background subtraction as a function of rotation speeds (100, 400, 900, 1600 rpm) for the Koutecky-Levich equation. (d) Number of electron transfer determined by panel c and Figure 3.12 during ORR at 0.34 and 0.54 V vs. RHE against different Fe substitution levels. The number of electron transfer decreases with Fe doping. The data points represent the average values from at least three measurements for each sample, while the error bars represent the corresponding standard deviations.

In addition to the Tafel slope, the electron transfer number during ORR is also closely correlated with the ORR catalysis pathway. Figure 3c shows the ORR currents measured at 0.54 V vs. RHE under different rotation speeds on different samples, plotted against the inverse root of the rotation speed. Similar plot measured at 0.34 V vs. RHE is shown in Figure 3.7. The slope of these plots, according to the Koutecky-Levich equation, can be used to determine the number of electron transfer during ORR by comparing with that of pure Pt disk, which has 4 electron transfers for ORR catalysis. As shown in Figure 3.3d, from LaCoO$_3$ to LaFeO$_3$, the electron transfer number dropped from 3.17 to 2.42 at 0.54V vs. RHE, and dropped from 3.74 to 2.60 at 0.34 V vs. RHE.

The great decrease of electron transfer number after Fe substitution indicates the Fe site prefer 2-electron-transfer ORR mechanism that reduces O_2 to H_2O_2, while the Co site prefer 4-electron-transfer reaction that directly reduces O_2 to H_2O.[50] Although both 2- and 4-electron-transfer pathways can reduce O_2 to H_2O at the end, the 2-electron-transfer pathway is not desirable for fuel cell applications since the free peroxides formed during ORR can damage the separators and the catalysts.[50] Meanwhile, the Fc/Fc+ test shown in Figure 3.8 indicates that the different $LaCo_xFe_{1-x}O_3$ samples used in this paper have similarly good conductivity Therefore, the decreased electron transfer numbers and catalytic activities observed on Fe-rich samples are less likely due to the conductivity variation but more likely due to the electronic structure evolutions, which can influence the bidentate and end-on O_2 adsorption type on the catalyst surface and therefore affect different electron transfer pathway.[21]

3.5. Electronic Structure Characterizations

In this study, we used surface-sensitive characterization techniques, including the XPS and the electron yield mode of soft XAS, to examine the oxidization state and surface electronic structures of $LaCo_xFe_{1-x}O_3$ with different Fe substitution levels. As demonstrated in our previous studies,[1, 25] XAS is an element-specific technique that can provide information related to both electronic and atomic structure, and quite powerful for *in situ* characterizations. XAS measurements on the Co L-edge (Figure 3.4a) show an intermediate spin state in $LaCo_xFe_{1-x}O_3$ with e_g=1, which is close to the optimized e_g filling number of perovskites for ORR catalysis.[15, 51, 52] In contrary, the Fe L-edge results in Figure 3.4b illustrates a high spin state with e_g=2, which, according to previous e_g descriptor studies, corresponds to much lower ORR activity.[53] Therefore, enhancing the Fe doping level will increase the average number of e_g orbital electrons and diverge the electronic structure from the optimized value around 1 (also see supporting information for details). This finding is consistent with the suppressed electrochemical performance after Fe substitution observed in Figure 3.3a. In addition, a small peak around 783 eV can be observed in the Co L-edge of $LaCo_{0.4}Fe_{0.6}O_3$ (see Figure 3.4a), indicating that when the Fe substitution level is too high, the surface Co trends to partially assume the low spin state, which also increases the average e_g filling number.[52] Here the change of e_g filling number can explain the slower ORR kinetics after substituting Co with Fe. However, no previous e_g orbital theory can be used to explain the different reaction pathways with different electron transfer numbers observed on various $LaCo_xFe_{1-x}O_3$ samples in Figure 3.3d. Actually, most of the previous mechanism studies on the ORR electron transfer numbers focused on the oxygen species adsorbed on the catalyst surface during ORR. One study proposed that the nature of the adsorption of oxygen species on metal oxides, which is related to the interaction between oxygen π orbitals and metal d_z^2 orbitals, could be different between Fe-based oxides and Co-based oxides, since Fe has filled d_z^2 (Pauling model) while Co has empty d_z^2 (Griffths or Bridge model).[5] The difference of oxygen-metal interactions on the surface may influence the final electron transfer number during ORR. In addition to oxygen-metal interactions, the surface oxidization status of transition metal sites may also be a descriptor for the ORR performance and electron transfer numbers. By comparing with Fe and Co XPS (Figure 3.10), we observed no change in Co and Fe oxidization states after Fe doping, meaning Fe substitution will not influence the oxidization states of Co and Fe on the surface, implying a weak interaction between Co and Fe. Therefore, Co prefers the 4-eletron pathway, and Fe prefers the 2-electron pathway.

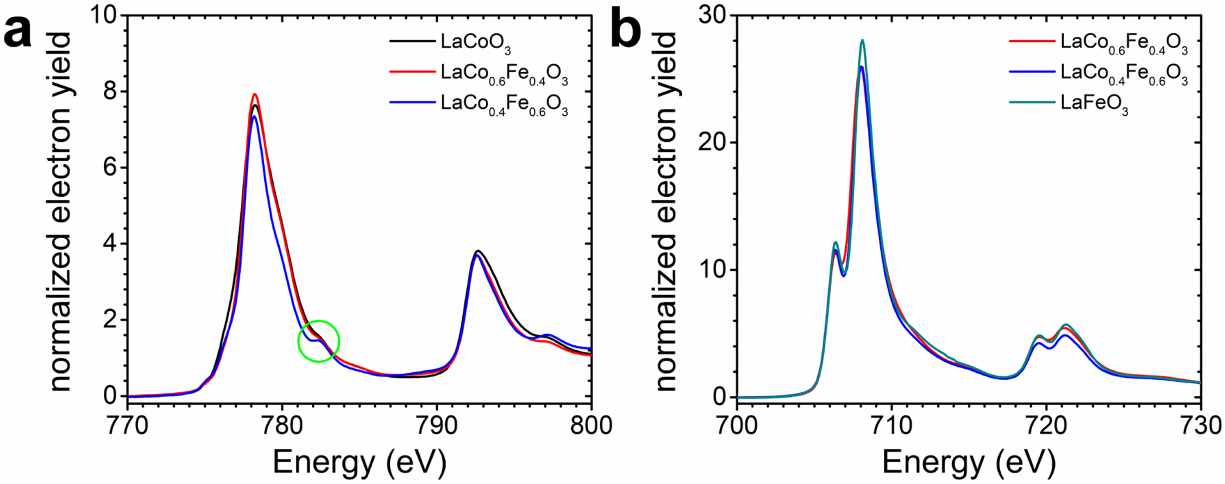

Figure 3.4 Surface-sensitive soft XAS electron yield mode data of (a) Co L-edge and (b) Fe L-edge represents the change of transition metal 3d spin state after the Fe substitution into $LaCoO_3$.

In addition to the investigation of metal oxidation states using metal L-edge results to explain the change of electron transfer numbers on different metal sites, we further applied XAS (Figure 3.5) and XPS (Figure 3.9) on the oxygen K-edge to quantify the role of M-O covalency in ORR mechanisms. Figure 5 shows the oxygen K-edge XAS results on different samples, where peak A is the covalent or hybridization mixing of oxygen 2*p* state with transition metal 3*d* state, peak B is due to the oxygen octahedral coordination, peak C is the mixed states of oxygen 2*p* state and lanthanum 5*d* state, and peak D is the mixed state of transition metal 4*sp* and lanthanum 5*sp*.[54-56] In a previous in-situ O K-edge XAS study, when different potentials were applied on the oxide catalysts, only peak A showed clear changes, which indicates peak A (i.e. the M-O covalency) is the most important property that is related to the oxygen adsorption and redox processes.[42] By calculating the area of peak A,[15] we can estimate the M-O hybridization of different perovskites, as shown in Figure 3.5b, which implies the reducing of M-O hybridization with increasing Fe contents. Previous studies on perovskite oxide for oxygen evolution reaction (OER) catalysis showed that a stronger M-O hybridization can optimize the oxygen adsorption, activate oxygen redox, and therefore reduce the overpotential required for 4-step OER process on perovskite oxides.[18, 45] However, few studies have been focused on the influence of M-O hybridization on the ORR catalysis. In this study, we showed that the increase of M-O covalency with less Fe and more Co in the perovskite B site can also accelerate the ORR kinetics, probably still due to the optimization of surface oxygen adsorption and the activation of oxygen redox observed for OER process. Furthermore, according to Figure 3.3d, a stronger hybridization between oxygen 2*p* band and metal 3*d* band in Co-rich samples also leads to a more beneficial 4-electron-transfer ORR pathway, which might be due to the reduction of the required overpotentials for the 4-step ORR mechanism. The intensity of peak A is also assigned to unoccupied states of Fe/Co 3*d*-O2*p* states generated by the Fe/Co 3*d* and O2*p* hybridization and linearly proportional to the total number of the empty Fe/Co 3*d*-O2*p* state.[6, 42] The surface oxidization state of Co and Fe can be roughly estimated by analyzing peak positions and peak shapes of XAS (Figure 3.4) and XPS (Figure 3.10) result. Comparing with XAS and XPS results in previous literature, we find the surface Co and Fe are roughly Co(III) and Fe(III).[57-60] Then the amount of e_g holes, t_{2g} holes and unoccupied states have been calculated in Figure 5c using the intermediate spin Co(III) and high spin Fe(III).[6, 15] Figures 3.5a and 3.5c indicate less unoccupied states with more Fe doping. Since it is the highest unoccupied electronic exchanges electrons with the oxygen adsorbate species, more electrons in the highest unoccupied states (e_g) after Fe doping lead to stronger electron exchange with the adsorbed oxygen species, which can facilitate the releasing of free peroxides and promote the 2-electron transfer pathway during the ORR.[42] This conclusion emphasizes the electronic structure determines the reaction pathway, and is supported by previous study which found Fe(IV) can promote 4-electron-transfer (Note Fe(IV) has the same e_g electron as Co(III), but different from Fe(III) with e_g=2).[61]

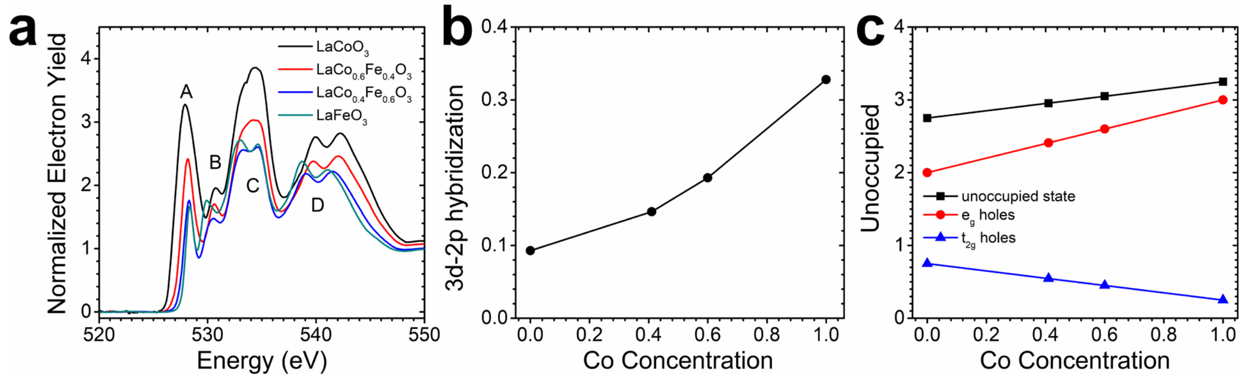

Figure 3.5 (a) O K-edge spectroscopy in surface-sensitive yield mode of LaCo$_x$Fe$_{1-x}$O$_3$ (x= 0.0, 0.4, 0.6, 1). Peak A represents the Fe/Co 3d and O 2p hybridized states correlated with ORR catalytic activity. (b) Estimated 3d-2p hybridization by integration the peak A area as a function of surface Co ratio. (c) Calculated amount of e$_g$ holes, t$_{2g}$ holes and unoccupied states related correlated with surface Co-ratio by using high spin Fe(III) and intermediate spin Co (III).

In summary, we have studied the role of Fe substitution to tune the catalytic performance and ORR reaction mechanism. We observed the reduced catalysis activity and the decrease electron transfer number during the ORR process on perovskites with more Fe substitution. The sluggish ORR kinetics and less preferable 2-electron-transfer pathway observed in Fe-substituted perovskites is attributed to the increase of e$_g$ filling number and decrease of M-O covalency observed in the soft XAS results. This paper provides deep insights to the effect of electronic structures on the ORR kinetics and mechanisms, as well as guidelines to develop more active oxide catalysts with preferred ORR pathway in the future.

3.6. Acknowledgement

This work was financially supported by Callahan Faculty Scholar Endowment and start-up funds from Oregon State University. The hard X-ray microscopy measurements were done at 2-ID-D of Advanced Photon Source, which is a U.S. Department of Energy (DOE) Office of Science User Facility operated for the DOE Office of Science by Argonne National Laboratory under Contract No. DE-AC02-06CH11357. The soft X-ray absorption spectroscopy was performed at beamline 6.3.1 of Advanced Light Source, which is an Office of Science User Facility operated for the U.S. DOE Office of Science by Lawrence Berkeley National Laboratory and supported by the DOE under Contract No. DEAC02-05CH11231. Authors thank Anton Paar USA, Inc. for the BET tests.

3.7. Supplementary Information

3.7.1. Material Synthesis

$LaCo_xFe_{1-x}O_3$ (x = 0, 0.4, 0.6, 1) powders were synthesized by using high temperature solid state reaction. La_2O_3, Fe_2O_3 and Co_3O_4 were mixed stoichiometrically. The mixed powder was heated in air up to 1673 K for 24 hours. The sample was naturally cooled down in the oven for several hours. Then the powder was taken out from the furnace and grinded. The well-grinded powder was heated up to 1673 K for another 24 hours.

3.7.2. Material Characterizations

X-ray diffraction (XRD): X-ray diffraction patterns were collected with a Bruker-AXS D8 Discover machine with a Cu-Kα X-ray tube (λ = 1.5406 Å). The XRD patterns were scanned between 10° to 90° with a scan speed of 0.05°/min.

X-ray photoelectron spectroscopy (XPS): The XPS results were collected with a Axis Ultra DLD Spectrometer (Kratos Analytical) equipped with a Monochromatic Al K_X-ray source (1486.6 eV). The spot size is 700 μm by 300 μm.

High-resolution X-ray microscopy: Simultaneous X-ray ptychorgraphy and fluorescence microscopy were performed on $LaCo_xFe_{1-x}O_3$ micro-particles at 2-ID-D beamline located at the Advanced Photon Source (APS) in Argonne National Laboratory (ANL). A 10.42 keV monochromatic X-ray beam was focused by a Fresnel zone plate with an outer zone width of 70 nm on to the sample. As the sample was scanned, coherent diffraction patterns were collected with a Dectris Eiger 500K hybrid pixel array detector that was located 1.75 m downstream of the sample, and fluorescence signals were simultaneously recorded by a Vortex silicon drift detector. Those diffraction patterns were reconstructed into real-space images with 5.65 nm pixels by a GPU-based code.[62]

Soft X-ray absorption spectroscopy: Total electron yield of transition metal L-edge and O K-edge was measured at beamline 6.3.1 Advance Light Source (ALS) at Lawrence Berkeley National Laboratory (LBNL) under vacuum condition.

Brunauer–Emmett–Teller (BET) test: The BET surface area was measured by Quantachrome Instrument LabQM. The multi-point BET specific surface area was taken by krypton adsorption at 77K using vacuum-volumetric method.

3.7.3. Electrochemical Test

To perform the electrochemical tests, three-electrode rotating-disk method was carried out by using $LaCo_xFe_{1-x}O_3$ as the working electrode, Pt as the counter electrode, and Ag/AgCl as the reference electrode, respectively. To make the catalyst slurry for working electrodes, 20 mg metal oxide and 4 mg Timcal Super C45 conductive carbon black purchased from MTI (C45) were dispersed in a mixed solution of 3 ml 18 MΩ Deionized (DI) water, 0.88 ml isopropanol and 0.12 ml 3.33wt% Nafion. The mixture was sonicated for 1 hour. Then 10 µL homogenous solution was dropped onto the 0.196 cm^2 glassy carbon rotation disk electrode and dried in air overnight to make the uniform working electrode. Cyclic voltammetry of double-capacitance background and ORR were performed using CHI 760E potentiostat in 0.1 M Ar and O_2 saturated KOH electrolyte (made with 18 mΩ DI water) respectively at 20 mV/s between 0.05 and 1.1 V vs. reversible hydrogen electrode (RHE). Double-capacitance current was measured under 0 rpm, and ORR current was measured under different rotation rates (1600, 900, 400, and 100 rpm).

To estimate ORR catalytic activity, the measured current (i_m) was subtracted by the double-capacitance current (i_{bg}) (Equation S1). Then the current (i) was corrected by using Koutecky–Levich equation (Equation S2) to get the kinetic current ($i_{kinetic}$), which will be further normalized by the BET surface area. The voltage was corrected by the $i_m R$ correction.

$$i = i_m - i_{bg} \qquad \text{(Eq. S3.1)}$$

$$\frac{1}{i} = \frac{1}{i_{limit}} + \frac{1}{i_{kinetic}} \qquad \text{(Eq. S3.2)}$$

To calculate the limiting current (i_{limit}) and the number of electron transfer (n), the background corrected current (i) was selected at different rotation speeds at a certain voltage, which will be plotted against the inverse root of rotation speed, as shown in Equation S3. The slope a of this plot, according to Equation S3, is reversely proportional to the number of electron transfer. By comparing with the slope of 4-electron-transferred measurement on pure Pt disk, we can calculate the limiting currents and the electron transfer numbers of different samples at different voltages during the ORR.

$$\frac{1}{i} = \frac{1}{0.062nFAD^{\frac{2}{3}}\omega^{\frac{1}{2}}v^{-\frac{1}{6}}C} + \frac{1}{i_{kinetic}} = a\frac{1}{\omega^{\frac{1}{2}}} + b \quad \text{(Eq. S3.3)}$$

3.7.4. Estimation of eg number in $LaCo_xFe_{1-x}O_3$

XAS in Figure 4 shows that Co has intermediate spin state and Fe has high spin state and XPS in Figure 3.10 suggest that Co and Fe have the oxidation state of 3+. Based on these, Co(III) has e_g=1 and Fe(III) has e_g=2. Therefore, the average e_g number in different compositions can be calculated using the following mathematical equation:

$$\text{n} = \frac{1\times Concentration(Co) + 2\times Concentration(Fe)}{Concentration(Co) + Concentration(Fe)}, \quad \text{(Eq. S3.4)}$$

where, 1 refers to the intermediate spin Co(III) with e_g = 1, 2 represents a high spin Fe(III) with e_g = 2, and the concentrations are determined by the XPS, as shown in Table 1.

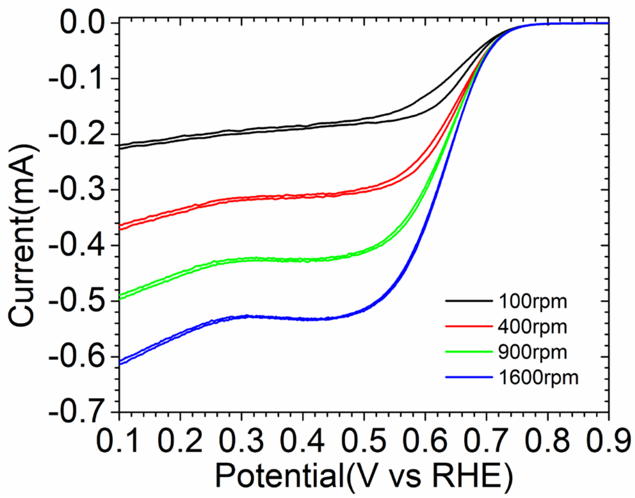

Figure 3.6 Background-subtracted ORR activity current of $LaCoO_3$ at different rotation speeds (1600, 900, 400, and 100 rpm) with the scan rate of 20 mV/s. The current at different rotation speeds can be used to calculate the number of electron transfer by using the Koutecky-Levich equation.

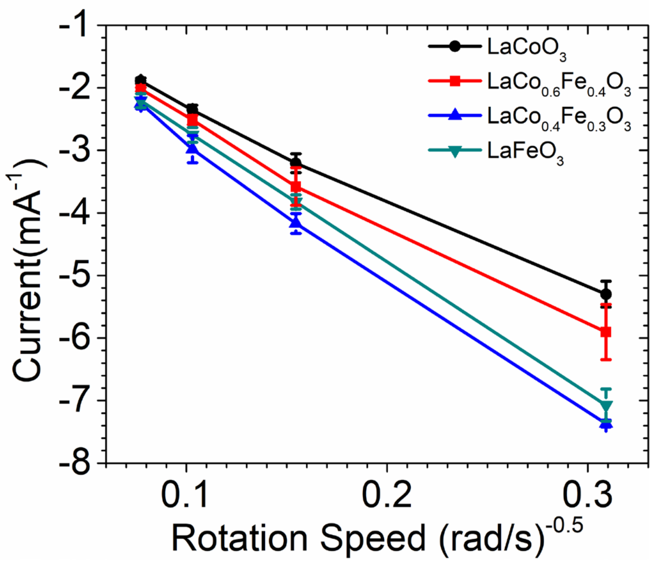

Figure 3.7 ORR current at 0.34 V vs. RHE corrected only by background subtraction as a function of rotation speeds for the Koutecky-Levich equation analysis, which indicates numbers of electron transfer. The greater slope represents higher electron transfer number.

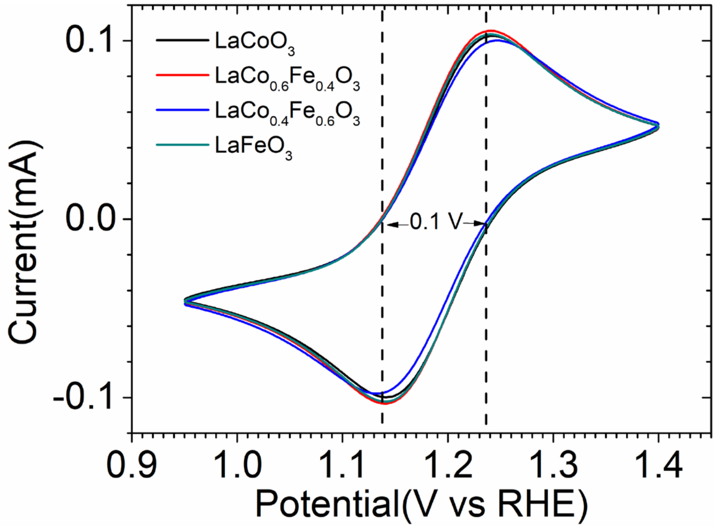

Figure 3.8 Cyclic voltammetry of conductivity measured in Ar-saturated 5 mM $K_3Fe(CN)_6$ and 5 mM $K_4Fe(CN)_6$ solutions at 20 mV/s for $LaCo_xFe_{1-x}O_3$ (x=0 ,0.4, 0.6, 1) The voltage differences between forward and backward peaks are all around 0.1 V, implying similar conductivity among different samples.

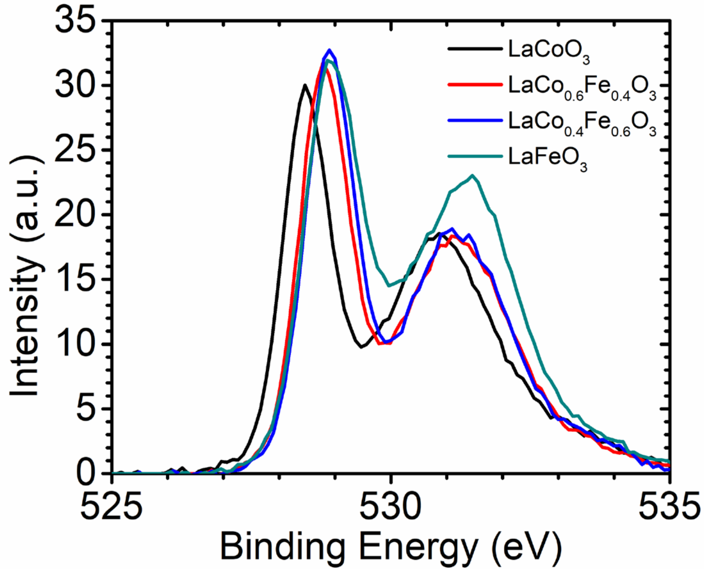

Figure 3.9 Normalized background-subtracted O 1s XPS of pristine $LaCo_xFe_{1-x}O_3$ (x=0 ,0.4, 0.6, 1) particles.

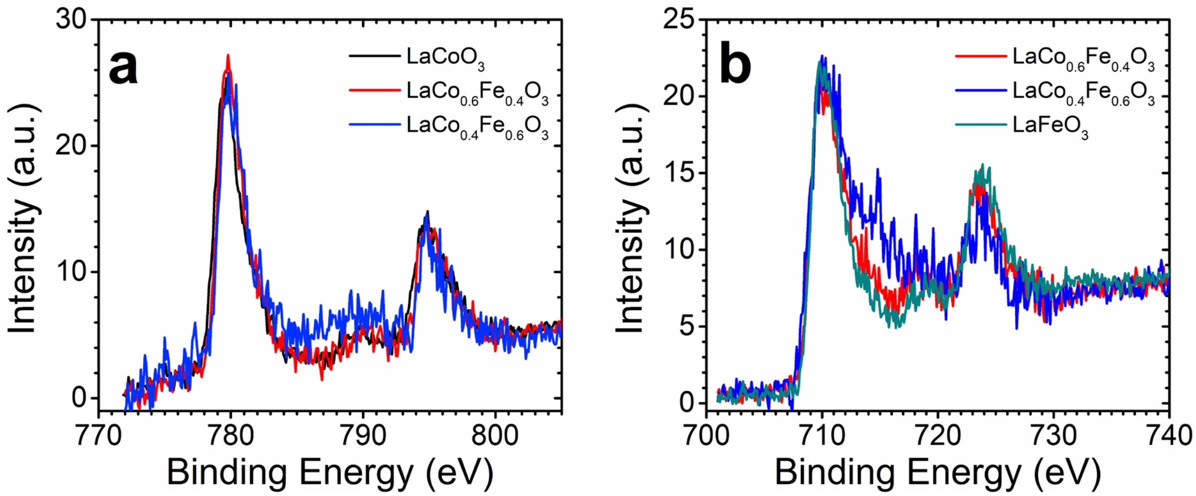

Figure 3.10 Normalized background-subtracted (a) Co 2p and (b) Fe 2p XPS of pristine LaCo$_x$Fe$_{1-x}$O$_3$ (x=0, 0.4, 0.6, 1) particles.

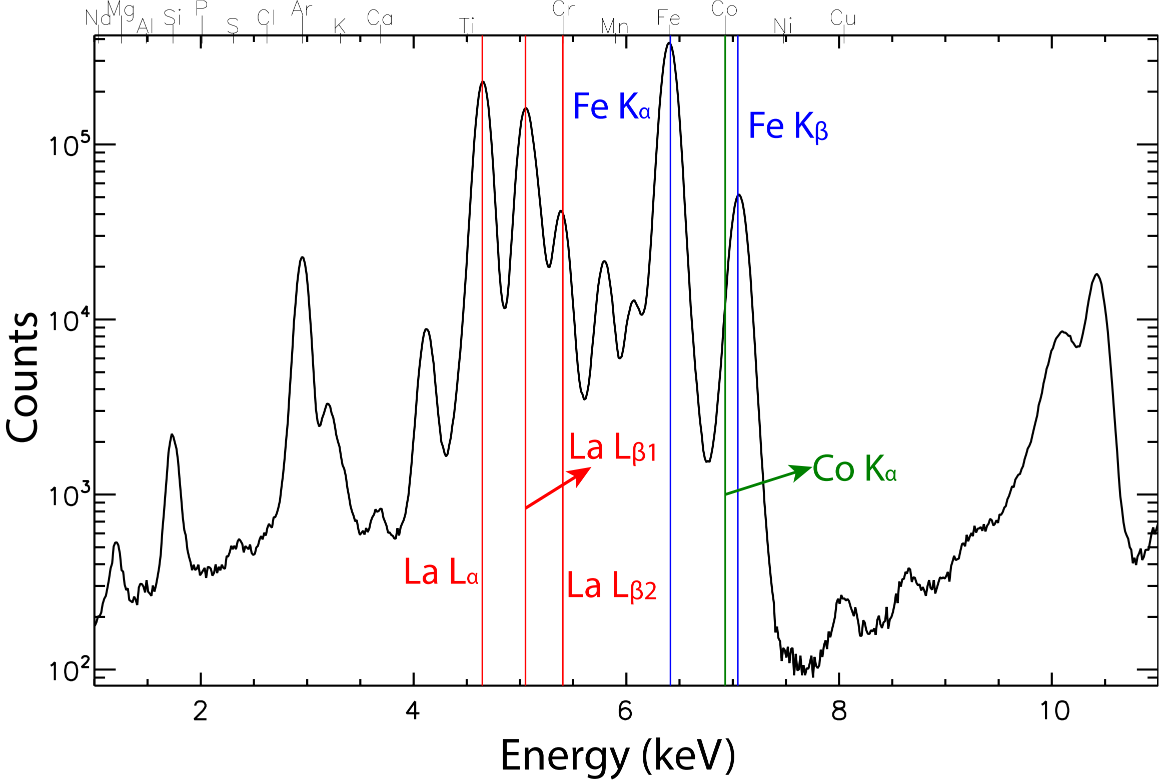

Figure 3.11 A representative X-ray fluorescence spectrum of LaFeO$_3$ particle from X-ray microscopy measurements to obtain the element distribution in Figure 2. The Co K$_\alpha$ fluorescence line is on the shoulder of Fe K$_\alpha$ peak, which could result in some Co fluorescence signals on LaFeO$_3$ during fluorescence data fitting.

Table 3.1 XPS analysis of surface Co and Fe ratios of different samples used in this paper.

Sample	**Name**	**Position (eV)**	**Raw Area**	**Concentration (%)**
$LaFe_{0.6}Co_{0.4}O_3$	Co 2p	779.8	4081.8	33.7
	Fe 2p	710.3	7011.9	66.3
$LaFe_{0.4}Co_{0.6}O_3$	Co 2p	779.8	6518.7	52.7
	Fe 2p	711.0	5124.7	47.3
$LaCoO_3$	Co 2p	779.7	8416.7	100
$LaFeO_3$	Fe 2p	709.8	7572.2	100

Table 3.2 BET surface area of different samples used in this paper.

Sample	**Area (m^2/g)**
$LaCoO_3$	0.179
$LaFe_{0.6}Co_{0.4}O_3$	0.264
$LaFe_{0.4}Co_{0.6}O_3$	0.302
$LaFeO_3$	0.565

Table 3.3 The integral fluorescence counts of La_L, Co, Fe by X-ray fluorescence analysis.

Sample	**La_L (counts)**	**Co (counts)**	**Fe (counts)**
$LaCoO_3$	1.81×10^7	2.75×10^7	-
La $Co_{0.6}Fe_{0.4}O_3$	2.84×10^7	2.90×10^7	1.46×10^7
$LaCo_{0.4}$ $Fe_{0.6}O_3$	3.10×10^7	1.29×10^7	3.04×10^7

$LaFeO_3$	2.15×10^7	-	2.72×10^7

Chapter 4. Engineering Modification of $LaCoO_3$ with Fe and P co-substitution to Improve Oxygen Evolution Catalytic Activity

Engineering Modification of $LaCoO_3$ with Fe and P co-substitution to Improve Oxygen Evolution Catalytic Activity

Maoyu Wang[a], Kingsley Chukwuma Chukwu[a], Brian Allen Muhich[a], Widitha Samarakoon[a,b], Alpha T N'Diaye[c], George Sterbinsky[d], Zizhou He[e], Ling Fei[e], Líney Árnadóttir[a*], Zhenxing Feng[a*]

[a] Department of Chemical, Biological and Environmental Engineering, Oregon State University, Corvallis, Oregon 97331, United States

[b] Physical and Computational Sciences Directorate, Pacific Northwest National Laboratory, Richland, Washington 99354, United States

[c]Advanced Light Source, Lawrence Berkeley National Laboratory, Berkeley, California 94720, United States

[d]Advanced Photon Source, Argonne National Laboratory, Argonne, Illinois 60439, United States

[e]Chemical Engineering Department, University of Louisiana at Lafayette, Lafayette, Louisiana 70504, United States

*Corresponding author: zhenxing.feng@oregonstate.edu

Abstract

The high-efficiency and low-cost catalysts for oxygen evolution reaction (OER) are critical for electrochemical water splitting to generate hydrogen as the clean fuel for sustainable energy conversion and storage. Transition metal perovskite ($LaCoO_3$) are an emerging type of OER has been studies as on the stable and active OER catalyst. Although researchers have tried various B-site cation substation into the Co-based perovskite catalysts to improve the OER performance, the influence of substitution on the OER mechanism is rarely studied. Here, the combination of ex-situ soft and operando hard X-ray absorption spectroscopy, X-ray diffraction, electrochemical tests, and density of function theory was carried out to explore the OER mechanism after co-substituting Fe and P into $LaCoO_3$. We observed enhanced OER catalytic activities in co-substituted materials, which are attributed to the stronger transition-metal-oxygen-bonding covalency. The detailed analysis around O K-edge XAS, electrochemical performance, and DFT pointed out the hybridization between O 2p and transition metal e_g orbit could be a more credible descriptor of OER performance, which is the combination of e_g orbit theory and transition-metal-oxygen-bonding covalency theory. The discoveries in this paper provide deep insights into the OER catalysis mechanism on metal oxides and new guidelines for the design of Pt-free OER catalysts.

Introduction

Developing sustainable energy conversion and storage techniques is key to combatting climate change and its harmful effects.[63-65] A promising solution is the use of electrochemical energy conversion to split water and generate hydrogen, which can be stored and used as a next-generation energy vector, thereby promoting the so-called “hydrogen economy”.[66, 67] Water splitting consists of two main electrochemical reactions, namely hydrogen evolution reaction

(HER) and oxygen evolution reaction (OER) occurring at the cathode and the anode, respectively. Compared to HER, the four-electron OER is more challenging due to its relatively sluggish kinetics and high overpotential.[12, 61] Therefore, significant emphasis has been directed towards conducting research to identify cost-effective, active, and stable catalysts for promoting OER.

Over the past decades, the efficient OER catalysts are mainly based on precious metals and their oxides such as IrO_2 and RuO_2. Due to their high costs, alternative materials such as transition metal oxides have been explored as electrocatalysts in OER. For example, Shao-horn's group presented the $Ba_{0.5}Sr_{0.5}Co_{0.8}Fe_{0.2}O_{3-\delta}$ show much better catalytic activity than the state-of-art IrO_2.[16] They also pointed out the highest OER activity could be achieved at an e_g occupancy close to unity with high transition-metal-oxygen-bonding covalency (TMOBC).[16] Best on these e_g orbit and covalency theory, Xu's tailored the Co-O bonding covalency via substituting Fe into $LaCoO_3$.[12] They found that $LaCo_{0.9}Fe_{0.1}O_3$ shows the best OER performance among different percent Fe substitution due to the highest TMOBC.[61] Recently, the P doping has become one new approach to enhance the OER performance of perovskite.[68, 69] For example, Chen's group found the high-valence-state P substituting in $SrCo_{0.8}Fe_{0.2}O_3$ would enhance the OER performance due to introducing more oxygen vacancy. However, the current studies lack of fundamental understanding of P substituting such as whether P substituting would change e_g orbit or modify the TMOBC.

In this work, we started with $LaCo_{0.9}Fe_{0.1}O_3$, the best OER catalysts in the $LaCo_xFe_{1-x}O3$ series. By substituting Fe with P, we found that $LaCo_{0.9}Fe_{0.05}P_{0.05}O_3$ shows the best OER performance, and even $LaCo_{0.9}P_{0.1}O_3$ shows better OER performance than $LaCo_{0.9}Fe_{0.1}O_3$. With the help from multimodal characterization tools including operando X-ray diffraction (XRD) and operando hard X-ray absorption spectroscopy (XAS) together with electrochemical performance, we revealed that those materials would not undergo any obvious crystal and local structure change under OER conditions, which means only surface adsorption and desorption happens. Furthermore, ex-soft XAS illustrated that P substitution would not change either Co or Fe electronic structure or crystal structure, but it would change TMOBC. Additionally, by combining O K-edge XAS with the density of function theory (DFT) results, we hypothesized a new approach for explanation the enhanced OER performance: the hybridization between e_g orbit and O 2p bond is more critical to determine the OER performance, which summarized the e_g orbit theory and TMOBC theory together.

Results and Discussion

XRD was carried out to reveal the crystal structure of $LaCo_{0.9}P_{0.1}O_3$, $LaCo_{0.9}Fe_{0.05}P_{0.05}O_3$, and $LaCo_{0.9}Fe_{0.1}O_3$ (Figure 4.1). There is no phase transition change caused by Fe and P substitution, and all those three materials show the rhombohedral structure, which is the same as pure $LaCoO_3$. To quantify the surface are of $LaCo_{0.9}Fe_xP_{0.1-x}O_3$, the Brunauer-Emmett-Teller (BET) tests were carried out and the specific surface areas of these $LaCo_{0.9}Fe_xP_{0.1-x}O_3$ are around 3.6 m^2/g (Table 4.1), which does not show big difference. Energy dispersive X-ray spectroscopy (EDS) was also carried out to ensure we get the Fe and P successful substituted into $LaCoO_3$ (Figure 4.5a, b, c), and the scanning electron microscopy (SEM) confirms the same morphology for all three different materials (Figure 4.5e, d, f). The element distribution ratio estimated from EDS (Table 4.2) confirms the correct composition of synthesized materials. The OER performance of $LaCo_{0.9}Fe_xP_{0.1-x}O_3$ was tested in 0.1M KOH solutions using the three-electrode rotating disk method. After normalizing the OER current with BET surface area, it indicates that $LaCo_{0.9}Fe_{0.05}P_{0.05}O_3$ has the best OER performance with lowest overpotential, and the $LaCo_{0.9}Fe_{0.1}O_3$ shows the worst OER performance. The $LaCo_{0.9}Fe_{0.1}O_3$ shows the same OER performance as mentioned in previous literature,[12] which also confirms that our P-substation would enhance the OER catalytic performance. Based on the XRD, all three materials have the same crystalline structure, so the crystal structure would affect the OER performance. Ex-situ XAS was also carried out to obtain the valence state, electronic structure, and local structure of both Co and Fe (Figure 4.2 a&b).[24, 70, 71] Due to the different electronic structure from $Co(NO_3)_3$ and Fe_2O_3 (Figure 4.2), the X-ray absorption near edge structure (XANES) shape is different from stand Co(III) and Fe(III), but the Co in all three $LaCo_{0.9}Fe_xP_{0.1-x}O_3$ shows close valence state to Co(III), and Fe shows a little bit higher valence state than Fe(III).[12, 70] Also, all $LaCo_{0.9}Fe_xP_{0.1-x}O_3$ have the same Co and Fe valence states, which means the substation would change the oxidization state to influence the OER performance. Moreover, figure 4.2b indicates small minor structure change on Fe and Co, which may be caused by the noise points in the Fourier Transfer k-space (Figure 4.6). Hence, the P substitution does not do big change on both electronic structure and local structure to cause different OER performance.

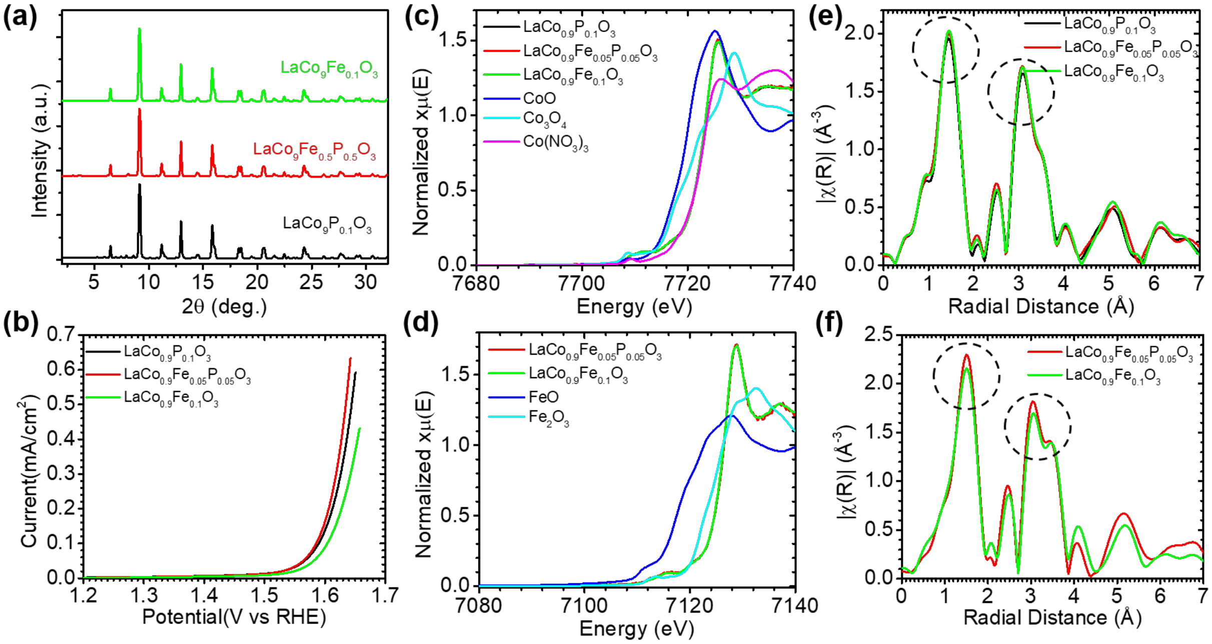

Figure 4.1 (a) XRD diffraction, (b) OER performance, (c) Co K-edge XANES, (d) Fe K-edge XANES, (e) Co K-edge Fourier Transfer R-space, (f) Fe K-edge Fourier Transfer R-space of $LaCo_{0.9}P_{0.1}O_3$, $LaCo_{0.9}Fe_{0.05}P_{0.05}O_3$, and $LaCo_{0.9}Fe_{0.1}O_3$

To further understand the OER reaction mechanism and how P-substation involved in the catalytic reaction. The operando characterization were carried out. The operando XRD (Figure 4.7) illustrated no change in the crystal structure for all three materials. Hence, we believe the OER will only happen on the surface of materials and it would change any bulk structure. The operando XAS was also carried out to observe any electronic structure or local structure change during the OER (Figure 4.2&4.7).[72, 73] Based on the Co K-edge XANES, there is not electronic structure change of Co on those $LaCo_{0.9}Fe_xP_{0.1-x}O_3$ materials during the catalytic reaction (Figure 4.2a). Also, no Co local structure change of those $LaCo_{0.9}Fe_xP_{0.1-x}O_3$ materials (Figure 4.2c). The similar situation was found in operando Fe K-edge XAS (Figure 4.8). There is no either electronic change or local structure change on those materials during the catalytic reaction. One possible reason is that XAS is a bulk sensitive techniques, so most bulk Co and Fe would involve in the reaction, and the only tiny surface Co and Fe change are below the XAS detection limited.[74] It is also possible that the bulk oxygen involved in the catalytic reaction, which would not cause any structure change of both Co and Fe.[11]

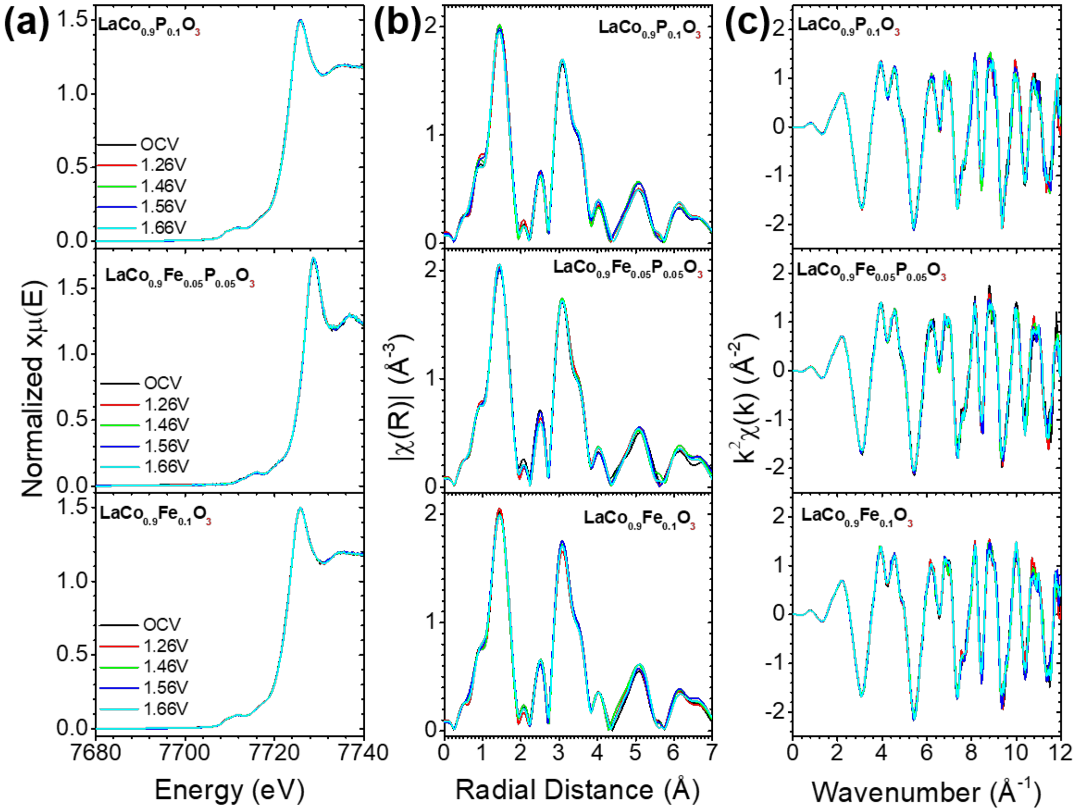

Figure 4.2 Operando Co K-edge (a) XANES (b) Fourier Transfer R-space (c) Fourier transfer k-space for $LaCo_{0.9}P_{0.1}O_3$, $LaCo_{0.9}Fe_{0.05}P_{0.05}O_3$, and $LaCo_{0.9}Fe_{0.1}O_3$

Due to no electronic structure and local structure change, the e_g orbital theory based on 3d transition metal would not work well in explaining the increased OER performance of $LaCo_{0.9}Fe_xP_{0.1-x}O_3$ materials. Therefore, the TMOBC theory, another important descriptor for perovskite OER performance,[12, 16] was introduced to help explain the electrocatalyst catalytic performance. O K-edge XAS were carried out to estimate TMOBC (Figure 4.3a).[75-78] It is clear that the P substitution would have a huge influence the O K-edge spectrum (Figure 4.3a). Peak a and peak b stands for the TMOBC (Figure 4.3a), which suggests completely difference in TMOBC around three $LaCo_{0.9}Fe_xP_{0.1-x}O_3$ materials. Therefore, such increased OER catalytic is caused by changing of TMOBC. To further comparing with the TMOBC theory, the area of peak a and peak b was used to estimation the TMOBC strength. Based on the method mentioned in previous literature, Co was treated as Co(III) with intermediate spin and Fe(III) with high spin.[15, 78] The results (Figure 4.3b) illustrated that $LaCo_{0.9}Fe_{0.05}P_{0.05}O_3$ has the strongest TMOBC, and it also shows the best OER performance. It consists with previous reported trend.[12, 15] However, the $LaCo_{0.9}Fe_{0.1}O_3$ should have better OER performance than $LaCo_{0.9}P_{0.1}O_3$ since the $LaCo_{0.9}Fe_{0.1}O_3$ has stronger TMOBC than $LaCo_{0.9}P_{0.1}O_3$, which is against previous TMOBC theory.[12, 15] Therefore, more detailed analysis was performed on the O K-edge XAS. According to previous literature, peak a can be treated as the transition metal t_{2g} and O 2p hybridization, and peak b can be treated as the transition metal e_g and O 2p hybridization.[75] The estimated hybridization are shown in figure 4.3c and figure 4.3d. The TMOBC of $LaCo_{0.9}Fe_{0.1}O_3$ are majority from t_{2g} hybridization, but the TMOBC of $LaCo_{0.9}P_{0.1}O_3$ are dominated by e_g hybridization. Based on the e_g hybridization strength, the $LaCo_{0.9}P_{0.1}O_3$ would have better OER performance than $LaCo_{0.9}Fe_{0.1}O_3$, which consists with our OER performance. However, the $LaCo_{0.9}Fe_{0.05}P_{0.05}O_3$ has close e_g hybridization but much larger t_{2g} hybridization compared with $LaCo_{0.9}P_{0.1}O_3$, and the $LaCo_{0.9}Fe_{0.05}P_{0.05}O_3$ has very similar OER performance with $LaCo_{0.9}P_{0.1}O_3$. The estimation of those hybridization based on EDS were also calculated (Figure 4.9), which shows the same trend as the general estimation. Hence, we ambiguously proposed a new descriptor for perovskite OER catalytic performance: the greater transition metal e_g orbit hybridization with O 2p orbit leads to higher OER performance.

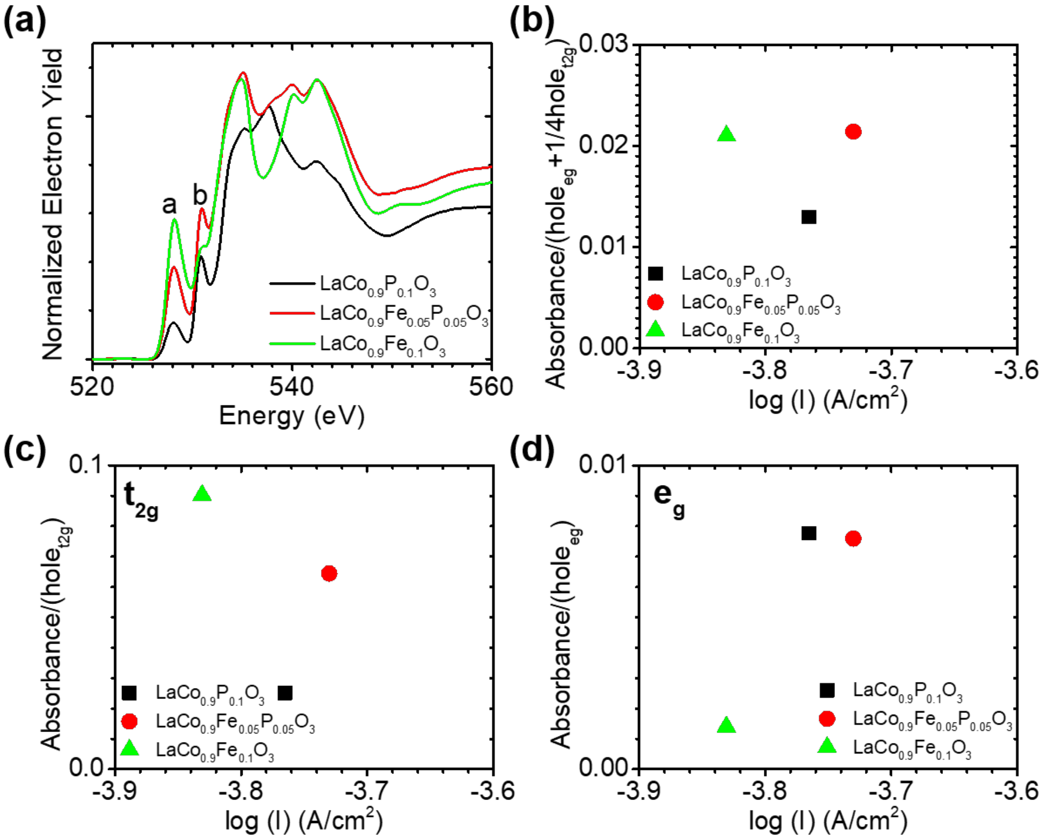

Figure 4.3 (a) O K-edge XAS, (b) estimation of TMOBC, (c) estimation of transition metal t_{2g} and O 2p hybridization, (d) estimation of transition metal e_g and O 2p hybridization for $LaCo_{0.9}P_{0.1}O_3$, $LaCo_{0.9}Fe_{0.05}P_{0.05}O_3$, and $LaCo_{0.9}Fe_{0.1}O_3$ (The current density for comparing is the current at overpotential equaling to 0.3V)

To further confirm the OER catalytic activity, the DFT was carried out to estimate the surface absorption of OH groups (Figure 4.4). According to previous study, the OER (oxygen evolution reaction) performance for Perovskite has a linear relationship with adsorption energy of OH.[79-81] We observed that the experimental OER performance increases with decrease in the calculated adsorption energy of OH on the perovskite and OH stretching frequency (see Figure 4.4a). Lower adsorption energy favors the first elementary reaction step ($OH^- + * \rightarrow OH^* + e^-$). This suggests that it is most energetically favorable for OH to adsorb on the $LaCo_{0.92}Fe_{0.04}P_{0.04}O_3$ Perovskite. Figure 4.4b shows how the OER activity increases with lower OH stretching frequency.

Lower OH stretching frequency indicates that OH bond is weaker, so it is easier for the second elementary reaction step ($OH^* + OH^- \rightarrow O^* + H_2O + e^-$) of the OER to occur. The second elementary step involves the shuttling of the hydrogen into the solution. Weaker OH bond enhances the shuttling of H into the solution. Based on the DFT results, it confirms that the $LaCo_{0.9}Fe_{0.05}P_{0.05}O_3$ has the best OER performance with lowest overpotential, and the $LaCo_{0.9}Fe_{0.1}O_3$ shows the worst OER performance.

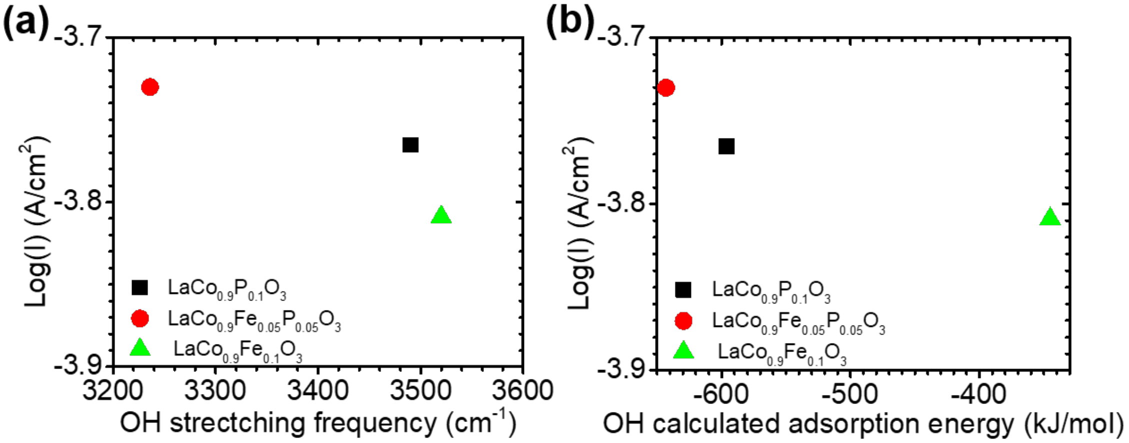

Figure 4.4 (a) Plot for Log of the experimental current density (at 0.3V overpotential) vs OH adsorption energy for different Perovskite structure (b) Plot for Log of the experimental current density (at 0.3V overpotential) vs OH adsorption energy for different Perovskite structure.

Conclusion

In summary, we have studied the role of P substitution to tune the OER catalytic performance. We observed the increased OER catalytic activity with co-substitution of P and Fe due to the change of TMOBC. According to detailed O K-edge XAS analysis, we proposed that the greater transition metal e_g orbit hybridization with O 2p orbit leads to higher OER performance, which combines the e_g orbit theory and TMOBC theorgy as one new descriptor. This paper provides deep insights to the effect of electronic structures on the OER kinetics and mechanisms, as well as guidelines to develop more active oxide catalysts for OER in the future.

Acknowledgement

This work was financially supported by Callahan Faculty Scholar Endowment and start-up funds from Oregon State University. The XAS measurements were done at beamline 9BM-B,C of the Advanced Photon Source, which is a U.S. Department of Energy (DOE) Office of Science User Facility operated for the DOE Office of Science by Argonne National Laboratory under Contract No. DE-AC02-06CH11357.The soft X-ray absorption spectroscopy was performed at beamline 6.3.1 of Advanced Light Source, which is an Office of Science User Facility operated for the U.S. DOE Office of Science by Lawrence Berkeley National Laboratory and supported by the DOE under Contract No. DEAC02-05CH11231.

Supporting Information

Material Synthesis

$LaCo_{0.9}P_xFe_{0.1-x}O_3$ (x = 0, 0.05, 0.1) powders were synthesized b via a sol-gel process combining the ethylenediamine tetra acetic acid (EDTA) and citrate acid (CA) as complexing agents.[68, 69] $La(NO_3)_3$, $Co(NO_3)_2 \cdot 6H_2O$, $Fe(NO_3)_3 \cdot 9H_2O$ and $NH_4H_2PO_4$ were mixed stoichiometrically. The mixed powder were dissolved in 5-10ml deionized water as solution A. EDTA and CA at a molar ratio of 1: 1: 2 for total metal ions: EDTA: CA were also dissolved in about 10-20ml deionized water as solution B. Solution B was slowly added to the solution A with continuous stirring. The pH of solution was adjusted to ~6 with the addition of NH3·H2O in order to reach the complete complexation. The mixed solution proceeded to stir and heat in the oil bath at 85°C until the water evaporated to form a transparent gel. The transparent gel was calcined at 250°C for 5hr to form a solid precursor, and further calcined at 950°C for another 5hr in the furnace to get the final powder products. The calcined powder were ground well and used as the perovskite electrocatalyst.

Material Characterizations

Electrochemical test: To perform the electrochemical tests, three-electrode rotating-disk method was carried out by using $LaCo_{0.9}P_xFe_{0.1-x}O_3$ as the working electrode, Pt as the counter electrode, and Ag/AgCl as the reference electrode, respectively. To make the catalyst slurry for working electrodes, 20 mg metal oxide and 4 mg Timcal Super C45 conductive carbon black purchased from MTI (C45) were dispersed in a mixed solution of 3 ml 18 MΩ Deionized (DI) water, 0.88 ml isopropanol and 0.12 ml 3.33wt% Nafion. The mixture was sonicated for 1 hour. Then 10 µL homogenous solution was dropped onto the 0.196 cm^2 glassy carbon rotation disk electrode and dried in air overnight to make the uniform working electrode. Cyclic voltammetry of OER were performed using CHI 760E potentiostat in O_2 saturated 0.1 M KOH electrolyte (made with 18 mΩ DI water) respectively at 20 mV/s between 1.2 and 1.7 V vs. reversible hydrogen electrode (RHE). The surface area of materials were measured via Brunauer-Emmett-Teller (BET) method, and the OER current were normalized by BET surface area.

Operando and ex-situ X-ray diffraction (XRD): X-ray diffraction patterns were collected with a Bruker-AXS D8 Discover machine with a Cu-Kα X-ray tube (λ = 1.5406 Å). The XRD patterns were scanned between 10º to 90º with a scan speed of 0.05º/min. Operando Powder XRD patterns were collected at the experimental station 13-BM of Advanced Photon Source (APS) of Argonne National Lab (ANL). To perform *operando* measurements, using the same ink procedure as prepared for electrochemical measurements, 0.4ml ink was deposited on the carbon paper in to form a 1cm*0.5cm area with 2mg active catalysts materials as the working electrode. Pt wire and Ag/AgCl were used as counter electrode and reference electrode, respectively. All three electrodes were mounted on a custom-designed electrochemical cell. The electrochemical data acquisition was done by using a Gamry Reference-600 electrochemical workstation under a O_2 gas flow of 30 sccm in 0.1 M KOH. Several potential points were selected based on preliminary cyclic voltammetry (CV) runs and were held for at least 15 minutes before acquiring XRD data.

Soft X-ray absorption spectroscopy: Total electron yield of transition metal L-edge and O K-edge was measured at beamline 6.3.1 Advance Light Source (ALS) at Lawrence Berkeley National Laboratory (LBNL) under vacuum condition.

Operando hard X-ray absorption spectroscopy: operando XAS experiments were carried out at 9BM-BC, APS of ANL. Both Co and Fe K-edge XANES and EXAFS were measured under fluorescence mode by a Vortex ME4 detector. The same working, counter and reference electrodes from operando XRD measurements were used in operando XAS. All three electrodes were mounted on a custom-designed *operando* XAS fluorescence cell,[1, 35, 82] and the electrochemical measurements were done by a Gamry Reference-600 electrochemical workstation under O_2 gas flow at 30 sccm in 0.1M KOH electrolyte. Several potential points were selected and held for at least 15 min to collect data to make sure completed reaction. All XAS data analysis were performed with Athena software package to extract XANES and EXAFS. Fourier Transform of Co and Fe K-edge EXAFS was performed by using Hanning window function with k-weights of 2.

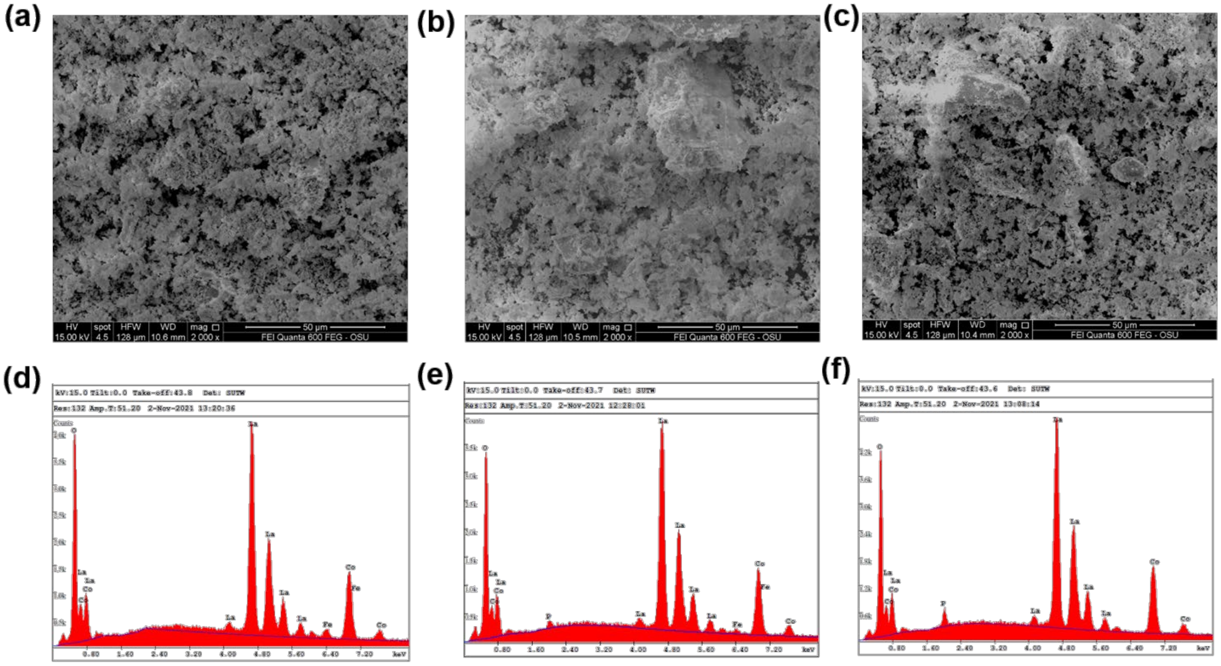

Figure 4.5 Scanning electron microscope of (a) $LaCo_{0.9}Fe_{0.1}O_3$ (b) $LaCo_{0.9}Fe_{0.05}P_{0.05}O_3$ (c) $LaCo_{0.9}Fe_{0.1}O_3$; Energy-dispersive X-ray spectroscopy of (d) $LaCo_{0.9}Fe_{0.1}O_3$ (e) $LaCo_{0.9}Fe_{0.05}P_{0.05}O_3$ (f) $LaCo_{0.9}Fe_{0.1}O_3$

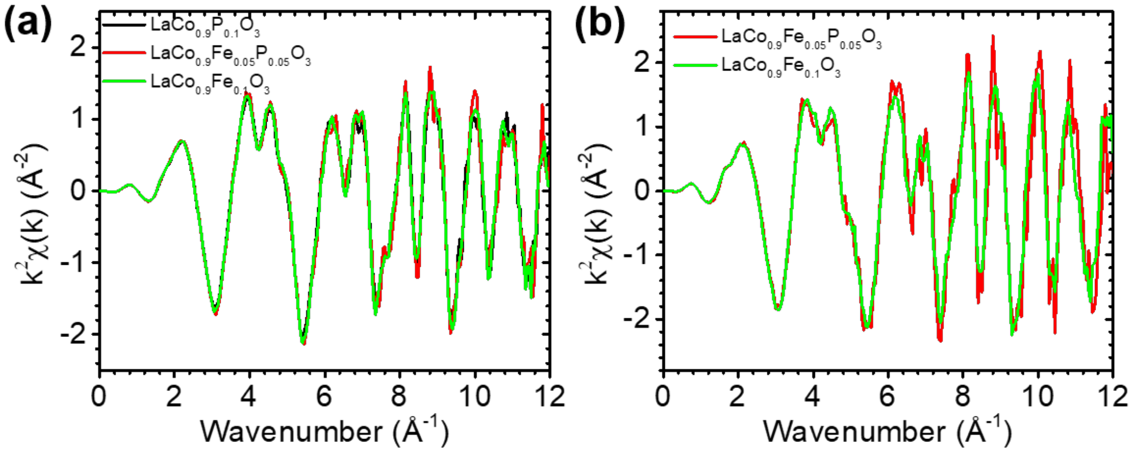

Figure 4.6 Ex-situ (a) Co K-edge and (b) Fe K-edge XAS Fourier transfer k-space for $LaCo_{0.9}P_{0.1}O_3$, $LaCo_{0.9}Fe_{0.05}P_{0.05}O_3$, and $LaCo_{0.9}Fe_{0.1}O_3$

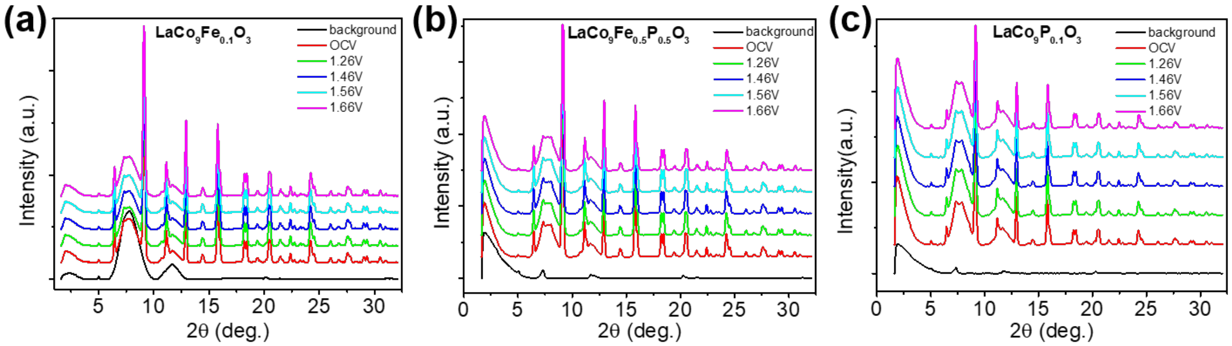

Figure 4.7 Operando XRD for (a) LaCo$_{0.9}$Fe$_{0.1}$O$_3$, (b) LaCo$_{0.9}$Fe$_{0.05}$P$_{0.05}$O$_3$, and (c) LaCo$_{0.9}$P$_{0.1}$O$_3$

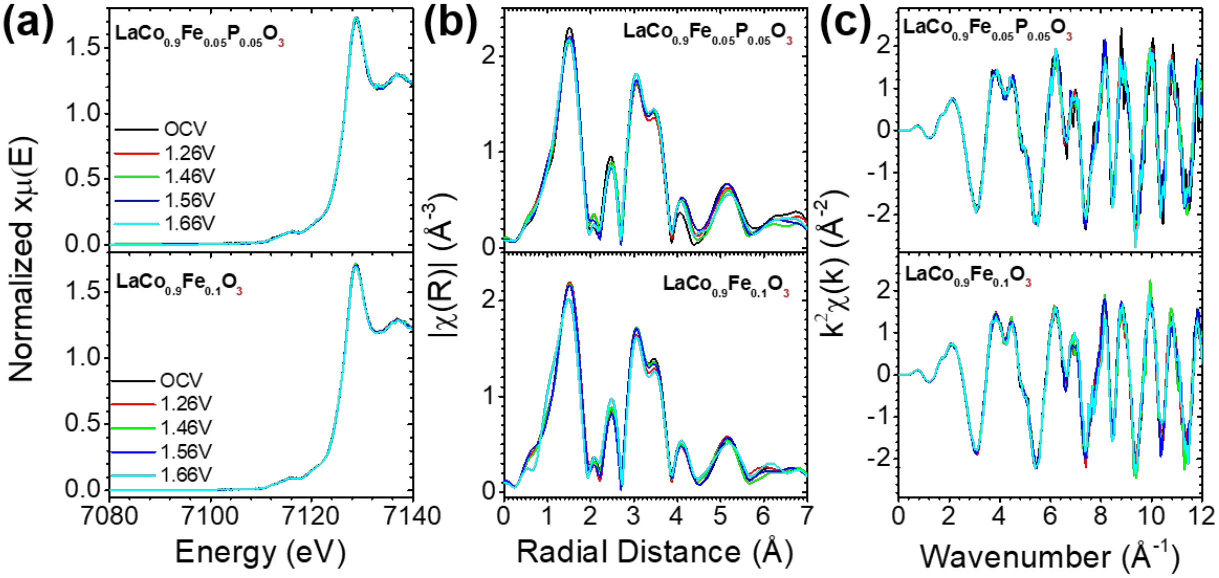

Figure 4.8 Operando Fe K-edge (a) XANES (b) Fourier Transfer R-space (c) Fourier transfer k-space for LaCo$_{0.9}$Fe$_{0.05}$P$_{0.05}$O$_3$ and LaCo$_{0.9}$Fe$_{0.1}$O$_3$

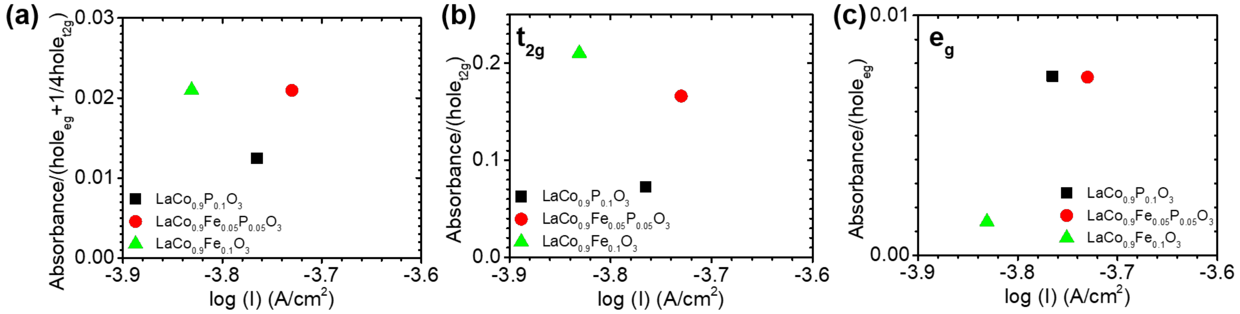

Figure 4.9 (a) estimation of transition metal oxygen bonding covalency, (b) estimation of transition metal t_{2g} and O 2p hybridization, (v) estimation of transition metal e_g and O 2p hybridization for LaCo$_{0.9}$P$_{0.1}$O$_3$, LaCo$_{0.9}$Fe$_{0.05}$P$_{0.05}$O$_3$, and LaCo$_{0.9}$Fe$_{0.1}$O$_3$ (The current density for comparing is the current at overpotential equaling to 0.3V) based on the EDS elemental ratio

Table 4.1 EDS elementary ratio:

$LaCo_{0.9}Fe_{0.1}O_3$	Element	wt%	atom%	K-Ratio	Z	A	F
	Fe K	9.58	10.06	0.0975	1.0186	0.9984	1.0000
	Co K	90.42	89.94	0.9025	0.9980	1.0001	1.0000
	Total	10.00	100.00				
$LaCo_{0.9}Fe_{0.05}P_{0.05}O_3$	Element	wt%	atom%	K-Ratio	Z	A	F
	P K	1.60	2.99	0.0125	1.1218	0.6953	1.0013
	Fe K	4.65	4.82	0.0472	1.0174	0.9981	1.0000
	Co K	93.75	92.19	0.9345	0.9968	0.9999	1.0000
	Total	10.00	100.00				
$LaCo_{0.9}P_{0.1}O_3$	Element	wt%	atom%	K-Ratio	Z	A	F
	P K	3.46	6.39	0.0271	1.1200	0.6981	1.0012
	Co K	96.54	93.61	0.9605	0.9953	0.9996	1.0000
	Total	10.00	100.00				

Table 4.2 BET surface area of different samples used in this paper

Sample	Area (m^2/g)
$LaCo_{0.9}Fe_{0.05}P_{0.05}O_3$	3.6356
$LaCo_{0.9}Fe_{0.1}O_3$	4.1249
$LaCo_{0.9}P_{0.1}O_3$	3.1269

Chapter 5. The Restructuring-Induced CoO_x Catalyst for Electrochemical Water Splitting

The Restructuring-Induced CoO_x Catalyst for Electrochemical Water Splitting

Maoyu Wang[1, †], Qingbo Wa[2, †], Xiaowan Bai[3, †], Zuyun He[4], Widitha S. Samarakoon[1], Qing Ma[5], Yingge Du[6], Yan Chen[4], Hua Zhou[7, *], Yuanyue Liu[3, *], Xinwei Wang[2, *], and Zhenxing Feng[1, *]

[1] School of Chemical, Biological and Environmental Engineering, Oregon State University, Corvallis, OR 97331, United States

[2] School of Advanced Materials, Shenzhen Graduate School Peking University, Shenzhen 518055, China

[3] Texas Materials Institute and Department of Mechanical Engineering, The University of Texas at Austin, Austin, Texas 78712, United States

[4] School of Environment and Energy, South China University of Technology, Guangzhou 510006, China

[5] DND-CAT, Synchrotron Research Center, Northwestern University, Evanston, IL, 60208, United States

[6] Physical and Computational Sciences Directorate, Pacific Northwest National Laboratory, Richland, Washington 99354, United States

[7] X-ray Science Division, Argonne National Laboratory, Lemont, IL, 60439, United States

†: Equally Contributed First Author

*: Corresponding Author

Reprinted with permission from JACS Au, 2021

5.1. Abstract

Restructuring is an important yet less understood phenomenon in the catalysis community. Recent studies have shown that a group of transition metal sulfide catalysts can completely or partially restructure during electrochemical reactions which then exhibit high activity even better than the best commercial standards. However, such restructuring processes and the final structures of the new catalysts are elusive, mainly due to the difficulty from the reaction-induced changes that cannot be captured by ex-situ characterizations. To establish the true structure-property relationship in these in-situ generated catalysts, in our study we use multi-model operando characterizations including Raman spectroscopy, X-ray absorption spectroscopy, and X-ray reflectivity to investigate the restructuring of a representative catalyst, Co_9S_8 that shows better activity compared to commercial standard RuO_2 during oxygen evolution reaction (OER), a key half reaction in water-splitting for hydrogen generation. We find that Co_9S_8 ultimately converts to oxide cluster (CoO_x) containing six oxygen coordinated Co octahedra as the basic unit which is the true catalytic center to promote high OER activity. The density functional theory (DFT) calculations verify the in-situ generated CoO_x consisting of edge-sharing CoO6 octahedral clusters as the actual active sites. Our results also provide insights to design other transition metal-based materials as efficient electrocatalysts that experience a similar restructuring in OER.

5.2. Introduction

Catalysts often undergo structural changes in working conditions to facilitate the reaction processes.[83-85] While reversible restructuring can maintain the catalysts' stability for long-term use, irreversible restructuring has long been believed to degrade their stability which can lead to a loss of activity due to undesirable changes in catalysts' compositions and structures. However, recent studies have shown that some materials (e.g., transition metal sulfides) can be unstable at the beginning of the reactions but evolve to new forms of catalysts with compositions and structures different from their initial states.[8, 86] These electrocatalysts, including transition metal chalcogenides, pnictides and carbides, are called metal X-ides and can exhibit superior activities, even better than the best commercial references.[8] Unfortunately, no agreement has been reached so far on the final structure of these metal X-ides.[8] in reactions and the origin of their superior activity/stability remains unclear.

One type of metal X-ides includes transition metal (i.e., Fe, Co, and Ni) sulfides which are earth-abundant materials and have attracted tremendous attention as a new group of catalysts for water oxidation in alkaline condition due to their comparable or superior activities compared to RuO_2 and IrO_2.[8] However, there is a lack of agreement on the composition of the "true" catalyst as these materials change at highly oxidative electrochemical conditions for oxygen evolution reaction (OER), a key half reaction to produce hydrogen as the clean fuel. The most prominent theories suggest that in highly oxidative condition these transition metal sulfide could restructure to metal oxide or (oxy)hydroxide, or partially oxidized/(oxy)hydroxidized compounds at the surface (Table 5.1),[8] which efficiently catalyze the reactions. Many literatures have indicated that the driving force for oxide (oxy)hydroxides OER is based on the transition metal redox couples (Table 5.2) such as Co(II)/Co(III), Co(III)/Co(IV), Ni(II)/Ni(III), and Ni(III)/Ni(IV). Unlike treating the metal oxidization state as a reaction center, some literature argued about the structure-dependent active sites for OER (Table 5.2). For example, Bergmann et. al. proposed that di-μ-oxo bond (a square structure formed by metal-oxygen-metal-oxygen) as a unified structural motif is the catalytically active site in the Co(oxyhydr)oxides;[87] Aliki et. al. suggested that the cobalt superoxide species as a key intermediate for cobalt oxyhydroxide OER; Kanan et al. demonstrated that the Co-oxo/hydroxo cluster in cobalt phosphate is the reaction site for OER.[88] Apparently these proposed active sites are different and some even conflict with each other. We hypothesize that there could be a common building block at atomic scale for these metal X-ides, acting as the catalytic site to promote the reaction with good stability. The active stie could also form different redox centers by absorbing and desorbing OH or aggregating together to form an oxo/hydroxo cluster with different oxidization states.

To prove our hypothetical theory, we need to understand the detailed restructuring processes for metal X-ides. Clearly, *ex-situ* characterizations, which are used to detect the pre- and post-chemical states of catalysts, cannot meet the requirements to study the reaction kinetics and any short-lived intermediates as well as transition forms of metal X-ides. To find out the true catalytically active sites of metal X-ides, *operando* characterizations are urgently required, as the structural, compositional and chemical information can be detected under reaction conditions.[1, 35, 70, 89-93] In this paper, we focus on a metal sulfide thin film, Co_9S_8, as a representative example of metal X-ides as it has excellent OER performance and reasonable stability compared to RuO_2.[94] Using multimodal *operando* characterizations including Raman spectroscopy, X-ray absorption spectroscopy (XAS) and X-ray reflective (XRR), we revealed the detailed structure and composition evolution of Co_9S_8 during OER. We unambiguously identified the edge-sharing CoO_6 octahedral clusters as the true active sites for CoO_x formed in OER, which is supported by the density function theory (DFT) calculations.

5.3. Results and Discussion

To investigate the reaction kinetics of as-deposited Co_9S_8 film, cyclic voltammetry (CV) was employed in 0.1 M KOH solution at a scan rate of 2 mV/s. As shown in Figure 1a for the first-cycle, the Co_9S_8 catalyst exhibited an excellent performance as the operational potential at a current density of 10 mA cm^{-2} ($E_{j=10}$) is 1.55 V (323 mV overpotential compared to 409 mV for

RuO_2).[94] The 1st cycle CV curve also exhibits pronounced irreversible feature as the integrated area of the anodic peaks (positive current values) at voltages less than 1.4 V was much larger than that of the cathodic peaks (negative current values), suggesting the oxidation of the Co_9S_8 catalyst (Figure 1a). In addition, by investigating the 2nd derivation of the curve,[95, 96] the anodic band at 1.15~1.4 V has two peaks at 1.27 and 1.31 V (Figure 5.5a-5.5b), which could be due to change of the coordination environments for cobalt atoms. Compared to the 1st cycle, the integrated area of anodic peaks for the following 2nd-5th cycles is much smaller (Figure 5.1b), and the 1.05 V anodic peak in the 1st cycle disappeared, which also indicates irreversible change of Co_9S_8 films. However, the anodic peaks and cathodic peaks in the 2nd-5th cycle have almost the same integrated area, implying the more reversible processes after the 1st cycles. Note that there is increased overpotential after the first cycle (Figure 5.1a), suggesting some deactivation of the newly restructured electrocatalyst. This is a common issue for electrocatalysts in alkaline condition but not our focus in this manuscript.[97, 98]

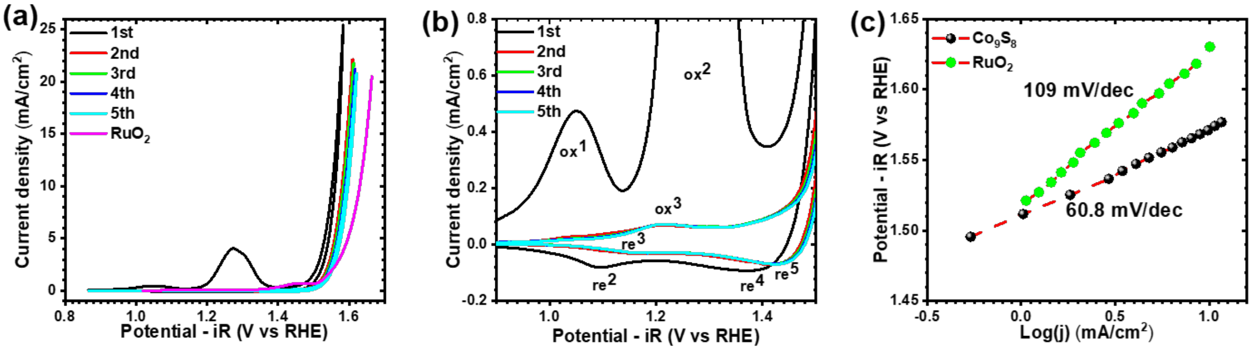

Figure 5.1 (a) First five cycles of the CV curve of the Co9S8 film at a scan rate of 2 mV/s. (b) Enlarged view of panel a indicating the oxidation and reduction peak in the first five cycles. (c) Tafel plot. (The Tafel plot was obtained by chronoamperometry measurements in steps of 10 mV, where a relaxation time of 60 s was used for each step to allow the current to achieve steady state.) All potentials are iR-compensated.

Figure 5.1c shows the Tafel plot, where the Tafel slope is a good indicator of the OER kinetics. The Tafel slope was measured to be 60.8 mV/dec, and a slope near 60 mV/dec is suggestive of a rrate-limiting chemical step following an electrochemical preequilibrium step.[99, 100] Figure 5.2a shows the representative *operando* Raman spectra taken at different applied potentials for the Co_9S_8 film on a glassy carbon electrode in 0.1 M KOH (enlarged data shown in Figure 5.6). The applied potential was stepwisely increased from 0.9 to 1.75 V and then decreased to 0.9 V (vs. RHE), with the step interval of 0.1–0.2 V. The Raman spectrum of the as-deposited Co_9S_8 film shows two distinct peaks at 338 and 403 cm^{-1}. Prolonged air exposure could oxidize Co_9S_8 to form Co_3O_4 (Figure 5.2b), and humid air could accelerate this oxidation process. Therefore, the Co_9S_8 samples were always stored under dry Ar ambient. Upon the immersion of the Co_9S_8 film in the 0.1 M KOH, the open circuit voltage (OCV) was found to gradually increase from 0.840 to 0.846 V (Figure 5.7). This OCV increase was probably due to the oxidation of Co_9S_8 in the alkaline electrolyte. (Note that the O_2 dissolved in the electrolyte was not intentionally removed.) After the OCV was stabilized, the Raman spectrum was taken on the sample. As shown in Figure5.2, no Raman peak is shown at 338 or 403 cm^{-1}, but instead the spectrum shows pronounced peaks at 482, 523, and 689 cm^{-1}, which match with the E_g, F_{2g}, and A_{1g} modes of spinel Co_3O_4, respectively.[101-104] In addition, the spectrum also shows a minor peak at 502 cm^{-1}, and this peak could be ascribed to CoO(OH), which often forms on the Co_3O_4 surface.[102, 103, 105] These results suggest that after the relaxation at OCV, the crystalline phase of Co_9S_8 disappeared, at least below the Raman detection limit, and converted to Co_3O_4 and CoO(OH). This conversion was confirmed by the XPS measurement on an OCV-relaxed sample (Figure 5.8). In fact, this spontaneous conversion is consistent with Pourbaix diagram, as Co_3O_4 is suggested by the Pourbaix diagram to be the thermodynamically stable phase in 0.1 M KOH.[99, 103, 106] Moreover, our electrochemical characterization results also indicate that the conversion from Co_9S_8 to Co_3O_4 was kinetically fast in the alkaline solution.

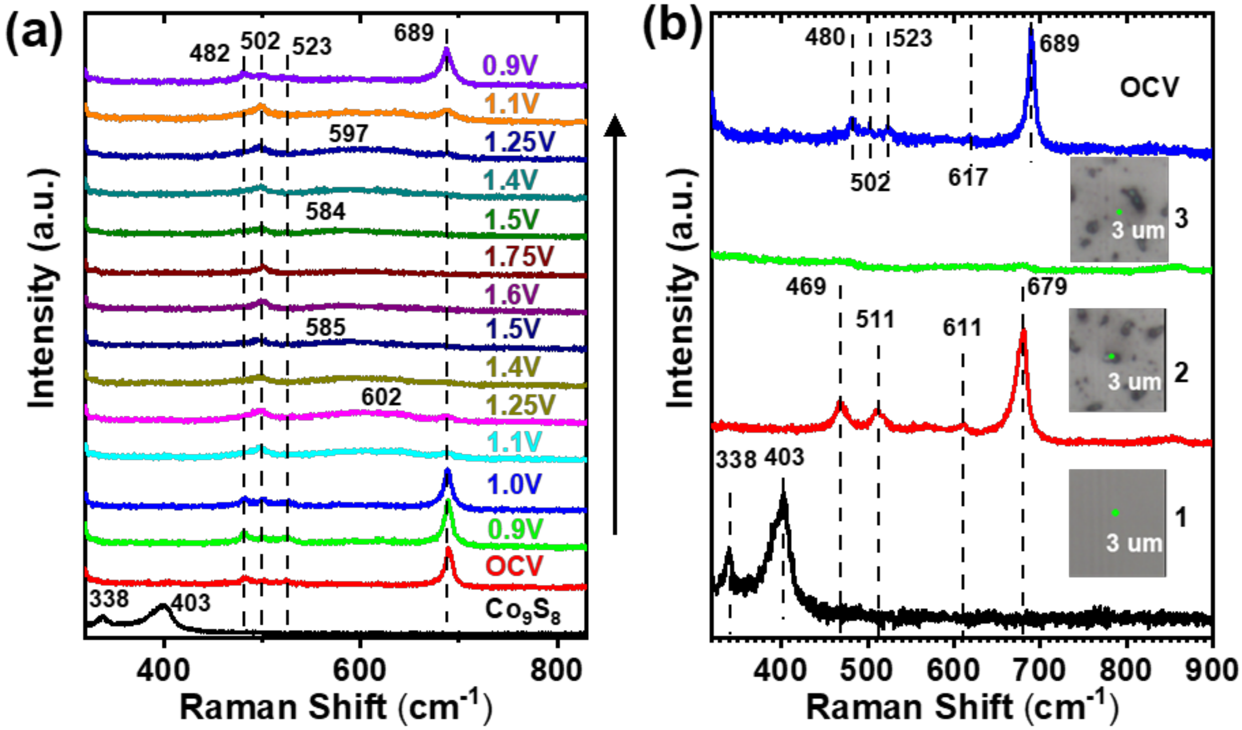

Figure 5.2 (a) *In-situ* Raman spectra for the Co_9S_8 film at various constant applied potentials. The arrow indicates the sequence of the applied potential, and each applied potential (vs. RHE) is labeled on the side of the spectrum. (b) Raman spectra of (1) an as-deposited Co_9S_8 film and (2,3) the film subject to one-week air exposure (~70% relative humidity). For the air-exposed sample, Raman spectra were taken at (2) a particle-like region and (3) a featureless region. For comparison, the plot also includes the OCV spectrum as shown in Figure 5.2a.

The above Raman features remained almost the same when a bias potential was applied and increased up to 1.0 V. However, when the potential was further raised to 1.1 V, the peaks belonging to Co_3O_4 (i.e. 482, 523, and 689 cm^{-1}) largely diminished while the peak of CoO(OH) at 502 cm^{-1} became more pronounced. In addition, a new broad band at 602 cm^{-1} appeared in the spectrum, and this broad band may also be a signature of CoO(OH)[103, 105, 107] These results suggest a change of Co_3O_4 to CoO(OH) occurred at 1.0–1.1 V, where an anodic peak was observed in the CV curve (Figure 5.1b).When the applied potential was further raised to 1.4 V and above, all the peaks belonging to Co_3O_4 disappeared, which suggests a complete conversion to CoO(OH). Notably, the band at 602 cm^{-1} gradually shifted to 585 cm^{-1} as the potential increased from 1.25 to

1.5 V. The red-shift of the 602 cm^{-1} band is suggested to be indicative of the oxidation of the Co(II) and Co(III) toward Co(IV).[103] This assignment is also consistent with the CV curve, where a pronounced anodic peak was observed at 1.35 V.[87, 108] Notably, the redshift of the band occurred monotonically, which suggests that the entire CoOOH was oxidized collectively. Above 1.6 V, substantial oxygen bubbling appeared.

When the applied potential was stepwisely reduced, the Raman spectra indicate that the structural change of the cobalt compound was generally reversed: the 585 cm^{-1} band shifted back to 597 cm^{-1} and the Co_3O_4 peaks reappeared when the potential was reduced below 1.4 V. However, this change was not completely reversible as the width of the 689 cm^{-1} peak was larger than that at the beginning (FWHM increased from 8.7 to 11.7 cm^{-1}). The increased peak width is suggestive of lowered crystallinity, which can be attributed to the irreversible crystalline-to-amorphous structure changes. At high applied potential (1.6 V vs RHE and above) part of CoOOH becomes amorphous and cannot be converted back to crystalline Co_3O_4 when the applied voltage is reduced. This crystalline-to-amorphous structure change was also supported by the grazing incidence diffraction (GID) in Figure 5.13.

To further confirm the change of Co_9S_8 oxidization state and local structure, we conducted *operando* XAS. Since the thin film Co_9S_8 was grown by atomic layer deposition (ALD) with ~ 20 nm, all signals collected by the bulk sensitive XAS can be used to determine the surface local structures. The pristine material Co_9S_8 shows an oxidization state around +2.1 (Table 5.3), and it is very unstable in the electrolyte (Figure 5.3a), which is also confirmed by *operando* Raman results and Pourbaix diagram.[99, 103, 106] Once Co_9S_8 was immersed into the electrolyte, it was oxidized from +2.1 to +2.2, which were calculated based on the linear relationship between the Co XANES edge and oxidation states (Figure 5.3b). As the applied voltage is increased, the Co

XANES edges shift to higher energy, suggesting the further oxidizing of Co. It was found that Co was first oxidized to +2.5 followed by an oxidation to +2.9, +3.1, and finally slightly above +3.2 at a potential of 1.75 (vs. RHE) (Figure 3b & Table 5.3). When decreasing the applied potential back to open circle voltage (OCV, approximately 0.88V vs RHE), the oxidation state of Co has a descending trend. The change of Co oxidization state is consistent with the *operando* Raman experiments, which also reflect as the reduction and oxidization peaks in the CV measurements. However, incomplete reversibility is also observed, as the oxidation state of Co after returning to OCV is around +2.7 which is higher than that of the pristine sample. This irreversibility change could be caused by the transformation of Co^{2+} to Co^{3+} coordinated in octahedral sites in low crystallinity $Co_xO_y(OH)_z$, and some of these octahedral sites could be non-reducible Co^{3+} which do not play a role in catalyzing OER.[87] The formation of the low activity Co^{3+} site could be the reason for the instability of Co_9S_8.

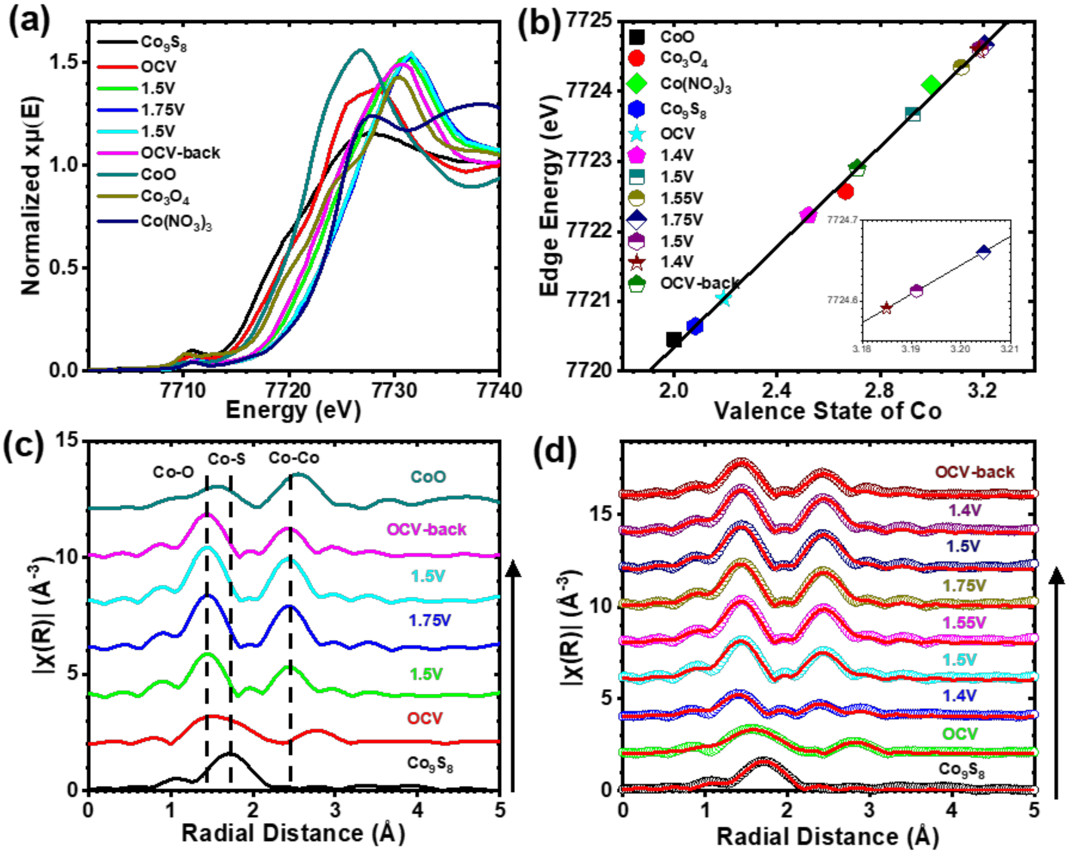

Figure 5.3 Operando Co K-edge XANES measurements under electrocatalytic reaction conditions of Co9S8. (b) Calculated Co valence state on operando Co K-edge XAS by using an integral method (V is in unit of V vs RHE), Inset shows an enlarged view. (c) Operando Co K edge EXAFS measurements of Co_9S_8. (d) model-based fitting results of *Operando* EXAFS of Co_9S_8.

The evolution of Co local structures under the applied potential is shown in Figure 5.3c. At OCV, the phase-uncorrected EXAFS of the catalyst has a board peak around 1.55 Å that should be resulted from the combination of Co-O and Co-S scattering comparing to the EXAFS of CoO and Co_9S_8 standards, suggesting the mixture of the two phases. This is consistent with XANES at OCV that shows the partial oxidation of Co. As the applied potential is increased, the first peak in EXAFS (around 1.72 Å in OCV) shifts to 1.42 Å that is caused by the predominant Co-O scattering. The structure of original Co_9S_8 catalyst is likely to be gradually oxidized to CoO_x structure, which is also consistent with Raman spectroscopy findings. To generate further insights into the structural evolution of Co_9S_8 during the reaction, we performed model-based EXAFS fitting by combining

Co_9S_8 and CoO crystal structures (Figure 5.3d, S5.6-S5.7; Table 5.4-5.5).[1, 67] The fitted results clearly show an increasing trend of both Co-O and Co-Co coordination numbers (CNs) as the applied potential is increased, and Co-S coordination mostly exists in the pristine state and at OCV. Only a small fraction (around 13.3% compared with pristine Co_9S_8) of Co-S coordination is left at 1.4V vs RHE. This small amount of remaining Co-S may be due to the incomplete S leaching at OCV. As the applied potential is increased, the conversion of Co-S coordination to Co-O coordination takes place. It is noted that the first shell of Co atoms around 1.9 Å reaches the fully coordination with 6 Co-O bonds, representing an octahedron (CoO_6) that can be found in spinel Co_3O_4 or CoOOH as confirmed by the Raman experiments. However, the second shell Co-O-Co is under coordinated (less than 12 in CoO or slightly less than 6 in CoOOH), suggesting a cluster-like structure without long-range ordering.[1, 109, 110] When the applied potential is increased, Co-O and Co-Co CNs increase, contributing to the increase of the oxidation state of Co. When reversing the applied potential back to OCV, the Co-O and Co-Co CNs decrease, and both stay undercoordinated, indicating the formation of reduced Co nanoparticle.

The loss of long-range ordering of the *in-situ* generated CoO_x is further confirmed by *operando* XRR and GID measurements on Co_9S_8 thin films (See supporting information for details). For the as-deposited catalyst thin film, *Kiessig* fringes in XRR can be observed, suggesting a smooth surface. As the applied potential is increased, these fringes quickly disappear, indicating the surface was roughing. No crystalline diffraction peaks are identified from GID, confirming the formation of short-range ordering materials in OER, which is consistent with the lack of long-range ordering indicated by EXAFS and could also be the reason of irreversible reconstruction observed by *operando* XAS.

Although Co_9S_8 catalyst goes through both compositional and long-range-to-short-range ordering structural evolution, the CoO_6 octahedron is remained during OER. In our previous studies, the octahedral site in the spinel structure is the active site for OER,[22, 111] and e_g theory for transition metal perovskite oxides is based on the electronic structure of metal-oxygen octahedron.[16] However, some octahedral Co^{3+} in CoOOH is not reducible and has low activity in OER, and some are reducible and has high activity in OER.[87] Therefore, it is possible that CoO_6 is the smallest structure building block and the surface Co atoms bridged by di-μ-oxo bonds in these octahedrons are active sites as the catalytic center for this type of metal X-ides. To verify our hypothesis, we performed DFT calculations by building a small cluster of CoO_6 as shown in Figure 5.13. Except for di-μ-oxo site, the octahedral coordination geometry of each peripheral Co ion is completed by nonbridging oxygen ligands (including water and hydroxide). The average Co-O bond length between the central Co atom and the surrounding six O atoms is 1.86 Å, which is in accordance with the experimental result (Co-O: 1.90 Å for the first shell). This result also indicates that the central Co atom is +3 oxidation state with the same as the Co of octahedral site in Co_3O_4.[112] Recent studies have shown that the oxidation states of surface atoms are determined using atomic projections of the magnetic moments and the smaller the magnetic moments of the atoms, the higher the oxidation states.[113] In $Co_7O_{24}H_{23}$ cluster model, it is estimated that there are two oxidation states of Co, namely, Co^{3+} and Co^{2+}, due to the overlap between the atom-projected magnetic moments of Co ions in various oxidation states. Next, the possible OER mechanisms are explored in alkaline environment. For path1 in Figure 5.4a and Table 5.7, *Step #1*: The reaction starts from the deprotonation of *OH to generate a H_2O molecule and the *O group by the addition of the first OH^- at Co2 site, in which the oxidation states of Co1 and Co2 atoms remain unchanged. *Step #2*: The *O combined with the second OH^- as initial state is optimized into a di-μ-OH and the released O_2 molecular, as shown in Figure 4b. Both the Co1 and Co2 ions (+3) are reduced to +2. *Step #3*: The third OH^- is preferentially adsorbed on Co2 site due to coordinative unsaturation of Co2, causing Co1 to be oxidized to +3 and no change in the Co2 oxidation state (+2). *Step #4*: the deprotonation of di-μ-OH completes the 4-electron transfer of OER by the addition of the fourth OH^-. In this reaction step, all the Co ions return to the initial oxidation states (see Figure 5.14). For path2 in Figure 5.4c and Table 5.8, *Step #1*: The reaction begins with the first OH^- adsorbed at the di-μ-O site to form di-μ-O_2 and $*H_2O$ at Co2 site, in which the Co1 and Co2 ions are reduced from the +3 to the +2 oxidation state. *Step #2*: The deprotonation of $*H_2O$ at Co2 site produces an *OH by the addition of the second OH^-. At the same time, di-μ-O_2 spontaneously desorbs in the optimization process, as show in Figure 5.4d. *Step #3*: The third OH^- is preferentially adsorbed on the bridge site between Co1 and Co2. *Step #4*: This step is the same as the fourth step of path 1. The above results indicate that the adsorption of different intermediates can cause the continuous changes in the oxidation states of Co ions to determine the active sites in OER Analyzing the free energy diagrams at the equilibrium potential of 0.402 V, the rate determination step is the deprotonations of *OH at Co2 site for path1 and di-μ-OH site for path2 with an overpotential of 0.86 V and 0.69 V, respectively. Our results reveal that the *OH at the bridge site is more prone to deprotonation than that of the OH adsorbed on Co ions, and Co atoms bridged by di-μ-oxo bonds with di-μ-oxo are active sites in OER, and Co1-Co2 with di-μ-oxo are active sites in OER, which is in good agreement with the experimental results. Note that our calculation only chooses Co1 and Co2 as the reaction surfaces. Other surface atoms such as Co3, Co5, Co6 and Co7 have the equivalent roles after deprotonations at di-μ-OH sites. In addition, no change of Co (Co4) at the central of the nanocluster confirm our hypothesis that only surface Co atoms bridged by di-μ-oxo bonds are active in reactions. These results also imply that the overall activity and stability of the *in-situ* generated CoO_x could be related to the size of the nanocluster. The continuous growth of the CoO_x nanocluster leads to the low ratio of active surface di-μ-oxo Co-Co motifs and high amount of inactive central Co atoms, which affect the long-term performance of the metal X-ides.

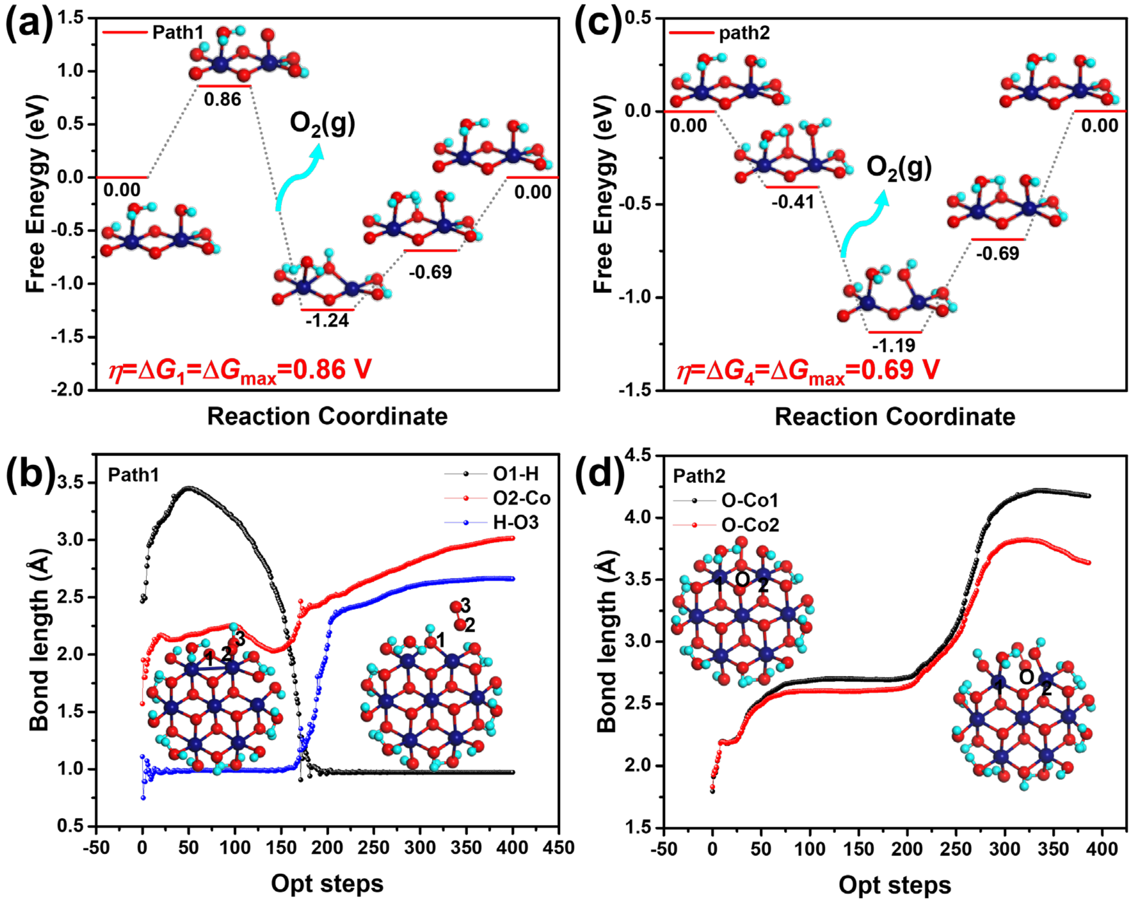

Figure 5.4 The Gibbs free energy diagrams of OER at all possible active sites on the Co7O24H23 cluster. (a) path1 and (c) path2 in alkaline environment. Structural optimization of the second electrochemical step to produce O_2(g) on the Co7O24H23 cluster, (b) Changes of O1-H, O2-Co and H-O3 bond lengths in path1. (d) Changes of O-Co1 and O-Co2 bond lengths in path2. Red, cyan and blue spheres indicate O, H and Co atoms, respectively.

5.4. Conclusions

In summary, we have combined *operando* XAS, XRR, and Raman spectroscopy together with DFT calculations to reveal the restructuring processes of Co_9S_8 as one example of metal X-ides for OER. We have shown that the Co_9S_8 transfers into an entirely different CoO_x structure consists of edging sharing octahedral CoO_6 nanoclusters with di-μ-oxo Co-Co motifs on surface, which is the true catalytic center. The atop oxygen in CoO_6 octahedrons can adsorb reaction intermediates (OH*) and the bridging Co-O-Co in di-μ-oxo Co-Co motifs can be easily broken to form the vacancies or unsaturated coordination to facilitate the OER. Comparing with the edge-sharing octahedral CoO_6 in bulk Co_3O_4, the restructuring Co_9S_8 in OER induces crystalline-to-amorphous conversion in addition to Co_9S_8-to-CoO_x change. The composition and structure transformation in this restructuring process is beneficial to provide abundant active sites for the OER. The leaching of S ions also helps create the vacancies in the materials to facilitate the participation of lattice oxygen in the OER, which is another benefit compared other CoO_x bulk materials. Our results demonstrate that for catalysts that experience complicated restructuring processes, *operando* characterizations are essential to understanding the reaction kinetics and related reaction mechanisms. This strategy is also reflected in a recent study using *operando* surface-enhanced Raman spectroscopy to point out the formation of super cobalt oxide as the possible reaction center.[100] In addition, previous studies (Table 1) also suggests some other metal X-ides such as metal X-ides (X = C, P, N, Se, etc.), which may also be either completed or partially oxidized to metal oxide[88] during the OER. If such restructuring occurs in metal X-ides, the metal-oxygen octahedral clusters with surface di-μ-oxo metal-metal motifs could act as the active sites to promote the OER. Although some work has shown that the metal X-ides may not undergo any restructuring, the surface-active sites may still contain such building block similar to what we found here. For example, Nath's group has shown that nickel telluride will form some telluride-based edge sharing octahedra instead of oxygen-based octahedra structure, which favors the OH adsorbing for OER. Therefore, we come up with a new hypothesize that the edge sharing octahedra units are the basic reaction center for OER in the alkaline medium, but the composition in the units can be modified to enhance the OER performance. Our findings and strategy on identifying metal X-ides' active site could aid future research in the development of advanced electrocatalysts for the energy conversion and storage systems.

5.5. Supplementary Experimental Method

5.5.1. ALD Growth of Co_9S_8

Atomic layer deposition (ALD) of Co_9S_8 thin films was performed in a home-built tubular ALD reactor at 120°C, using bis(*N,N'*-di-*tert*-butylacetamidinato)cobalt(II) and H_2S as the precursors.[114, 115] The films (used for electrochemical and *operando* XAS measurements) were deposited on flat glassy carbon (GC) substrates (1×1 cm^2). The thickness for all the Co_9S_8 films was about 20 nm, as measured by X-ray fluorescence (Rigaku, ZSX Primus II). Co_9S_8 films with the same thickness were deposited on Si substrates for *operando* Raman and XRR measurements.

5.5.2. Electrochemical Measurements

The electrochemical measurements were performed in an electrochemical workstation (CHI 660E), using a standard three-electrode configuration. An ALD-Co_9S_8-coated GC electrode was used as the working electrode. Hg/HgO and Pt electrodes were used as the reference and counter electrodes, respectively, and 0.1 M KOH aqueous solution was used as the electrolyte. All the electrochemical measurements were taken at room temperature. The RuO_2 benchmarking electrode was made by drop-casting 16 μL of a RuO_2 ink onto a GC electrode to afford a RuO_2 loading amount of 0.20 mg cm^{-2}. The RuO_2 ink was made by ultrasonically dispersing 5 mg RuO_2 (99.9 wt%, Aladdin) in a mixed solution of 0.1 mL Nafion, 0.9 mL water, and 1.0 mL ethanol.

5.5.3. Operando Raman Measurement

Operando Raman spectra were taken by a confocal Raman microscope (LabRAM HR Evolution, Horiba), using 532 nm laser for excitation (Laser Quantum Ltd). The laser was focused by a 100× objective lens to reach a spot size of 1 μm, and the laser power was about 100 mW. A custom-designed electrochemical cell was used for the *operando* Raman measurement. The GC working electrode was sealed in the cell, which had a transparent window to allow the laser light to pass through. Ag/AgCl and Pt wire electrodes were used as the reference and counter electrodes, respectively, and 0.1 M KOH was used as the electrolyte. During the *operando* Raman experiment, each Raman spectrum was taken at a constant applied potential. The applied potential was stepwise changed from 0.9 to 1.75 V (vs. RHE). At each potential step, the applied potential was first held for 5 min to stabilize the electrochemical current before collecting the Raman spectra. The current was monitored by the electrochemical workstation (CHI 660E). The acquisition of each Raman spectrum took about 5 min. The Raman spectra were also taken at multiple locations on the sample, and no appreciable difference was observed, which suggests negligible sample damage by the Raman laser.

5.5.4. Operando surface X-ray scattering experiments

Operando XRR experiments were carried out at 12-ID-D, Advanced Photon Source (APS) at Argonne National Laboratory (ANL) using an eight-circle diffractometer equipped with a Pilatus 100k 2D detector. Specular reflectivity data were collected to probe surface normal properties such as surface roughness and electron density contrast for Co_9S_8 thin films. To perform *operando* measurements, thin film material was mounted on a custom designed electrochemical cell with Pt wire and Ag/AgCl as the counter and reference electrodes and electrochemical data acquisition was done by using a Gamry Reference-600 electrochemical workstation under a O_2 gas flow of 30 sccm in 0.1 M KOH. Several potential points were selected based on preliminary cyclic voltammetry (CV) runs and were held for at least 15 minutes before acquiring XRR data. XRR data were background subtracted and corrected for active area and polarization. Moreover, out-of-plane gracing-incidence diffraction (GID) measurements were done after the electrochemical experiments to probe the surface-specific crystal structure of the film.

5.5.5. Operando X-ray Absorption Spectroscopy

Operando XAS experiments were carried out at 5BM-D, APS of Argonne National Laboratory. Both Co K-edge XANES and EXAFS were measured under fluorescence mode by a Vortex ME4 detector. 20 nm thick Co_9S_8 was deposited by the same ALD process on carbon fiber paper with 100-µm thickness as the working electrode. Pt wire and Ag/AgCl were used as counter electrode and reference electrode, respectively. All three electrodes were mounted on a custom-designed *operando* XAS fluorescence cell,[1, 35, 82] and the electrochemical measurements were done by a Gamry Reference-600 electrochemical workstation under O_2 gas flow at 30 sccm in 0.1M KOH electrolyte. Several potential points were selected and held for at least 15 min to collect data to make sure completed reaction. All XAS data analysis were performed with Athena software package to extract XANES and EXAFS. Fourier Transform of Co K-edge EXAFS was performed by using Hanning window function with k-weights of 2. For model-based EXAFS analysis, all the scattering paths were generated by the FEFF calculation function in Artemis based on the crystal structure of CoO and Co_9S_8. The generated scattering paths were then calibrated by performing the FEFFIT of the EXAFS data of the CoO reference sample, mainly to obtain the amplitude reduction factor (S_0^2) values. With S_0^2 (0.71) known, all EXAFS data of the catalyst materials were fitted with such generated amplitudes using co-refinement fitting. All those EXAFS fittings are done with k-range from 3 to 12 $Å^{-1}$. An integral method was used to determine the Co oxidization state with Co K-edge XANES.

5.5.6. DFT calculations

All spin-polarized DFT calculations were performed using the revised Perdew−Burke−Ernzerhof (RPBE)[116] exchange correlation functional of the generalized gradient approximation (GGA) as implemented in VASP 5.4.4.[117, 118] The projector augmented-wave (PAW)[119] method was used to describe the core−valence interaction and a plane-wave cutoff energy was set to 400 eV to approximate the valence electron densities. The DFT+U method with an effective coulomb integral (U – J) of 5.02 eV for the octahedral sites in bulk Co_3O_4 was adopted to describe the strong correlation of the localized Co 3d states.[112] Convergence was achieved when all atomic forces and energies were below 0.01 eV/Å and 10^{-5} eV, respectively. The dispersion correction was considered by using the DFT-D3[120] method to describe the van der Waals interactions. An edge-sharing molecular cobaltate cluster (MCC)[121] was utilized to simulate the molecular dimensions of our experimental CoO_6 octahedral clusters, namely, $Co_7O_{24}H_{23}$. For isolated cluster, interactions between periodic images are negligible in a 15×15×15 $Å^3$ unit cell and thus single gamma-point sampling was used for Brillouin zone integration. Details on the calculations of Gibbs free energies are presented in the Supporting Information.

5.6. Supplementary discussion and results

5.6.1. Raman spectrum of Co_9S_8

The Raman spectrum of the as-deposited Co_9S_8 film shows two distinct peaks at 338 and 403 cm^{-1} (Figure 5.2). Air exposure could oxidize Co_9S_8 to afford Co_3O_4. As shown in Figure 2b, after one-week exposure in air with about 70% relative humidity, the surface of the film formed some particle-like features, which could be observed under an optical microscope. The Raman spectra taken on these particle-like features show pronounced peaks at 465, 511, 611, and 679 cm^{-1}, which could be assigned to the spinel Co_3O_4.[101-104] Therefore, the particle-like features were probably the spinel Co_3O_4, which was the oxidation product of Co_9S_8. For those featureless regions, the Raman spectra show only barely-visible weak peaks at ca. 471 and 680 cm^{-1}. These peaks were probably also from the spinel Co_3O_4 but perhaps with small crystallites and/or poor crystallinity. Possibly, in these featureless regions some intermediate oxidation compounds may have formed, such as cobalt oxysulfide (CoO_xS_y), with amorphous or poorly crystalline structures. Nevertheless, we did not observe any peaks of Co_9S_8 at 338 or 403 cm^{-1}, which suggests that the crystalline phase of Co_9S_8 disappeared after the prolonged air exposure.

5.6.2. The calculation details of Gibbs free energies

Computational hydrogen electrode (CHE)[122] model was used to calculate the Gibbs free energy change for OER elementary reactions. At electrode potential U = 0 V (vs. reversible hydrogen electrode, RHE), the Gibbs free energy change (ΔG) can be calculated by

$$\Delta G = \Delta E + \Delta E_{\mathrm{ZPE}} - T\Delta S \qquad (1)$$

where ΔE is the energy difference between the products and reactants from DFT computations; ΔE_{ZPE} and ΔS are the changes in zero-point energies and entropy, respectively, which are obtained from the vibrational frequency calculations; T is the temperature at 298 K. The energy corrections of gas-phase species in this work, including zero point energies and entropies, are listed in Table 4. The overpotential (η), $\eta = \Delta G_{\max}/e$. where $\Delta G_{\max}$ is the maximum free energy change among all elementary steps under standard electrode (reduction) potential.

The oxygen evolution reaction follows four elementary steps in alkaline:

Path1:

$$*(O_{(bri)} + OH_{(Co)}) + OH^- \rightarrow *(O_{(bri)} + O_{(Co)}) + H_2O(l) + e^- \quad (2)$$

$$*(O_{(bri)} + O_{(Co)}) + OH^- \rightarrow *(OH_{(bri)} + {}_{(Co)}) + O_2(g) + e^- \quad (3)$$

$$*(OH_{(bri)} + {}_{(Co)}) + OH^- \rightarrow *(OH_{(bri)} + OH_{(Co)}) + e^- \quad (4)$$

$$*(OH_{(bri)} + OH_{(Co)}) + OH^- \rightarrow *(O_{(bri)} + OH_{(Co)}) + H_2O(l) + e^- \quad (5)$$

Path2:

$$*(O_{(bri)} + OH_{(Co)}) + OH^- \rightarrow *(O_{2(bri)} + H_2O_{(Co)}) + e^- \quad (6)$$

$$*(O_{2(bri)} + H_2O_{(Co)}) + OH^- \rightarrow *({}_{(bri)} + OH_{(Co)}) + O_2(g) + H_2O(l) + e^- \quad (7)$$

$$*({}_{(bri)} + OH_{(Co)}) + OH^- \rightarrow *(OH_{(bri)} + OH_{(Co)}) + e^- \quad (8)$$

$$*(OH_{(bri)} + OH_{(Co)}) + OH^- \rightarrow *(O_{(bri)} + OH_{(Co)}) + H_2O(l) + e^- \quad (9)$$

the ΔG for each step can be calculated by:

Path1:

$$\Delta G_1 = G(*O_{(bri)} + O_{(Co)}) + \mu(H_2O(l)) + \mu e^- - (G(*O_{(bri)} + OH_{(Co)}) + \mu(OH^-)) \quad (10)$$

$$\Delta G_2 = G(*OH_{(bri)} + {}_{(Co)}) + \mu(O_2(g)) + \mu e^- - (G(*O_{(bri)} + O_{(Co)}) + \mu(OH^-)) \quad (11)$$

$$\Delta G_3 = G(*OH_{(bri)} + OH_{(Co)}) + \mu e^- - (G(*OH_{(bri)} + {}_{(Co)}) + \mu(OH^-)) \quad (12)$$

$$\Delta G_4 = G(*O_{(bri)} + OH_{(Co)}) + \mu(H_2O(l)) + \mu e^- - (G(*OH_{(bri)} + OH_{(Co)}) + \mu(OH^-)) \quad (13)$$

Path2:

$$\Delta G_1 = G(*O_{2(bri)} + H_2O_{(Co)}) + \mu e^- - (G(*O_{(bri)} + OH_{(Co)}) + \mu(OH^-)) \quad (14)$$

$$\Delta G_2 = G(*({}_{(bri)} + OH_{(Co)}) + \mu(O_2(g)) + \mu(H_2O(l)) + \mu e^- - (G(*O_{2(bri)} + H_2O_{(Co)}) + \mu(OH^-)) \quad (15)$$

$\Delta G_3 = G(*OH_{(bri)} + OH_{(Co)}) + \mu e^- - (G(*(_{(bri)} + OH_{(Co)}) + \mu(OH^-))$ (16)

$\Delta G_4 = G(*O_{(bri)} + OH_{(Co)}) + \mu(H_2O(l)) + \mu e^- - (G(*OH_{(bri)} + OH_{(Co)}) + \mu(OH^-))$ (17)

Therefore, the free energy change of each elementary reaction can be calculated using i) the chemical potentials of hydroxide, electron, liquid water and oxygen molecule ($\mu(OH^-)$, μe^-, $\mu(H_2O(l))$, and $\mu(O_2(g))$, and ii) the free energies of each intermediate on the surface of catalyst (*). Then, we calculated the chemical potential of hydroxides and electrons with reference to Lee's work in alkaline environment.[123] $\mu e^- - \mu(OH^-) - eU = 9.65$ eV was obtained by repeated calculations under standard electrode (reduction) potential ($E^0 = 0.402$ V) at T=298.15 K.

5.6.3. Ex-situ XPS Characterization

For the Co_9S_8 before OER, the Co 2p spectrum shows two peaks at 778.4 and 793.4 eV, which match well with CoS_x. The presence of O signal in the survey spectrum is because of surface air oxidation, as the sample was exposed to air before the XPS test. The S 2p spectrum shows two peaks at 162.4 and 167.5 eV, which correspond to CoS_x and some oxidized S-containing surface species (e.g. sulfite), respectively. After OER, all S signals disappeared. The Co 2p spectrum shows two peaks at 780.2 and 795.2 eV, which are consistent with the formation of CoO_x.

5.6.4. Operando XRR Characterization

To observe the evolution of surface normal properties such as the surface roughness, electron density contrast in successive layers in Co_9S_8 thin films as the electrochemical reaction propagates, *operando* specular XRR measurements were obtained using a custom-built electrochemical cell. The comparison of XRR spectra subjected to background subtraction, active area correction and polarization correction at different potential points are shown in Figure 5.13a. We can observe characteristic Keissig fringes that are formed by the interference of X-rays scattered by substrate and different layers in the thin film. The critical angle for total external reflection of X-rays shows a sudden decrease from the as-prepared film to others. This is reasonable because the inclusion of an additional electrolyte layer between the topmost layer of the film and the vacuum lowers the contrast, hence lowering the critical angle. Moreover, the amplitude of the Keissig fringes decreases as the reaction proceeds that is indicative of reduction of electron density contrast between adjacent layers. In addition, as shown in the inset to Figure 5.13a, the XRR spectra decays more as the reaction proceeds which shows that the surface roughness of the film increases as the reaction propagates. These observations are reasonable for an electrocatalytic reaction which typically involves reactions that can alter the surface morphology. Especially, in this instance, the inter-diffusion of ions/atoms between adjacent layers in the film could lower the electron density contrast between adjacent layers and surface dissolution and formation of vacancies can increase surface roughness of the film. According to EXAFS fitting results, the catalyst is likely to form undercoordinated Co nanoparticles with 6 coordinated Co-O and Co-Co bonds after the reaction. The GID spectrum for the Co_9S_8 film after the *operando* measurements shows further evidence to this with clearly visible broad peaks that are indicative of amorphous nature or the presence of nanoparticles.

5.7. Supplementary Figures for electrochemical characterization, Raman, XPS, XAS, and DFT

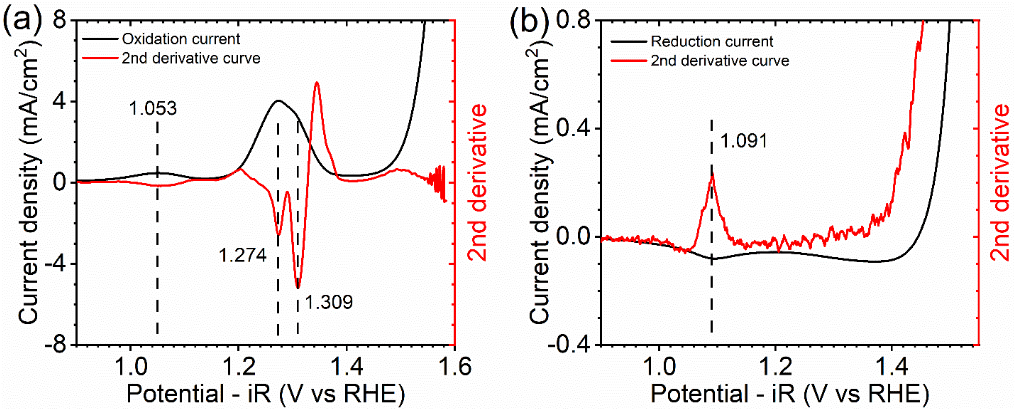

Figure 5.5 (a) 2nd derivative for the 1st cycle oxidization current. (b) 2nd derivative for the 1st cycle reduction current.

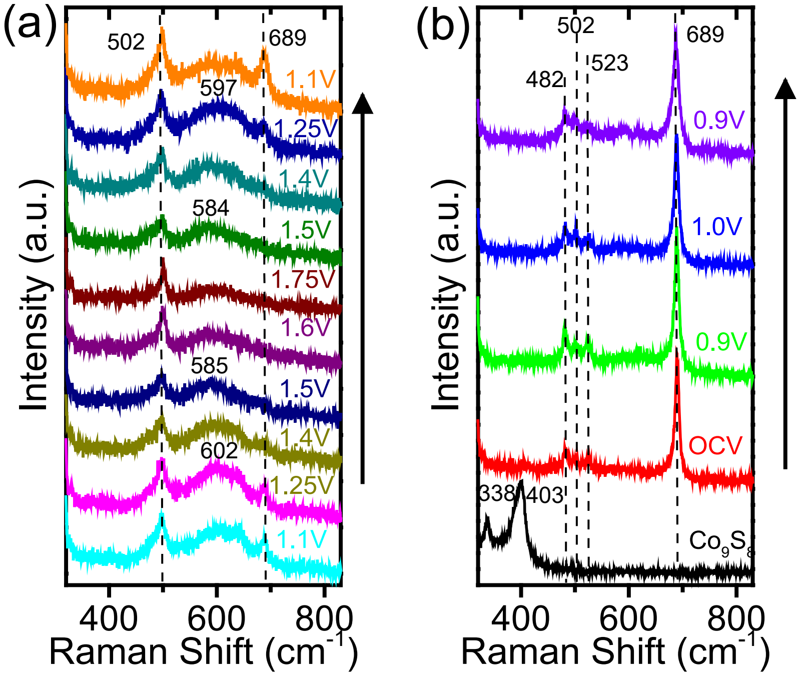

Figure 5.6 In-situ Raman spectra for the Co_9S_8 film at various constant applied potentials. The arrow indicates the sequence of the applied potential and each applied potential (vs. RHE) is labeled on the side of the spectrum.

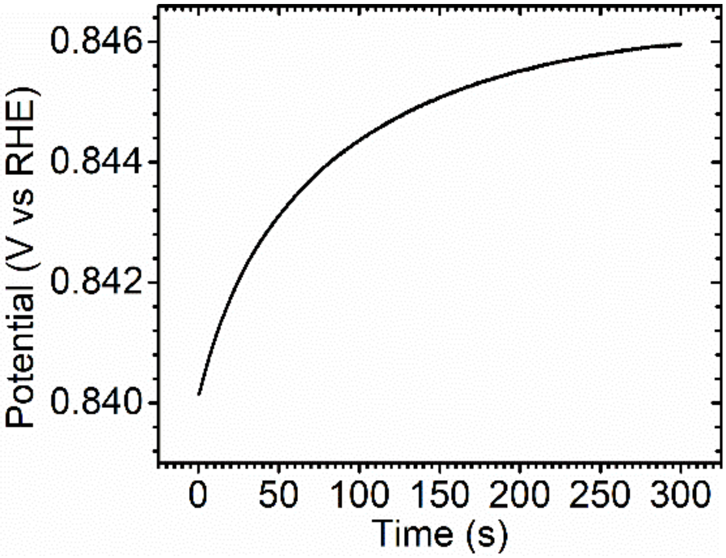

Figure 5.7 Trace of OCV upon the immersion of Co_9S_8 in 0.1 M KOH

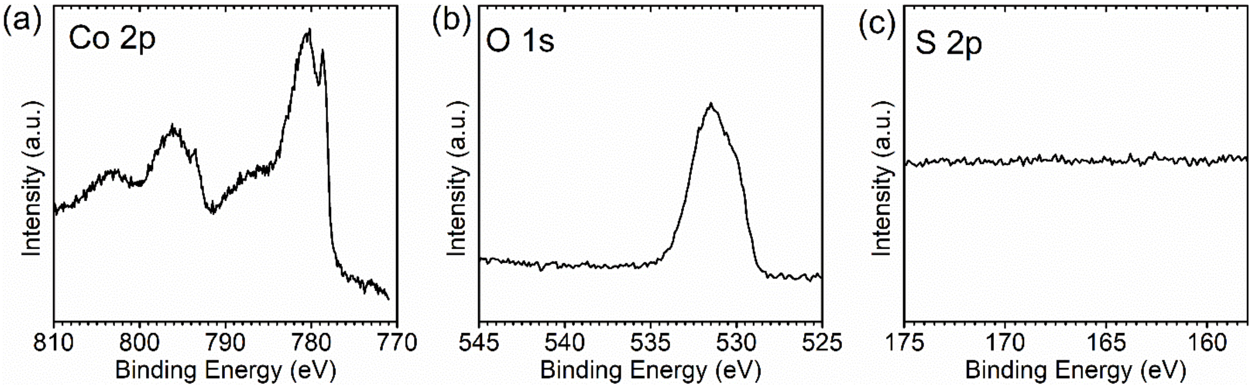

Figure 5.8 XPS spectra of the Co_9S_8 film after resting in 0.1 M KOH at OCV for 3h. (a) Co 2p, (b) O 1s, and (c) S 2p spectra.

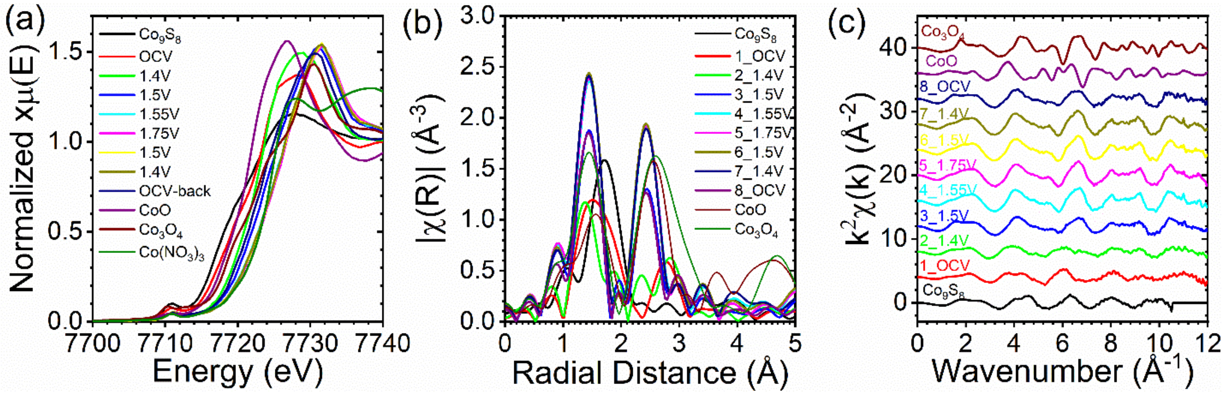

Figure 5.9 *Operando* Co K-edge (a) XANES (b) EXAFS R-space (c) EXAFS k-space measurements under electrocatalytic reaction conditions of Co_9S_8.

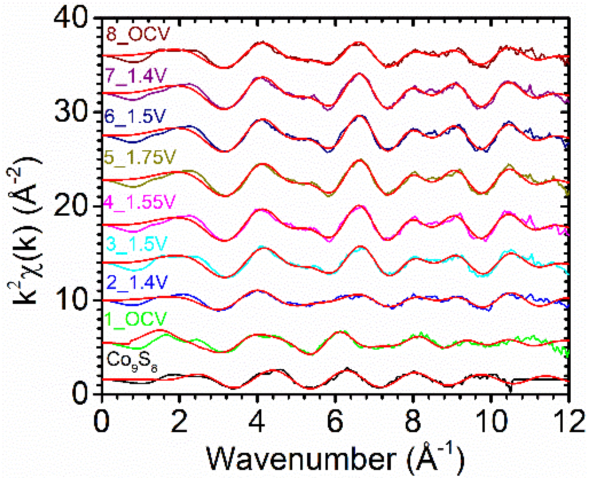

Figure 5.10 model-based fitting results of *operando* EXAFS k-space of Co_9S_8 under electrocatalytic reaction conditions

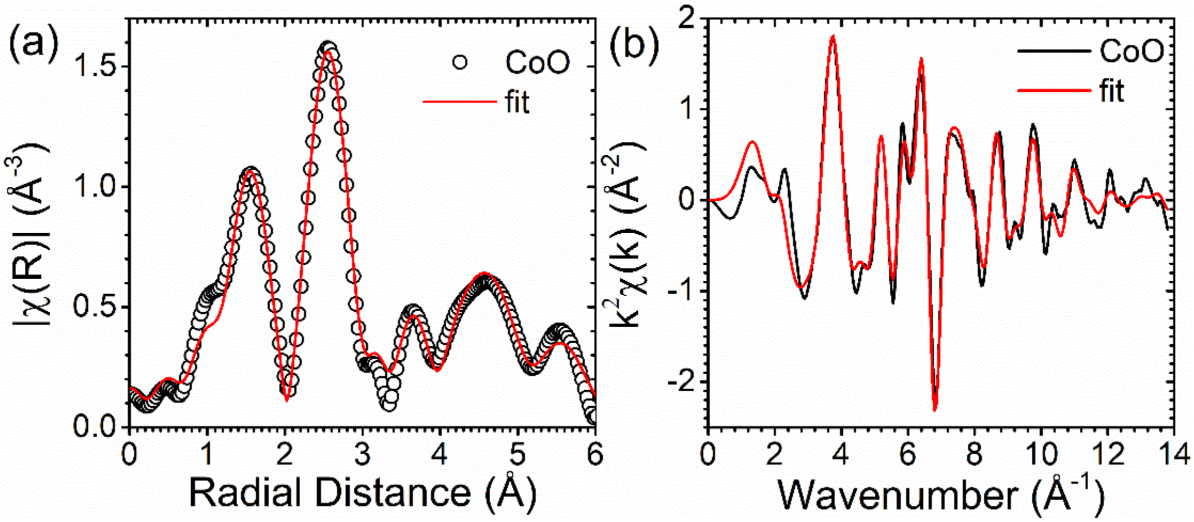

Figure 5.11 model-based fitting results of EXAFS (a) R-space and (b) k-space of standard CoO

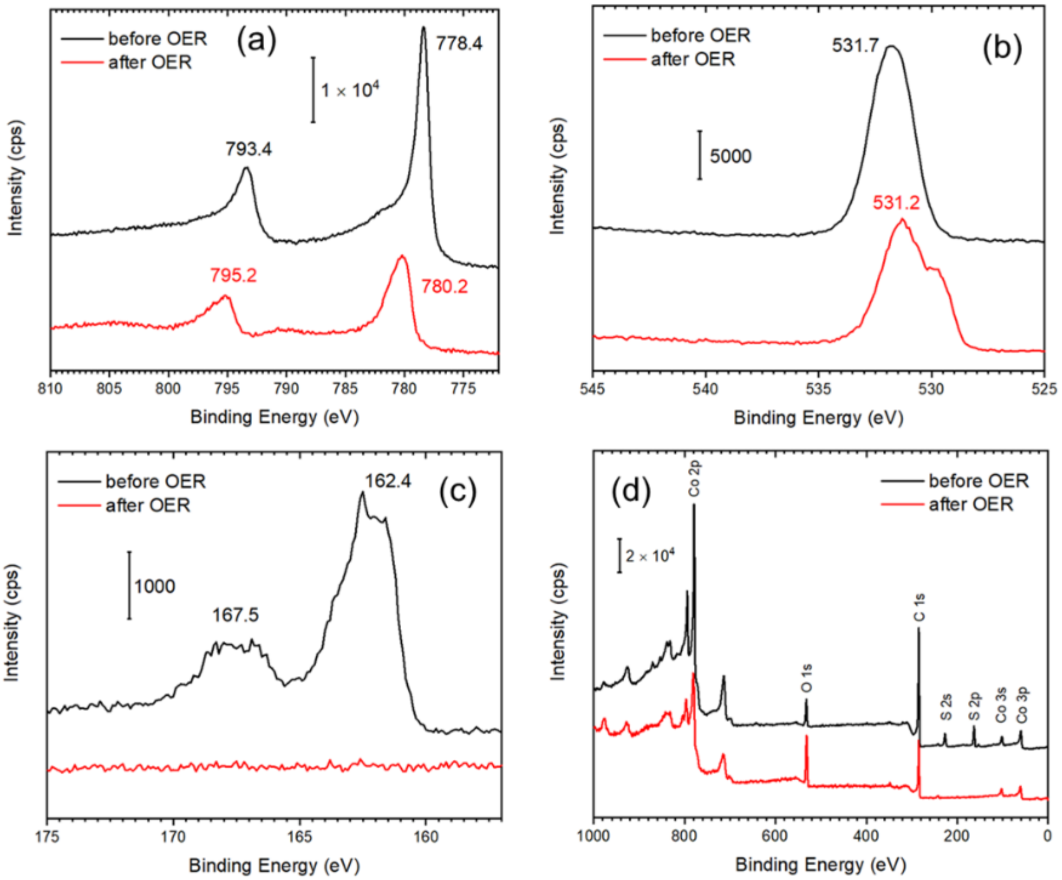

Figure 5.12 Comparison of the XPS data of Co_9S_8 before and after the OER test. (a) Co 2p, (b) O 1s, (c) S 2p, and (d) survey spectra.

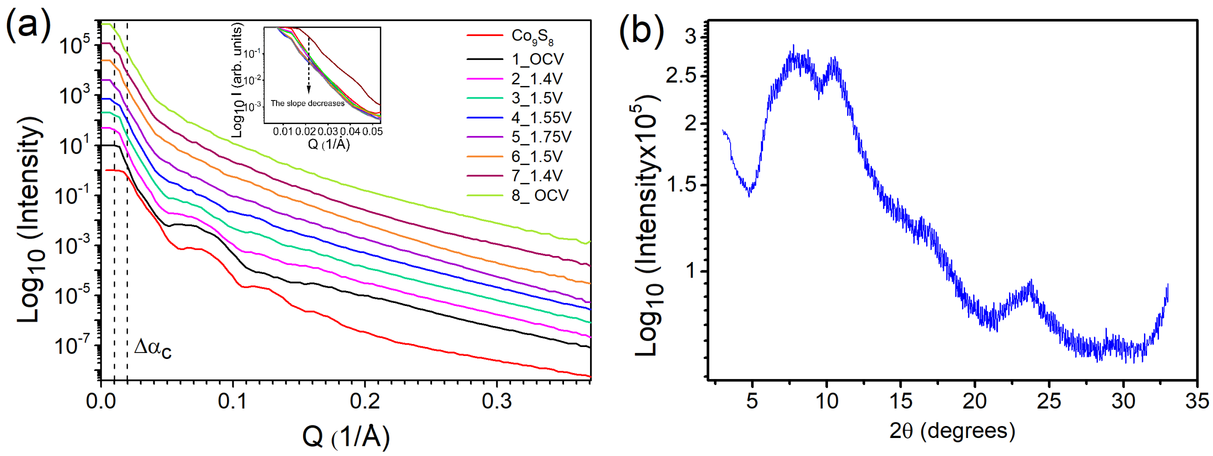

Figure 5.13 (a) Comparison of *operando* specular X-ray reflectivity spectra obtained at different potential points (OCV is around 0.8V vs RHE) for the Co_9S_8 film. The inset to graph with a zoomed region shows the increase in decay of the spectra as the reaction propagates. (b) In-plane Grazing Incidence Diffraction (GID) spectrum for the Co_9S_8 film after electrochemical tests.

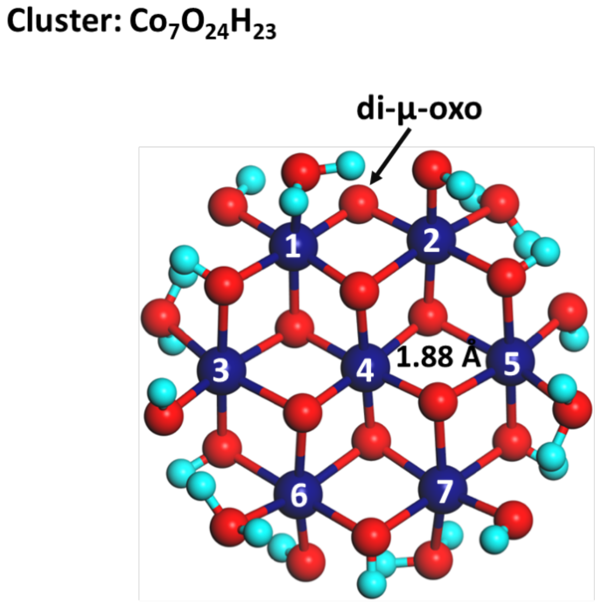

Atom	magnetic moment(μ_B)	Oxidation state
Co1	2.521	3
Co2	2.670	3
Co3	3.201	2
Co4	2.002	3
Co5	3.200	2
Co6	3.196	2
Co7	3.200	2
Average	2.856	2.43

Figure 5.14 Schematic diagram of the calculated Co-oxo/hydroxo clusters model and the magnetic moments and oxidation states of Co atoms in $Co_7O_{24}H_{23}$ cluster.

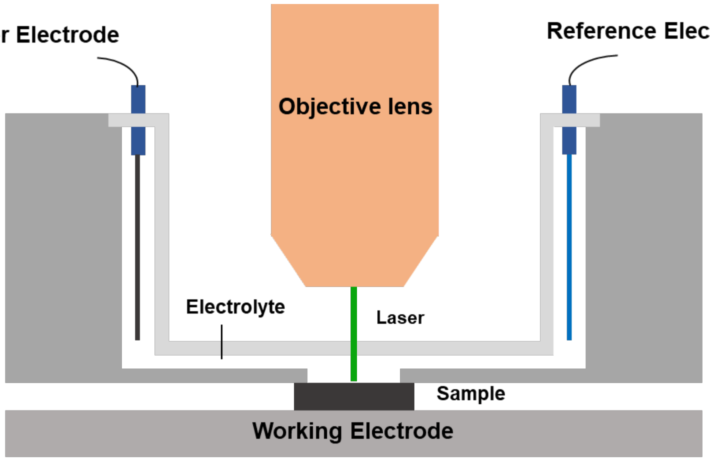

Figure 5.15 Schematic diagram of the *operando* Raman setup.

5.8. Supplementary Tables for reference materials, XAS fitting, and DFT

Table 5.1 a group of transition metal X-ide catalysts (X: C, P, N, S, etc.) restructuring during the OER

Catalysts	Form	Reaction condition (pH)	Reaction intermediates	Ref
$FeNi_3N$	Nanoparticle	14	FeNi oxides/hydroxides	124
FeP	Powder	14	Fe oxides/hydroxides	98
FeS	Nanosheet	14	Fe oxides/hydroxides	125
$FeSe_2$	Nanoparticle	14	Fe oxides/hydroxides	126
Co_3C	Nanoparticle	14	Co oxides/hydroxides	65
Co_4N	Nanowire	13	Co oxides/hydroxides	127
CoP	Thin film	N/A	Co oxides/hydroxides	88
CoS_2	Thin film	14	Co oxides/hydroxides	128
$CoSe_2$	Thin film	14	Co oxides/hydroxides	128

$CoTe_2$	Thin film	14	Co oxides/hydroxides	128
Ni_3C	Nanoparticle	14	Ni oxides/hydroxides	129
Ni_3N	Nanosheet	14	Ni oxides/hydroxides	130
NiP_x	Thin film	14	Ni oxides/hydroxides	131
NiS_x	Thin film	14	Ni oxides/hydroxides	131
$NiSe_x$	Thin film	14	Ni oxides/hydroxides	131
NiTe	Thin film	14	Ni oxides/hydroxides	132

Table 5.2 Proposed different OER rection center for FeOOH, CoOOH and NiOOH

Materials	**Reaction sites**	**Ref**
FeOOH	oxygen vacancy-modified CoOOH edge-sharing FeO6 octahedra	133-135
CoOOH	oxygen vacancy-modified CoOOH Co(IV) species CoO2 (Co superoxides) Co(III)/Co(IV) redox Co(II)/Co(III) redox Cobalt-Oxo Core Co oxo/hydroxo clusters composed of edge-sharing CoO6 octahedra μ 2-OH-bridged Co(II)/Co(III) ion clusters	87, 88, 108, 136-140
NiOOH	four-coordinated Ni site edge-sharing NiO6 octahedra Ni(III)/Ni(IV) redox Ni(II)/Ni(III) redox	134, 141-147

Table 5.3 Co oxidization state for operando Co K-edge XAS (V is in unit of V vs RHE)

Applied Potential (V vs. RHE)	Oxidization State
Pristine	2.1
OCV	2.2

1.40	2.5
1.50	2.9
1.55	3.1
1.75	3.2
1.50	3.2
1.40	3.2
-0.09	2.7

Table 5.4 Fitting parameters of the co-refined EXAFS spectra of standard CoO. CN: coordination number; R: distance; E_0: energy shift; σ^2: mean-square disorder). The numbers in the parentheses are the last digit error.

Scattering Path	**CN**	**R(Å)**	**E_0(eV)**	**σ^2(Å^2)**	**R-factor**
			Co Metal		
Co-O	6	2.092(0.0012)	-2.05(0.94)	0.0075(0.0021)	0.011
Co-Co	12	3.006(0.0009)		0.0105(0.0013)	
Co-O-Co	12	4.293(0.0017)		0.0163(0.0031)	
Co-O-O	48	4.450(0.0018)		0.0007(0.0044)	
Co-O	24	4.809(0.0019)		0.0178(0.0277)	
Co-O-Co	48	4.991(0.0020)		0.0039(0.0114)	
Co-O-O	48	4.991(0.0020)		0.0070(0.0409)	
Co-Co	24	5.258(0.0021)		0.0012(0.0033)	
Co-Co-Co	24	6.071(0.0024(		0.0126(0.0036)	
Co-Co-Co-Co	12	6.071(0.0024)		0.0172(0.0082)	

Table 5.5 Fitting parameters of the co-refined EXAFS spectra of standard Co9S8 at different potentials (CN: coordination number; R: distance; E0: energy shift; σ2: mean-square disorder). The numbers in the parentheses are the last digit error. The numbers in the parentheses with yellow label are the full error.

Scattering Path	**CN**	**R(Å)**	**E_0(eV)**	**σ^2(Å^2)**	**R-factor**
		Co9S8			
Co-S	6	2.205(0.012)	-4.60(1.62)	0.0029(0.0015)	0.035

1_OCV					
Co-O	13.9(2.6)	2.036(0.017)	1.95(2.25)	0.0008(0.0005)	0.028
Co-Co	2.5(1.5)	2.878(0.024)	1.95(2.25)	0.0045(0.0051)	
Co-S	22.9(4.3)	2.222(0.015)	-2.28(2.08)	0.0054(0.0007)	
2_1.4V					
Co-O	3.2(0.03)	1.917(0.015)	-7.67(2.15)	0.0007(0.0006)	0.039
Co-S	0.8(0.03)	2.345(0.036)		0.0008(0.0006)	
Co-Co	1.5(0.03)	2.809(0.018)		0.0007(0.0006)	
Co-O	1.7(0.03)	3.441(0.022)		0.0008(0.0006)	
3_1.5V					
Co-O	5.3(0.4)	1.896(0.007)	-4.84(0.52)	0.0008(0.0001)	0.015
Co-Co	4.2(0.7)	2.831(0.009)		0.0035(0.0009)	
4_1.55V					
Co-O	5.7(0.3)	1.902(0.005)	-4.84(0.52)	0.0008(0.0001)	0.015
Co-Co	5.4(0.7)	2.847(0.006)		0.0035(0.0009)	
5_1.75V					
Co-O	5.8(0.3)	1.898(0.005)	-4.84(0.52)	0.0008(0.0001)	0.015
Co-Co	5.4(0.7)	2.844(0.006)		0.0035(0.0009)	
6_1.5V					
Co-O	5.9(0.3)	1.901(0.006)	-4.84(0.52)	0.0008(0.0001)	0.015
Co-Co	5.4(0.7)	2.845(0.007)		0.0035(0.0009)	
7_1.4V					
Co-O	5.8(0.4)	1.902(0.006)	-4.84(0.52)	0.0008(0.0001)	0.015
Co-Co	5.4(0.7)	2.846(0.007)		0.0035(0.0009)	
8_OCV					

Co-O	4.6(0.4)	1.909(0.008)	-4.84(0.52)	0.0008(0.0001)	0.015
Co-Co	3.4(0.7)	2.840(0.011)		0.0035(0.0009)	

Table 5.6 Total energies (E, eV) of H_2O, H_2 and adsorbates and zero point energy (ZPE) corrections and entropic contributions (TS) to the free energies.

Species	E (eV)	ZPE (eV)	TS (eV)
H_2O (0.035 bar)	−14.22	0.56	0.67
H_2	−6.76	0.27	0.41
	Path1		
$*(\mathrm{O_{(bri)}} + \mathrm{OH_{(Co)}})$		0.43	0.13
$*(\mathrm{O_{(bri)}} + \mathrm{O_{(Co)}})$		0.13	0.11
$*(\mathrm{OH_{(bri)}} + {}_{\mathrm{(Co)}})$		0.36	0.09
$*(\mathrm{OH_{(bri)}} + \mathrm{OH_{(Co)}})$			
	Path2		
$*(\mathrm{O_{2(bri)}} + \mathrm{H_2O_{(Co)}})$		0.79	0.23
$*({}_{\mathrm{(bri)}} + \mathrm{OH_{(Co)}})$		0.36	0.09

Table 5.7 Atom-projected magnetic moments (μB) for Co atoms in the path1.

Co Atom	$*(\mathrm{O_{(bri)}} + \mathrm{OH_{(Co)}})$	$*(\mathrm{O_{(bri)}} + \mathrm{O_{(Co)}})$	$*(\mathrm{OH_{(bri)}} + {}_{\mathrm{(Co)}})$	$*(\mathrm{OH_{(bri)}} + \mathrm{OH_{(Co)}})$
1	2.521	2.567	3.181	2.729
2	2.670	2.483	3.134	3.194
3	3.201	3.199	3.198	3.197
4	2.002	2.005	1.996	2.039
5	3.200	3.209	3.195	3.202
6	3.196	3.195	3.200	3.199
7	3.200	3.199	3.203	3.187

Table 5.8 Atom-projected magnetic moments (μB) for Co atoms in the path2.

Co Atom	$*(\mathrm{O_{(bri)}} + \mathrm{OH_{(Co)}})$	$*(\mathrm{O_{2(bri)}} + \mathrm{H_2O_{(Co)}})$	$*({}_{\mathrm{(bri)}} + \mathrm{OH_{(Co)}})$	$*(\mathrm{OH_{(bri)}} + \mathrm{OH_{(Co)}})$
1	2.521	3.108	3.165	2.729
2	2.670	3.139	3.160	3.194
3	3.201	3.195	3.192	3.197
4	2.002	2.038	2.028	2.039
5	3.200	3.193	3.197	3.202
6	3.196	3.198	3.199	3.199
7	3.200	3.202	3.203	3.187

5.9 Acknowledgement

This work is supported by the startup funding from Oregon State University (OSU) and NNCI-2025489. The synchrotron X-ray characterization is supported by the National Science Foundation

(CBET-1949870 and DMR-1832803). W. S. S. acknowledges the support from PNNL-OSU Distinguished Graduate Research Fellowship. XAS measurements were done at 5-BM-D of DND-CAT, which is supported through E. I. duPont de Nemours & Co., Northwestern University, and The Dow Chemical Company. XRR measurements were done at 12 ID-D. The use of Advanced Photon Source (APS) of Argonne National Laboratory (ANL) for synchrotron measurements is supported by Department of Energy under Contract No. DE-AC02-06CH11357. The DFT calculations are supported by The National Science Foundation (Grant No. 1900039) and the Welch Foundation (Grant No. F-1959-20180324). The calculations used computational resources of (TG-CHE190065), National Renewable Energy Lab, Argonne National Lab, and Oak Ridge National Lab. X.W. acknowledgements the support from NSFC (51961165105), Guangdong Basic and Applied Basic Research Foundation (2020B1515120039), and Shenzhen Fundamental Research Program (JCYJ20200109110628172).

Chapter 6. Ultrahigh Oxygen Evolution Reaction Activity Achieved Using Ir single atoms on amorphous CoOx nanosheets

Ultrahigh Oxygen Evolution Reaction Activity Achieved Using Ir single atoms on amorphous CoO_x nanosheets

Chao Cai[a,b#], Maoyu Wang[c#], Shaobo Han[a,b#], Qi Wang,[b] Qing Zhang,[b] Yuanmin Zhu,[b] Xuming Yang,[b] Duojie Wu,[b] Xiaotao Zu[a]*, George E. Sterbinsky,[d] Zhenxing Feng[c]*, Meng Gu[b]*

[a] School of Physical, University of Electronic Science and Technology of China, Chengdu 610054, China.

[b] Department of Materials Science and Engineering, Southern University of Science and Technology, Shenzhen, 518055, China

[c] School of Chemical, Biological, and Environmental Engineering, Oregon State University, Corvallis, OR 97331

[d]Advanced Photon Source Argonne National Laboratory, Argonne, IL 60431, USA

[#]: Equally Contributed First Author

*: Corresponding Author

Reprinted with permission from ACS Catal. 11,1, 123-130

6.1. Abstract

Developing efficient electrocatalysts for oxygen evolution reaction (OER) is important for renewable energy storage. Here we design high-density Ir single-atom catalysts supported by CoO_x amorphous nanosheets (ANSs) for OER. Experimental results show that Ir single-atoms are anchored by abundant surface-absorbed O in CoO_x ANSs. The Ir single-atom catalysts possess ultrahigh mass activity that is 160-fold of commercial IrO_2. The OER of $IrCoO_x$ ANSs reached a record-low onset overpotential of less than 30 mV. The *in-situ* X-ray absorption spectroscopy reveals that the Ir-O-Co pairs directly boosted the OER efficiency and enhanced the Ir stability.

6.2. Introduction

Industrial chemical reactions utilize catalysts to increase the production rate of a desired product and reduce the energy costs.[1,2] Therefore, developing efficient catalysts can reduce energy costs and selectively promote the production of value-added chemicals.[3] Sluggish kinetics of the oxygen evolution reaction (OER) seriously limit the practical applications of hydrogen production[4-9] and carbon dioxide reduction in aqueous media.[10] To date, Ru/Ir –based metals and their oxides are well known as the most efficient OER catalysts.[11] However, their scarcity and high price are major barriers for their application.[12,13] Therefore, exploring highly efficient catalysts with reduced Ru/Ir usage is necessary for practical applications. Many attempts have been made, such as alloying with transition metals, core-shell approaches, and single atom catalysts (SACs), etc.[14]

The high free energy of single atoms in SACs ensures an easier adsorption process than traditional nano-catalysts, further boosting their catalytic activity.[15] Adsorption of molecules on surfaces often leads to varied coordination environments of SACs during pre-activation or initial reaction processes.[13,16,17] The synergistic Ru sites in the $Ru\text{-}FeCo(OH)_x$ SACs are the active reaction sites, which significantly promote the OER activity.[18] Unfortunately, once the highly active SACs are put in liquid, the active atoms often suffer from surface etching, subsequently leading to activity loss.[19] In addition, the harsh reaction may trigger the aggregation of SACs, which weakens the synergistic effect between single atoms and the matrix and lowers the adsorption-desorption efficiency as well as catalytic activity/stability.[15,20,21] Moreover, harsh catalytic reaction leads to the structural transformation and breakdown of catalysts.[22,23] Currently, these issues of SACs still delay their various practical applications.

In this work, we synthesized CoO_x ANSs doped with Ir single atoms. The $IrCoO_x$ ANSs possess a thickness of *ca.* 1 nm and ultrahigh surface areas of 213 m^2/g. By tuning the stoichiometric ratio of Ir/Co, we achieve the highest mass OER activity reported to date. We used a combination of aberration corrected scanning transmission electron microscopy (STEM) and *in-situ* X-ray absorption spectroscopy (XAS) to understand the catalyst structure and related reaction mechanisms.

6.3. Structural characterizations

As $Ir_1Co_{13.3}O_{20.1}$-(Sample 4) ANSs with an Ir/Co ratio of ~7:93 shows the best activity among all $IrCoO_x$ ANSs (Figure 6.5), we focus on the structural characterization of $Ir_1Co_{13.3}O_{20.1}$. The relative Ir/Co ratio determined by inductively coupled plasma optical emission spectroscopy (ICP-OES) is shown in Table 1. Scanning electron microscopy (SEM), transmission electron microscopy (TEM), double Cs-corrected STEM, powder X-ray diffraction (XRD), and N_2 adsorption-desorption tests are employed to clarify the morphology and structure of as-prepared $Ir_1Co_{13.3}O_{20.1}$ ANSs. The Ir1Co13.3O20.1 $Ir_1Co_{13.3}O_{20.1}$ possess a hierarchical microstructure composed of curly nanosheets (Figure 6.1a). The selected area electron diffraction (SAED) in the inset of Figure 6.1b reveals the amorphous nature of the as-prepared $Ir_1Co_{13.3}O_{20.1}$. The amorphous feature of $Ir_1Co_{13.3}O_{20.1}$is also verified by XRD (Figure 6.6). Benefitting from the ultrathin feature of CoO_x ANSs (thickness of ca. 1 nm, as shown in Figure 6.1c), the $Ir_1Co_{13.3}O_{20.1}$ possess large surface area determined to be *ca.* 213.3 m^2/g (Figure 6.7). This is larger than many reported metal oxides and carbon-based materials, which typically have surface areas smaller than 180 m^2/g.[24-26] The formation of an ultrathin layered structure can be attributed to the hexadecyltrimethylammonium bromide (CTAB, 0.05 M) and the fast precipitation caused by $NaBH_4$. The concentration of CTAB is *ca.* 2.5-fold of its second critical micelle concentration (0.02 M), leading to the formation of a CTAB bilayer structure in solution.[27] The $NaBH_4$ leads the fast formation of CoB_x that can be easily oxidized by O and H_2O. Therefore the newborn CoB_x in the system tends to form CoO_x amorphous layers.[28] Without CTAB use in reaction solution, the precipitation can be CoB_x amorphous particles.[29]

The catalytic activity is impacted by the distribution and structure of Ir atoms. Thus we used STEM to clarify the nanostructure of $Ir_1Co_{13.3}O_{20.1}$. The low magnification STEM image finds no Ir particles in $Ir_1Co_{13.3}O_{20.1}$ (Figure 6.1d). The energy dispersive spectrum (EDS) at low magnification demonstrates a homogeneous distribution of Ir, Co and O (Figure 6.1e). The high magnification STEM image demonstrates the monodispersed Ir single atoms (brighten spots marked by red circles in Figure 6.1f) on CoO_x ANSs. Unlike multi-step preparation of Au single atoms on $FeNi(OH)_x$ nanosheets[16] and Pt single atoms on CeO_2[15], $Ir_1Co_{13.3}O_{20.1}$ ANSs are prepared in one pot. Due to the large surface area and high chemical activity, two-dimensional CoO_x ANSs may adsorb many oxygen atoms on the surface. Surface-absorbed oxygen and surfactant could be the major contributors to the formation of Ir single atoms. The anchoring of Ir atoms can occur at the sites with surface-absorbed oxygen, because the strong bonding between O and Ir firmly captures the Ir atoms. The surfactant can avoid the regrowth of Ir.[26] Using this idea, we successfully synthesized $IrNiO_x$ ANSs using an approach similar to $IrCoO_x$ ANSs (Figure 6.8). This result demonstrates that reduction of noble metal on ANSs with abundant surface-absorbed oxygen could be a reliable approach to synthesize various SACs.

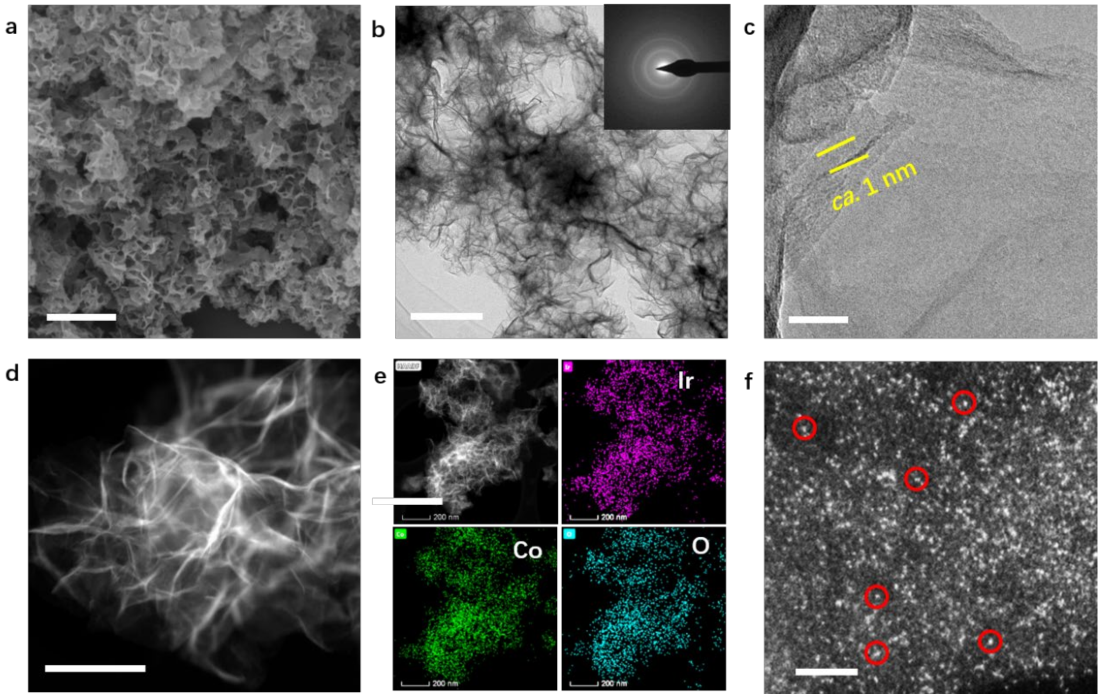

Figure 6.1 Structural characterization of $Ir_1Co_{13.3}O_{20.1}$. SEM image (a), low magnification TEM image (b), high magnification TEM image (c), HAADF image (d), EDS mapping (e), and high magnification HAADF image (f) of $Ir_1Co_{13.3}O_{20.1}$. Ir single atoms anchor on CoO_x ANSs and are well dispersed. The brighten spots in Figure 1f correspond to Ir atoms, exemplified by red circles marked. Scale bar in a-f is 1 um, 200 nm, 20 nm, 100 nm, 500 nm, and 1 nm, respectively.

6.4. Electrochemical performance

We use Ir/Co-based materials as catalysts for OER in 1 M KOH using a three-electrode system. Relative data is shown in Figure 6.2, where all the current densities are normalized by the geometric area of the glass carbon electrode (GCE). The $Ir_1Co_{13.3}O_{20.1}$ possess the highest OER activity among all reported OER catalysts to date (Table 6.2). As shown in Figure 6.2a, $Ir_1Co_{13.3}O_{20.1}$ exhibit much better OER activity than CoO_x ANSs and IrO_2 over the entire potential range. Figure 6.2b shows that $Ir_1Co_{13.3}O_{20.1}$ require a low overpotential of only 152±5.2 mV to achieve 10 mA/cm^2, much lower than pure CoO_x ANSs (330.1±12.5 mV) and commercial IrO_2 (320.0±10.1 mV). The $Ir_1Co_{13.3}O_{20.1}$ have the lowest Tafel slope (*ca.* 60.5±2.8 mV/dec) among these prepared catalysts, and it is even lower than commercial IrO_2 (*ca.* 65.6±2.7 mV/dec) as shown in Figure 6.2c. At 1.485 V *v.s.* RHE, the $Ir_1Co_{13.3}O_{20.1}$ possess specific current density of 160 mA/cm^2 (mass activity of 1412 A/g), which is 160-fold of commercial IrO_2 (1 mA/cm^2). To clarify the origin of such superior OER activity, we employed double layer capacitance (C_{dl}) testing to calculate the electrochemical surface area (ECSA) (Figure 6.2e), which is sensitive to the exposed atoms in OER. The $Ir_1Co_{13.3}O_{20.1}$ possess *ca.* 2-fold ECSA value compared to CoO_x ANSs, while surprisingly the catalytic activity of $Ir_1Co_{13.3}O_{20.1}$ is *ca.* 40-fold of CoO_x ANSs (Figure 6.2d). These results show that its high OER activity is due to not only increasing ECSA, but also the high intrinsic activity of Ir for OER. The high intrinsic catalytic activity of Ir is further promoted by the support of ultrathin amorphous CoO_x ANSs (Figure 6.9). The commercial IrO_2 sample is also characterized using STEM, XRD, and XPS (Figure 6.10 to 6.12) to get further insights regarding to its physical structure, morphology, and surface chemistry information. By carefully comparing the polarization curve that normalized by surface area and ECSA (Figure 6.12a&b), we found that the $Ir_1Co_{13.3}O_{20.1}$ possess higher intrinsic activity than IrO_2. The aggregated Ir on CoO_x NSs shows better OER activity than pure CoO_x NSs, but lower than $Ir_1Co_{13.3}O_{20.1}$ (Figure 6.12c&d), confirming that the OER activity in Ir/Co NSs is critically affected by the Ir local environments and morphology. In addition, as shown in Figure 6.2f, electrochemical impedance spectrum (EIS) results testify that the charge transport resistance (R_{ct}) of $Ir_1Co_{13.3}O_{20.1}$ is 11.8±0.9 Ω, which is around 1/5 of CoO_x ANSs (56.4±2.3 Ω). Therefore, such superior OER activity of $Ir_1Co_{13.3}O_{20.1}$ can be ascribed to the largely enhanced chemical active areas, high intrinsic activity of Ir on CoO_x ANSs, and super-fast charge transport from catalysts to support.

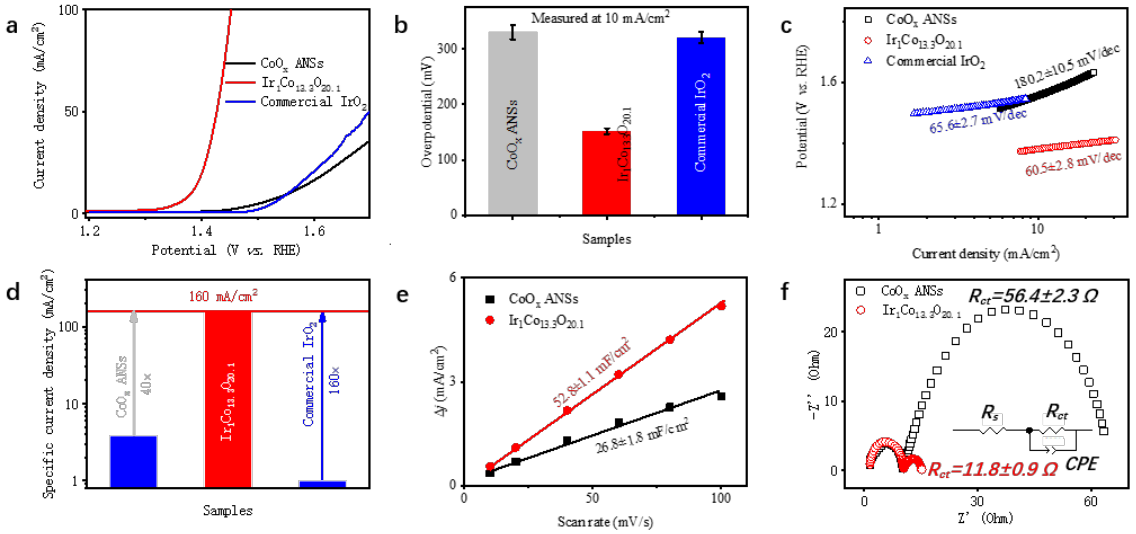

Figure 6.2 Electrochemical characterizations of different catalysts. Polarization curves (a), collection of overpotential at 10 mA/cm^2 (b), Tafel plots (c), specific current density at 1.485 V *v.s.* RHE (d), C_{dl} values (e), and Nyquist plots (f) of CoO_x ANSs and $Ir_1Co_{13.3}O_{20.1}$ ANSs. The inset in Figure 2f is the equivalent circuits for R_{ct} calculation. The $Ir_1Co_{13.3}O_{20.1}$ANSs show far better OER performance than CoO_x ANSs and IrO_2.

6.5. Surface chemistry and structures

The abundant surface-absorbed oxygen and strong synergistic effect between Ir and Co also play critical roles in promoting OER activity. X-ray photoelectron spectroscopy (XPS) was used to clarify the valence of metal cations and oxygen states in $Ir_1Co_{13.3}O_{20.1}$ and CoO_x ANSs (Figure 6.3). Figure 6.3a shows the survey spectrum of $Ir_1Co_{13.3}O_{20.1}$ and CoO_x ANSs. Figure 6.3b collects the fitted Co 2p fine spectrum. The fitted peaks of Co $2p_{3/2}$ correspond to Co^{3+} (*ca.* 780.2 eV) and Co^{2+} (*ca.* 782.1 eV), respectively.[25,26] The increased Co^{3+}/Co^{2+} ratio after Ir loading indicates also a higher content of oxygen, forming possible Ir-O-Co pairs. Figure 6.3c shows the normalized O 1s spectrum. The O 1s spectra extends at high energy edge in $Ir_1Co_{13.3}O_{20.1}$. The adsorption O ratio is increased after Ir loading (Figure 6.13a), which can increase average valence of catalysts, and thus enhance the OER activity.[30] To further clarify the oxidation state of Co and O, the electron energy loss spectroscopy (EELS) is carried out for determining the average valance of Co and O/Co ratio, as shown in Figure 3d. The valence states of Co can be measured according to the L_3/L_2 white-line intensity ratios. In our work, the integrated L_3/L_2 ratio of $Ir_1Co_{13.3}O_{20.1}$ is calculated to be 2.78 which is lower than 3.13 of CoO_x ANSs, verifying the higher Co valence. Correspondingly, the O *K* edge fine structure also shows a higher pre-peak intensity after Ir-loading on the CoOx sample, which correspondingly indicates a higher Co oxidation state. The integrated area ratio of O *K*-edge to Co *L*-edge in $Ir_1Co_{13.3}O_{20.1}$ is calculated to be 0.38, which is larger than that of CoO_x ANSs (0.27), confirming a higher O content in $Ir_1Co_{13.3}O_{20.1}$. This result is also verified by the EDS results, where the O/Co ratio is increased after Ir loading (Figure 6.13b). In this case, the Ir loading can increase the oxidation states of cobalt and promote the O adsorption efficiency in $Ir_1Co_{13.3}O_{20.1}$. The peaks of Ir corresponding to various valance are shown in Ir 4f spectra (Figure 6.11c).[31] The existence of Ir^{3+}/Ir^{4+} cations demonstrates a strong bonding between Ir and oxygen atoms including the ones absorbed on the surface. These results show that controlling the amount of surface-absorbed oxygen atoms can be fine-tuned by changing Ir loading. In the same time, Ir loading modulates the Co valence of the matrix.

To get further insight into the Ir-Co coupling effect, *in-situ* XAS was carried out to identify the oxidization state and local coordination environment of Ir and Co. Co K-edge X-ray absorption near edge structure (XANES) shows that Co cations in CoO_x ANSs have a slightly higher oxidation state than crystalline CoO (Figure 6.3e and S6.10), which is caused by abundant surface-absorbed oxygen environments in CoO_x ANSs. The surface-absorbed oxygen can firmly capture Ir atoms by forming Ir-O-Co bonding that is confirmed by extended X-ray absorption fine structure (EXAFS) fitting. Interestingly, Co is further oxidized after loading Ir on the surface. With surface-absorbed oxygen increasing, the higher electron affinity of Ir (150 kJ/mol) than Co (64 kJ/mol) leads to re-centering of the 3d electrons of Co towards Ir via Ir-O-Co bonding. To probe the exact local structure, the EXAFS measurements are performed (shown in Figure 6.3f) and the model-based analysis (Figure 6.13 and Table 6.3) confirms that CoO_x ANSs have surface-absorbed oxygen due to less Co-Co scattering paths which are related to Co-O-Co bond in the CoO model (also seen at 2Å < R < 3 Å region in Figure 6.3f) comparing with crystalline CoO.

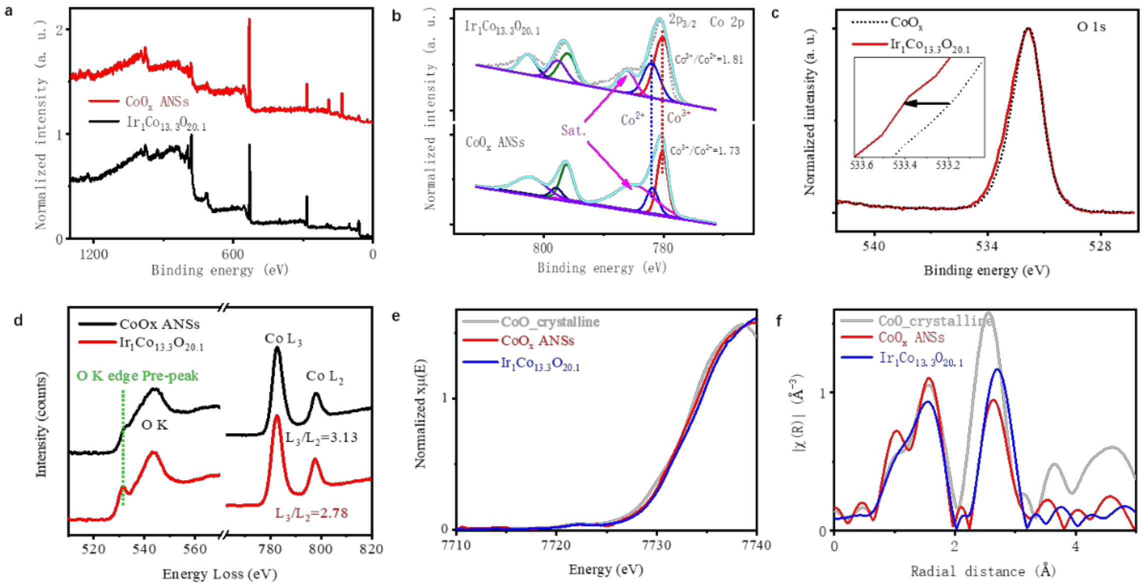

Figure 6.3 Surface chemistry and structures of $Ir_1Co_{13.3}O_{20.1}$ and CoO_x ANSs. XPS results of $Ir_1Co_{13.3}O_{20.1}$ and CoO_x ANSs (a to d). Survey spectrum (a), Co 2p spectrum (b), O 1s spectrum (c), and EELS spectrum of O K- and Co L-edge (d). Co K-edge (e) XANES and (f) EXAFS of $Ir_1Co_{13.3}O_{20.1}$ and CoO_x ANSs.

6.6. Reaction process

The catalytic activity of Ir-based catalysts usually being affected by the surrounded environment change and their valence variation during OER.[6-9,32,33] In our experiments, the OER performance improvement can be attributed to the change in the OH^- free energy, the O^{2-} to OH^- adsorption Gibbs energy difference, and the different electron affinity between Ir and Co.[34] The much higher electron affinity of Ir can attract the highly concentrated electrons moving toward Ir sites, which leads to the preferential adsorption of OH^- and intermediates during OER, thus promoting the formation of high valence Ir cations during OER.[35] Herein, the amount of Ir doping also influences the OER activity by changing the number of active sites. Figure 6.5 shows that $Ir_1Co_{13.3}O_{20.1}$ have the highest OER activity compared to other samples. Therefore, optimized stoichiometry of $IrCoO_x$ ANSs could effectively promote active Ir-O-Co cation formation, leading to a much better OER performance. It is reported that surface-absorbed O can promote OER and be released by heat-treatment.[36] In our experiment, the annealed $Ir_1Co_{13.3}O_{20.1}$ with surface-absorbed O released has much lower OER activity than $Ir_1Co_{13.3}O_{20.1}$ (Figure 6.14).

The catalysts with high activity usually possess structural instability, leading to deactivation of the catalysts.[12,37,38] The current density of $Ir_1Co_{13.3}O_{20.1}$ is stable after 10 h, while that of IrO_2 decreases by 72 % (Figure 6.15a). The decreased OER activity of IrO_2 originates from the fast degradation of active Ir in alkaline solution by forming water soluble IrO_3[2-3,11]. The $Ir_1Co_{13.3}O_{20.1}$ is also show high stability under large current (Figure 6.15b). *Ex-situ* STEM is used to check the structure of $Ir_1Co_{13.3}O_{20.1}$ after OER (Figure 6.16). The remaining isolated Ir single atoms on CoO_x ANSs demonstrate the high structural stability in OER for 10 h. The highly structural stability of Ir single atoms may be responsible for the stable OER activity. However, the matrix (CoO_x) may dissolute during OER which can lead to the Ir dissolution. Therefore, we examined the Ir ions residual in electrolyte after OER (Table 6.3). The stability number of $Ir_1Co_{13.3}O_{20.1}$ is 1.15×10^4, which is near to the value of reported amorphous IrO_x.[8] The $Ir_1Co_{13.3}O_{20.1}$ shows higher OER activity in 2 M KOH than one in 1 M KOH, and shows 3-fold increase at 60°C in 1 M KOH (Figure 6.17). To understand how catalysts restructure in reactions, *in-situ* XAS was used.[18,39-41] Relevant electrochemical results are shown in Figure 6.26. In Figure 6.4a, at the open-circle voltage (OCV), the energy at which the white line of the Ir L-edge XANES lies is in between those of Ir and IrO_2, suggesting the co-existence of high valence Ir^{4+} cations and Ir^0 atoms in the pristine sample.[26] When higher voltage is applied, the white line intensity increases and the peak shifts to higher energy (Figure 6.4a and S6.16), indicating the increase of the Ir oxidation state. Since Ir^{4+} is believed to be active for OER, [42] the increase of the Ir^{4+} ratio promotes the OER reaction. When the applied potential returned to OCV, Ir was slightly reduced back but didn't overlap with the one at OCV.[43] This can be resulted by the further oxidation of Ir^0 atoms to $Ir^{3/4+}$ ions at high potential during OER.

Furthermore, the EXAFS fitting of $Ir_1Co_{13.3}O_{20.1}$ pristine material (Figure 6.4c) shows that Ir is bonded with 6 oxygen (Table 6.5). The Ir-Co scattering pathway in pristine is around 3.56 Å, much longer than the same Ir-Co scattering paths (2.92 Å) during the reaction (Table 6.6). This suggests a strong Ir and Co interaction after applying voltage, which subsequently causes more oxidized Co cations in reactions. All those results are consistent with XPS results. Note that Ir-Ir scattering cannot be added in our model to produce meaningful fitting results for both pristine and reacted materials in our EXAFS analysis, which further verifies that most Ir is likely singly distributed on the CoO_x ANS surface, consistent with the conclusions drawn from the STEM results shown in Figure 6.1.

The restructuring of Ir cations is responsible for the high OER activity (Figure 6.9). As shown in Figure 6.4b, the Ir local coordination environment varies a lot during the reaction. The Ir-O peak becomes shaper and bonding length becomes shorter during OER due to the increased Ir oxidization state, which is also a result of stronger Ir bonding with O to form IrO_x (x near to 6) in reaction. The EXAFS analysis of Ir-O shows that the average coordination numbers (CNs) and bond-length of Ir-O decrease during OER (Figure 6.4f, Figure 6.21 and Table 6.7). These result from the restructuring of $Ir_1Co_{13.3}O_{20.1}$ in reaction conditions. Once the potential is applied, the substrate-catalyst interaction becomes stronger, thus trapping and stabilizing the surface Ir atoms into CoO_x ANSs and forming a new peak around 2.5 Å which is corresponding to shorter Ir-Co scattering path or Ir-O-Co bonding (Figure 6.4b&e). This is similar to our previous work on single atom Ru anchored on cobalt-iron layerd double hydroxides, which has a shorter and stable Ru-O-M (M=Co or Fe) bond in OER compared to that in as-synthesized catalyst.[44] In our case, the Ir cations in their first shell are not fully coordinated in OER. These under-coordinated Ir cations can adsorb OH^- efficiently. When the potential reaches 1.26 V, the surface-absorbed O and Ir-O start to be oxidized, leading to the decrease of Ir-O CNs. The Ir will capture the H_2O or OH^- from electrolyte to become fully coordinate after the voltage is back to OCV (Figure 6.4c&d; table 6.5). These results show that the OER start at an onset potential of <30 mV. In contrast, the average CN of Ir-O-Co bond (the second shell) is substantially increased, suggesting that O between Ir and Co are mostly oxidized during OER. These Ir-O-Co remains visible after OER stop (Figure 4b), as Ir/Co can get O from alkaline solution. In this case, the active Ir-O-Co can be strongly anchored on CoO_x ANSs during OER, and thus ensuring high stability in alkaline solution. In short, such high OER activity of $Ir_1Co_{13.3}O_{20.1}$ is associated with those pre-adsorpted O and the O in Ir-O-Co. In addition, the replenished O species bonding with Ir continually get preferentially oxidized in OER reaction.

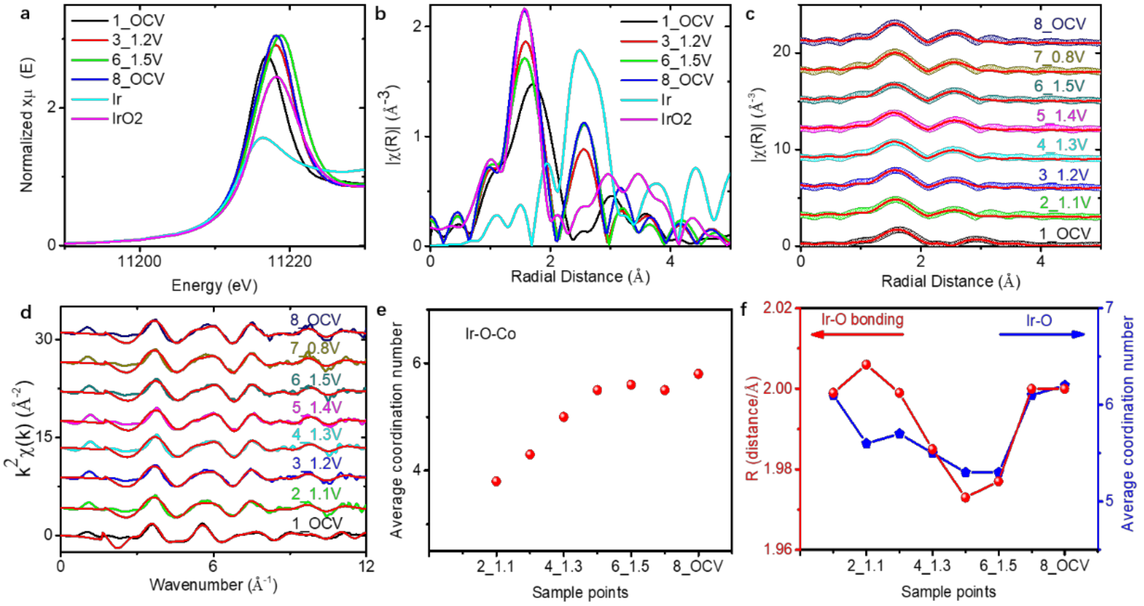

Figure 6.4 XAS results of $Ir_1Co_{13.3}O_{20.1}$. *In-situ* Ir L-edge (a) XANES and (b) EXAFS under various reaction potential; Fourier Transfer EXAFS fitting of in-situ Ir during the reaction (c) R-space and (d) k-space.

6.7. Conclusions

In summary, we demonstrated that the Ir/Co synergistic effect can be effectively manipulated by controlling the O state in SACs. The $Ir_1Co_{13.3}O_{20.1}$ANSs start the OER at low onset potential of <30mV. This material shows superior OER activity which is 160-fold of commercial IrO_2. The Ir single atoms on CoO_x ANSs enable the ultrahigh utilization of Ir, leading to the lowest cost for industrial applications. The in-situ XANES results disclose that the O in the *in-situ* formed Ir-O-Co get preferentially oxidized with smaller overpotential, magnifying OER activity. We believe that our findings could be a giant leap towards designing highly active catalysts for various applications, such as metal-air batteries and hydrogen production from water electrolysis.

6.8. Acknowledgements

This work is supported by the National Natural Science Foundation of China (21802065&U1830204) and Guangdong Innovative and Entrepreneurial Research Team Program

(2016ZT06N500), Shenzhen Peacock Plan (KQTD2016022620054656), Shenzhen Clean Energy Research Institute (No. CERI-KY-2019-003). Z. F. thanks the startup funding from Oregon State University. The XAS measurements were done at beamline 9-BM of the Advanced Photon Source, which is a U.S. Department of Energy (DOE) Office of Science User Facility operated for the DOE Office of Science by Argonne National Laboratory under Contract No. DE-AC02-06CH11357.

6.9. Experimental

6.9.1. Chemicals

All the chemicals are directly used in experiments without further purification. $Co(NO)_3 \cdot 6H_2O$ (>98 %), $Ni(NO)_3 \cdot 6H_2O$ (>98 %), cetyltrimethylammonium bromide (CTAB, >95 %), $H_2IrCl_6 \cdot 6H_2O$ (> 40 %, metal basis), sodium borohydride (SB, >99 %), isopropanol (>95 %), acetone (>95 %), and NaOH (>99.999 %) were purchased from Aldrich. Nafion solution was purchased from sigma (5 wt. % aqueous solution). Commercial IrO_2 is purchased from Macklin Biochemical (99.9 % metal basis, Ir>84.5 %). Nickel Foam was purchased from Shenzhen Green and Creative Environmental Science and Technology Co. Ltd.

6.9.2. Synthesis of $IrCoO_x$-(Sample X) ANSs

This experiment is carried out at room temperature in air. 4 mmol $Co(NO)_3 \cdot 6H_2O$ is added into 100 mL water (contains 50 mmol CTAB) with magnetic stirring to form solution A. After 20 min, 6 mmol SB is added into solution A quickly. After reacting for 30 min, amount of $H_2IrCl_6 \cdot 6H_2O$ aqueous solution (X=0.5 ml, 1 ml, 2 ml, 3 ml, and 4 ml) (40 mg/mL) is added. The system is held for another 1 h with magnetic stirring. Then 1 mmol SB is added into system and held for 20 min. The precipitation is washed by water and acetone for 5 times. Those black powders are dried in vacuum oven at 80 °C for whole night. The yield of $IrCoO_x$-(Sample 4) is ca. 648 mg. The mass loading of Ir in $IrCoO_x$-(Sample 4) is ca. 20 wt. %.

6.9.3. Synthesis of Ir nanoparticles/CoO_x

4 mL $H_2IrCl_6 \cdot 6H_2O$ aqueous solution and 4 mmol $Co(NO)_3 \cdot 6H_2O$ are added into 100 mL water (contains 50 mmol CTAB) with magnetic stirring to form transparent solution. Then, 6 mmol SB is added into solution quickly. After reacting for 30 min, the precipitation is washed, dried, and collected as $IrCoO_x$-(Sample X) ANSs.

6.9.4. Annealing of $Ir_1Co_{13.3}O_{20.1}$

20 mg prepared powders of $Ir_1Co_{13.3}O_{20.1}$ (4 ml $H_2IrCl_6 \cdot 6H_2O$ aqueous solution is used during synthesizing process) are heated to 450 °C with a heat rating of 5 °C/min and held for 2 h in air. After cooling down to room-temperature, the black powders are collected for following electrochemical characterization.

6.9.5. Synthesis of $IrNiO_x$ ANSs

$IrNiO_x$ ANSs are prepared similar to $Ir_1Co_{13.3}O_{20.1}$ ANSs, using $Ni(NO)_3 \cdot 6H_2O$ instead of $Co(NO)_3 \cdot 6H_2O$.

6.9.6. Synthesis of CoO_x ANSs

The CoO_x ANSs are prepared in a way similar to $IrCoO_x$-(sample X) ANSs synthesis without Ir using. The yield of CoO_x ANSs is 540 mg (the feeding amount is 4 mmol).

6.9.7. Structure characterization

The morphology and microstructure characterizations of the as-prepared samples were investigated by scanning electron microscopy (SEM) (FEI, Helios Nanolab 600i, 2kV), Transmission electron microscopy (TEM) and selected area electron diffraction (SAED) (FEI, ETEM, G2, 200kV), scanning transmission electron microscopy with an energy dispersive X-ray spectroscopy attachment (STEM-EDS, FEI Titan Themis, 300 kV). X-ray diffraction (XRD) (Bruker ECO D8 power X-ray diffractometer with Cu Kα radiation) were utilized to determine the crystal structure of the samples. The 20 mg powders ($IrCoO_x$-(Sample X) ANSs) is dissolved into 10 mL nitric acid (1 M), and then the mixed solution is sonicated for 3 min. This solution is heated to 180 °C for 4 h, and then the pink solution is collected for ICP-OES testing.

6.9.8. Electrochemical characterization

All experiments are carried out using CHI760e in a three-electrode system in a PTFE bottle. Rotate glassy disk carbon electrode (GCE) (3 mm) is the support of active materials to be used as working electrode. Ag/AgCl (saturated with 4 M KCl) and graphite rod are used as counter electrode and reference electrode, respectively. Electrolyte is 1 M KOH saturated with O_2 (99.999) %. Working electrode for Co-based NSs is prepared by drop 20 uL dispersion (catalyst ink (4 mg/mL) with water containing 10 uL 5 wt. % Nafion solution) on a GCE (polished by Al_2O_3). Cycling voltammetry (CV), linear sweep voltammetry (LSV) and chronoamperometry are measured at 298 K, air and 10 mV/s (scan rate) on CHI 760e. After 10 h, the catalyst is washed by water and ethanol before characterized by STEM. The large current density test is carried out on a Nickel Foam (1 cm×0.5 cm). The catalyst loading on Nickel Foam is ca. 2.2 mg/cm^2. The prepared working electrode is soaked in 1 M KOH solution for 2 h to form a Na^+ Nafion before electrochemistry being conducted. 100 mL KOH solution is used for OER test.

6.9.9. In-situ and operando XAS measurement

In-situ XANES and EXAFS experiments were performed at the Advanced Photon Source (APS) beamline 9-BM-B&C of Argonne National Laboratory (ANL). The working electrodes were prepared by depositing 2mg catalyst on a 100 μm thick and 2.5 x 1.5 cm^2 carbon cloth to form a 0.5 x 1 cm^2 active area (catalysts loading is ca. 2.2 mg/cm^2). The working electrodes, counter electrodes (Pt) and reference electrodes (Ag/AgCl) were mounted onto a custom-designed *in-situ* XAS fluorescence cell.[39,40,45] Electrochemical measurements were done by a Gamry 600 electrochemical workstation under oxygen gas flow. A Vortex ME4 detector was used to collect the Ir L-edge fluorescence signal while a Si(111) monochromator scanned the incident X-ray photon energy through the Ir L absorption edge. The Si (333) harmonic was rejected by a Rh coated focusing mirror with an incident angle of 2.8 mrad. Each selected potential (iR compensated) was held until sufficient data statistics of XAS were achieved. The X-ray beam was calibrated using a Ir metal pellet. Data reduction, data analysis, and EXAFS fitting were performed with the Athena, Artemis, and IFEFFIT software packages. Standard procedures were used to extract the EXAFS data from the measured absorption spectra. The pre-edge absorption was fit with a line which was then subtracted from the full spectrum. The data was then normalized by dividing by a constant factor such that the post edge absorption has a value roughly equal to one. The post-edge background was determined using a cubic-spline-fit procedure and then subtracted to obtain the EXAFS.[45,46] For model-based EXAFS analysis, all the scattering paths were generated by the FEFF calculation function in Artemis based on the crystal structure of IrCoO (Figure 6.22). Phase shifts and back-scattering amplitudes were generated by the FEFF calculations based on crystal structures of IrO_2, and were then calibrated through performing the FEFFIT of the EXAFS data of the IrO_2 reference sample, mainly to obtain the amplitude reduction factor (S_0^2) values. With S_0^2 known, the EXAFS data of the catalyst materials were fitted with such generated phase shifts and amplitudes. We also check with EXAFS spectra of back-to-OCV sample to have the full six coordinated Ir-O bonding. All those EXAFS fitting are done with K-range from 3 to 12Å^{-1}. For Co model-based EXAFS analysis, the same procedure was applied by using CoO as reference instead of IrO_2.

6.10. Supplementary Information

Table 6.1 Ir/Co ratio of IrCoOx-(Sample X) NSs defined by ICP-OES.

Sample	**Co (wt. %)**	**Ir (wt. %)**	**Molar ratio (Ir/Co)**
$IrCoO_x$-(Sample 0.5) **$Ir_{0.067}Co_{13.3}O_{20.1}$ ANSs**	98.4	1.6	5:1000
$IrCoO_x$-(Sample 1) **$Ir_{0.160}Co_{13.3}O_{20.1}$ ANSs**	96.2	3.8	12:1000
$IrCoO_x$-(Sample 2) **$Ir_{0.279}Co_{13.3}O_{20.1}$ ANSs**	93.5	6.5	21:1000
$IrCoO_x$-(Sample 3) **$Ir_{0.545}Co_{13.3}O_{20.1}$ ANSs**	88.3	11.7	41:1000
$IrCoO_x$-(Sample 4) **$Ir_{1}Co_{13.3}O_{20.1}$ ANSs**	81.2	18.8	71:1000

The Co/O ratio is calculated from EDS results.

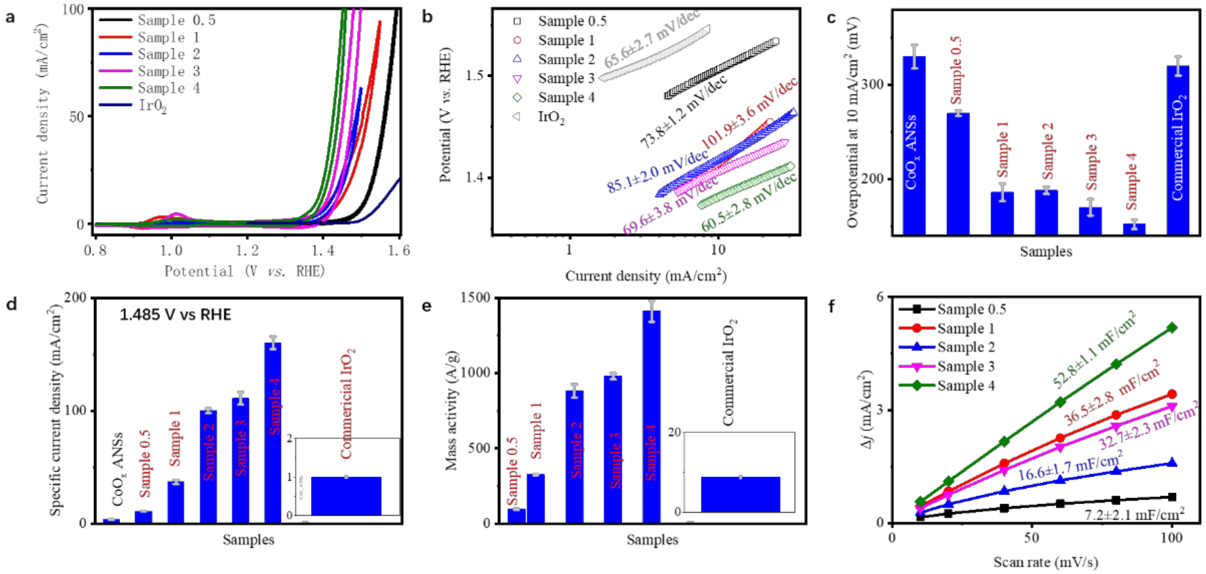

Figure 6.5 Electrochemical characterization of IrCoOx-(Sample X) ANSs with different amount of Ir doping. CV curves (a), Tafel plots (b), specific overpotential (c), specific current density (d), mass activity at 1.485 V vs. RHE (e), and C_{dl} value (f) of IrCoOx-(Sample X) ANSs.

The small amount of Ir doping in Sample 0.5 leads to the C_{dl} value decrease from 25.3 mF/cm^2 to 5.9 mF/cm^2, suggesting that the reactive sites transport from sole Co cations to Ir/Co couplings. However, the Sample 0.5 possess much higher OER activity than CoO_x ANSs (Figure 6.5c to 6.5e), demonstrating the ultrahigh intrinsic activity of Ir/Co couplings.

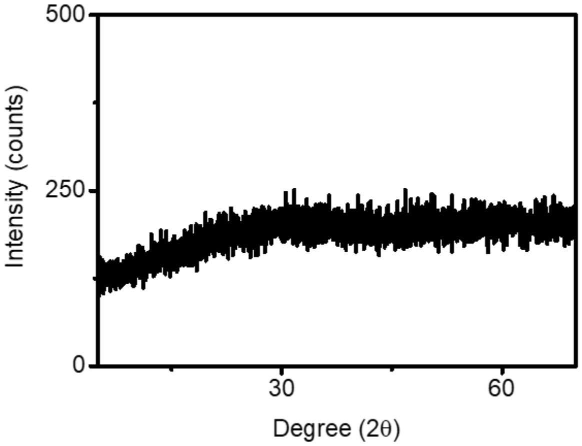

Figure 6.6 XRD pattern of $Ir_1Co_{13.3}O_{20.1}$.

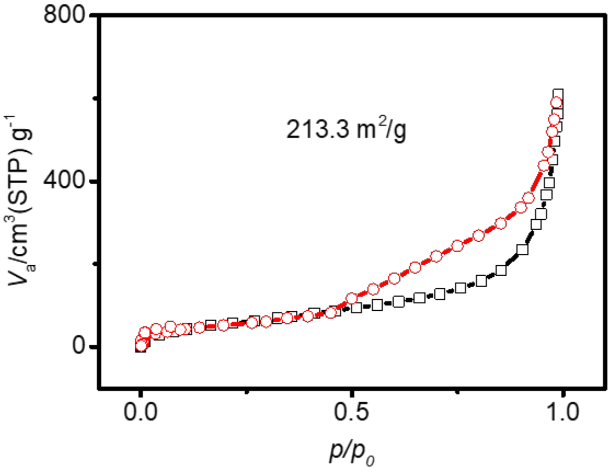

Figure 6.7 N_2 adsorption desorption isotherms of $Ir_1Co_{13.3}O_{20.1}$.

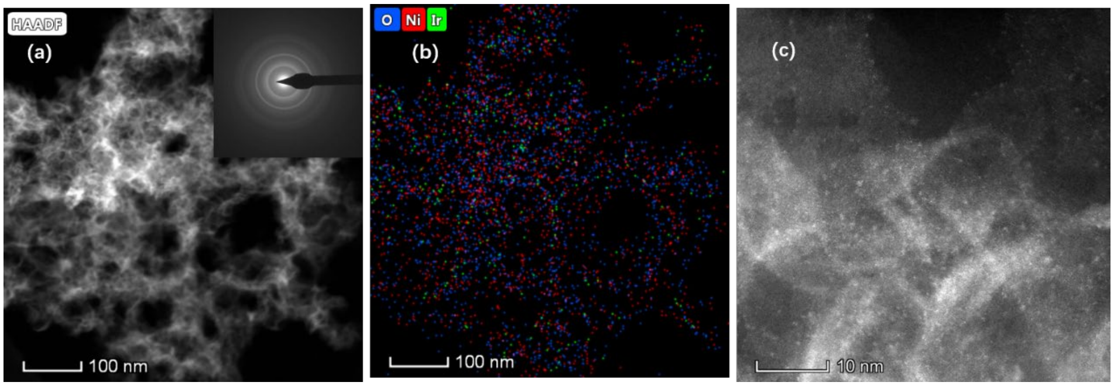

Figure 6.8 Structural characterizations of $IrNiO_x$ ANSs. Low magnification STEM (a), EDS (b), and high magnifications (c). The diffraction circles in SAED pattern (inset in Figure 6.8a) demonstrate the amorphous feature of the as-prepared IrNiOx ANSs. The brighten spots correspond to the Ir atoms (c).

Table 6.2 Collection of reported Co-based electrocatalysts on glassy carbon electrode for OER in 1 M KOH

Sample	**Tafel slope (mV/dec)**	**Overpotential at 10 mA/cm^2 (mV)**	**Mass activity (A/g)**	**Ref.**
CoOOH	38	300	66.6 @ 1.53 V	148
$CoSe_2$	50	430	--	149
Au@Co_3O_4	60	370	--	150

NiO/CoN	35	300	853 @ 1.596 V	151
NG-CoSe$_2$	40	366	63.5 @ 1.596 V	152
CoFe LDH	34	264	--	153
CoNi-P	52	270	--	154
rGO@CoFe-Pi	36	300	160 @ 1.59 V	155
CoNi-P	84	292	253 @ 1.59 V	156
Ir@Co	90	273	--	157
Co/Mo$_2$C@CNTs	90	356	--	158
Ir$_1$Co$_{13.3}$O$_{20.1}$	60	152±5.2	1412@1.485 V	This work

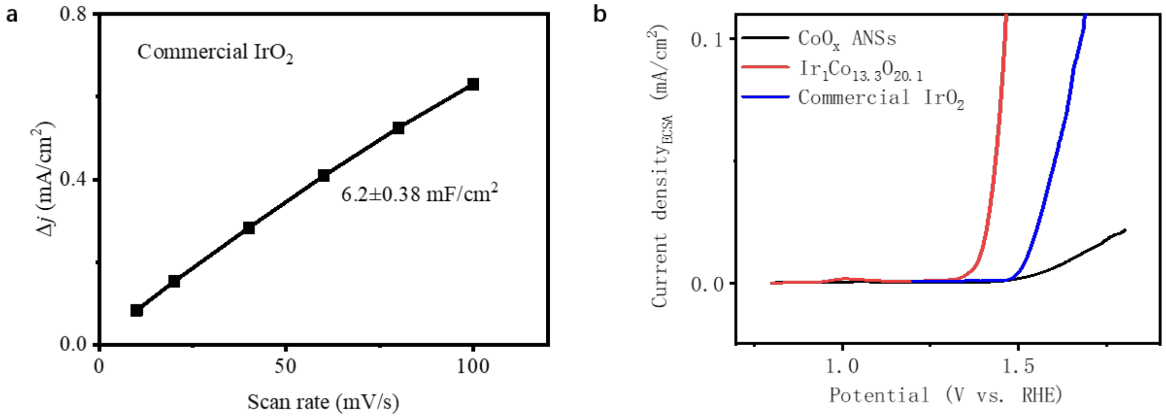

Figure 6.9 The ECSA-normalized current density of Ir$_1$Co$_{13.3}$O$_{20.1}$. C$_{dl}$ of Commercial IrO$_2$ (a) and normalized CV curves of various samples (b). The CoO$_x$ ANSs possess the lowest reaction rates on per active sites.

The ECSA is calculated from C_{dl},

$$ECSA = R_f S$$

$$R_f = \frac{C_{dl}}{20\ uF/cm^2}$$

$$Current\ density = \frac{measured\ current}{ECSA}$$

The ECSA of $Ir_1Co_{13.3}O_{20.1}$ ANSs is ca. 181.79 cm^2. This value is smaller than the surface area (tested by BET method), indicating that the ECSA is not a reliable way to estimate the exposure sites of Co-O compounds.

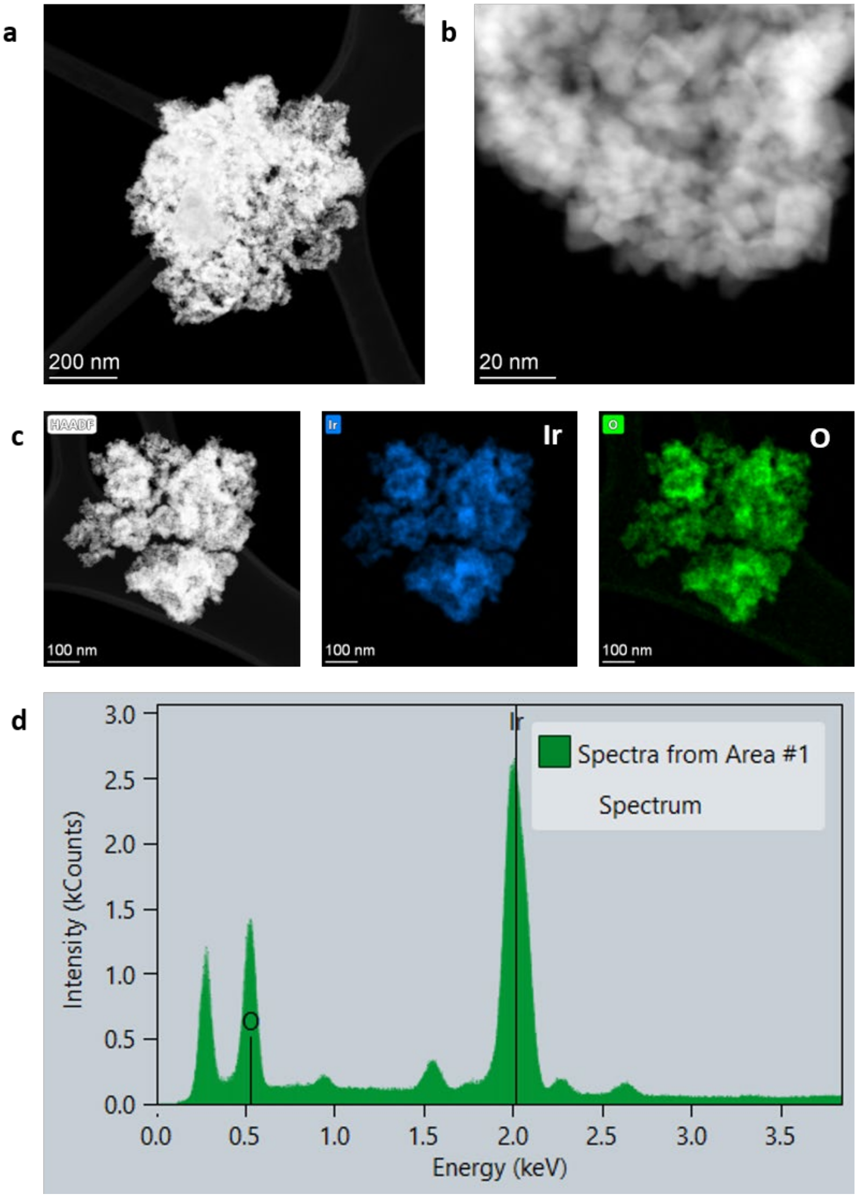

Figure 6.10 TEM results of commercial IrO_2. Low magnification (a), high magnification (b) image, EDS mapping (c), and element profile of Ir and O (d). The Ir:O atomic ratio is ca. 30:70.

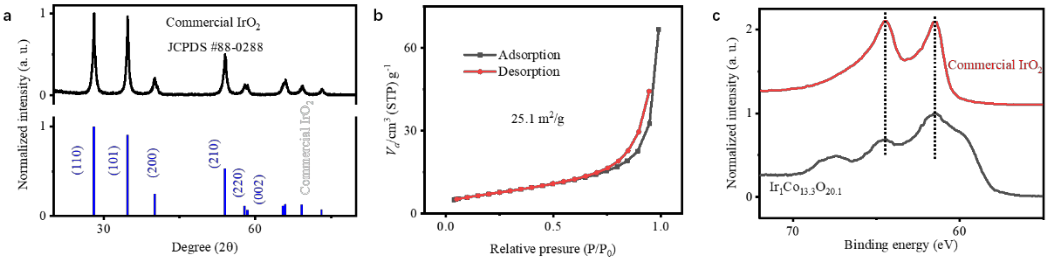

Figure 6.11 Structural and surface characterization of commercial IrO_2. XRD pattern (a), N_2 adsorption desorption isotherms (b), and Ir 4f spectra of commercial IrO_2. The Ir in $Ir_1Co_{13.3}O_{20.1}$ show various valance, including Ir^0, Ir^{3+}, and Ir^{4+}.

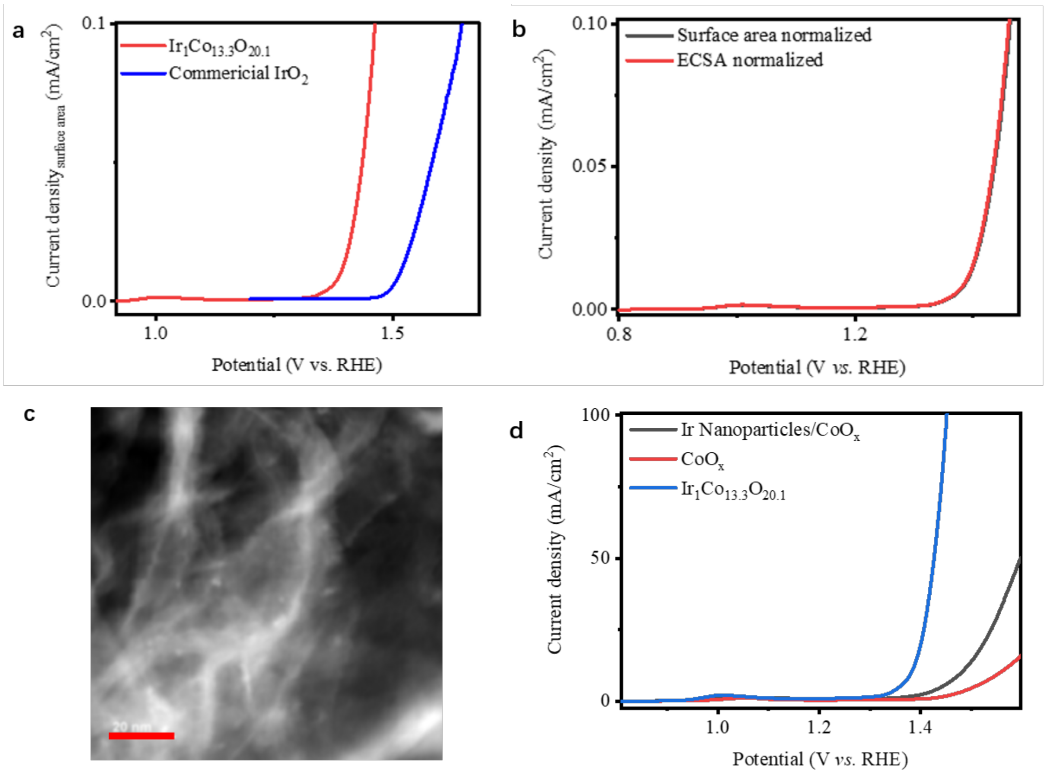

Figure 6.12 Comparison of normalized current density. Surface area normalized current density of $Ir_1Co_{13.3}O_{20.1}$ and commercial IrO_2 (a). Comparison of $Ir_1Co_{13.3}O_{20.1}$ current density with different normalized method (b). The exposed Ir sites in $Ir_1Co_{13.3}O_{20.1}$ work effectively during OER. STEM image (c) and polarization curve (d) of Ir nanoparticles/CoO_x. Scaler bar is 20 nm.

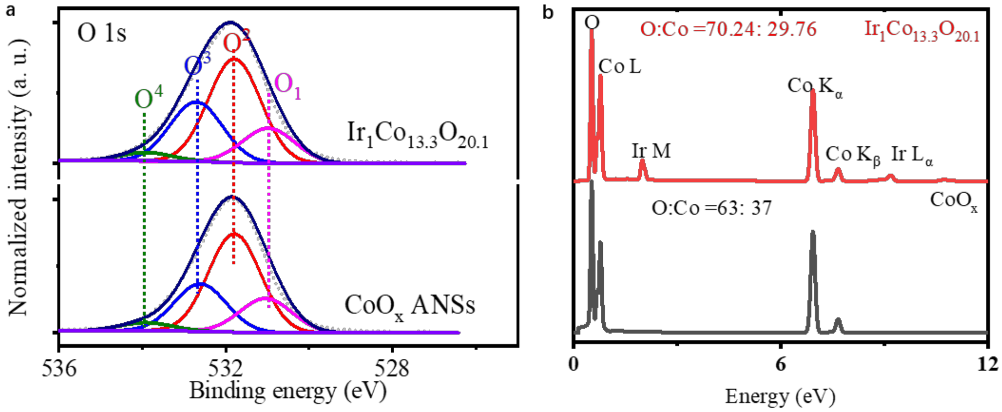

Figure 6.13 XPS and EDS results of O. O 1s spectrum in XPS (a). EDS profile (b).

The ratio of O^2/O increases from 50.16% in CoO$_x$ ANSs to 52.21% in Ir$_1$Co$_{13.3}$O$_{20.1}$ ANSs, indicating that the Ir loading can promote the O adsorption. This modulation of O can increase the adsorption efficiency and average valence of catalysts.

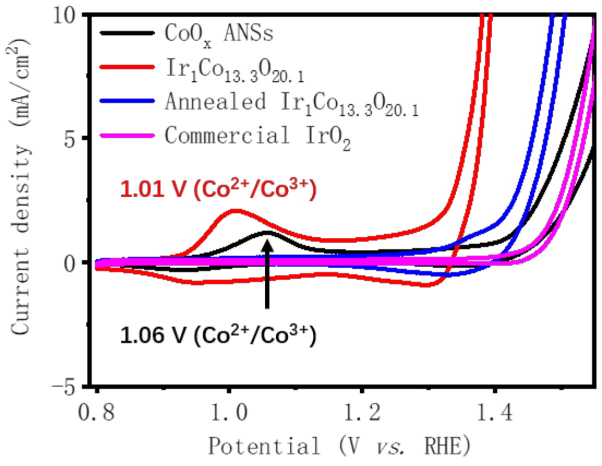

Figure 6.14 CV curves of CoO$_x$-based ANSs.

The oxidation area is far larger than the reduction area, indicating that the oxidation of most metal cations in OER can be reduced to its initial state. After Ir doping, the peak belonged to Co^{2+}/Co^{3+} moves from 1.06 V to 1.01 V; meanwhile the oxidation area is increased compared to CoO_x ANSs. This result can be resulted by that the Ir in Ir-O-Co in pristine $Ir_1Co_{13.3}O_{20.1}$ can promote the oxidation of Co, which is also supported by the XAS results in Figure 4e&f. The increased oxidation area can be contributed by the Ir oxidation area and promoted Co oxidation state. The pure IrO_2 has a very low integral oxidation area, and thus the substantially increased oxidation area can be resulted by the synergistic effect of Ir and Co.

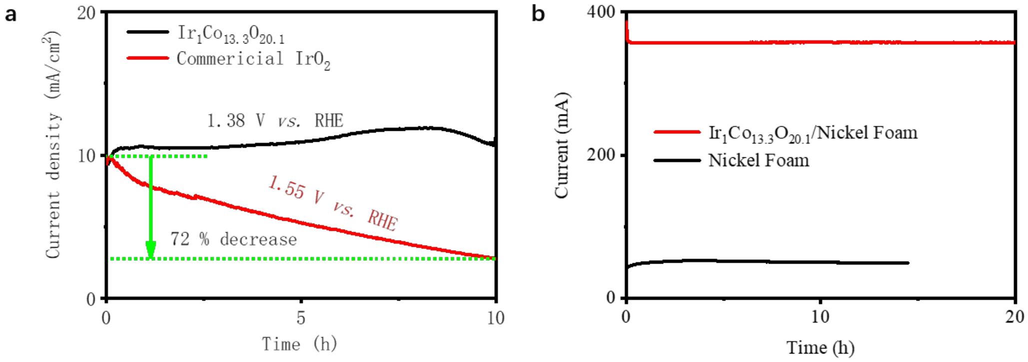

Figure 6.15 Accelerating degradation of $Ir_1Co_{13.3}O_{20.1}$. Catalysts on glassy carbon electrode (a). Catalysts on Nickel Foam (b). The active area of Nickel Foam is ca. 0.5 cm^2.

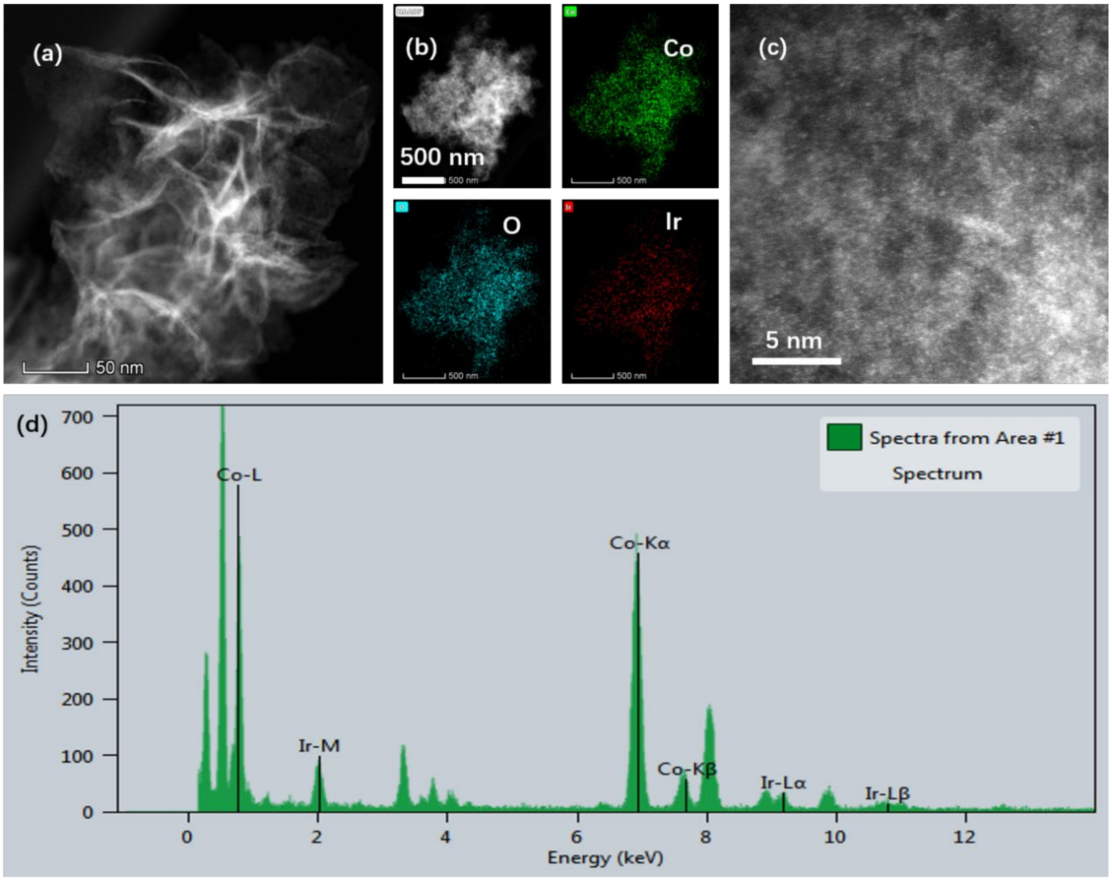

Figure 6.16 Structural characterization of $Ir_1Co_{13.3}O_{20.1}$ after use in OER for 10 h at 1.38 V *vs.* RHE.

Sample 4 show the sheet-like feature after use (Figure 6.12a), demonstrating the high structural stability of $Ir_1Co_{13.3}O_{20.1}$, suggesting the potential of using Co oxides as practical support for catalysts for OER. Further large area EDS mapping (Figure 6.12b) and high-resolution STEM image (Figure 6.12c) demonstrates the high structural stability of Ir single atoms on Co oxides, with abundant oxygen vacancies surrounded. According to Figure 6.12d, the Ir/Co atomic ratio in $Ir_1Co_{13.3}O_{20.1}$ is 6.8 % after use in OER (Figure 6.12d), near to the initial value (7.1 %) (Table 1).

Table 6.3 Ir/Co disolution in electrolyte after OER.

	Element	**Concentration (mg/L)**
Electrolyte after 10 h at 1.38 V vs. RHE	Ir	0.0011
	Co	0.0042

Stability-number of $Ir_1Co_{13.3}O_{20.1}$ is calculated according to literature (Ref. 8 in main text),

$$Stability \cdot Number = \frac{n_{oxygen \cdot molecules}}{n_{Ir \cdot disollution}}$$

The $n_{oxygen.molecules}$ is calculated from the volume of produced oxygen from water electrolysis. The $n_{Ir.disolutition}$ is the amount of Ir ions that can be observed in electrolyte after OER, as shown in Table 3. The dissolution rate of Ir during OER is 1.1 ug/h.

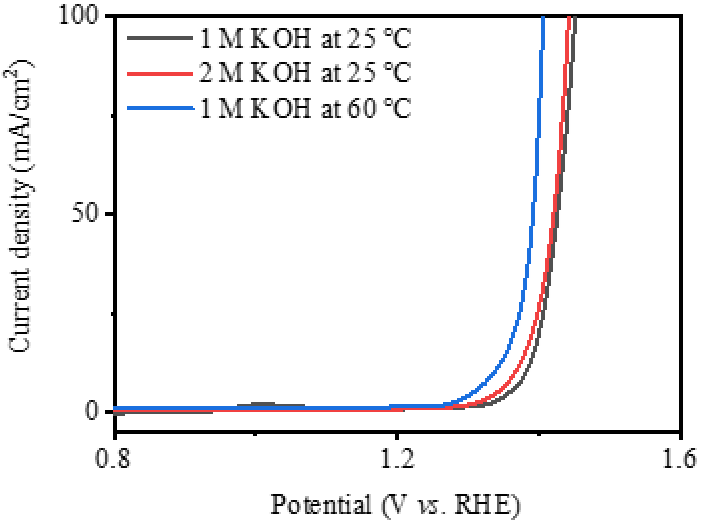

Figure 6.17 The OER test of $Ir_1Co_{13.3}O_{20.1}$ under various condition.

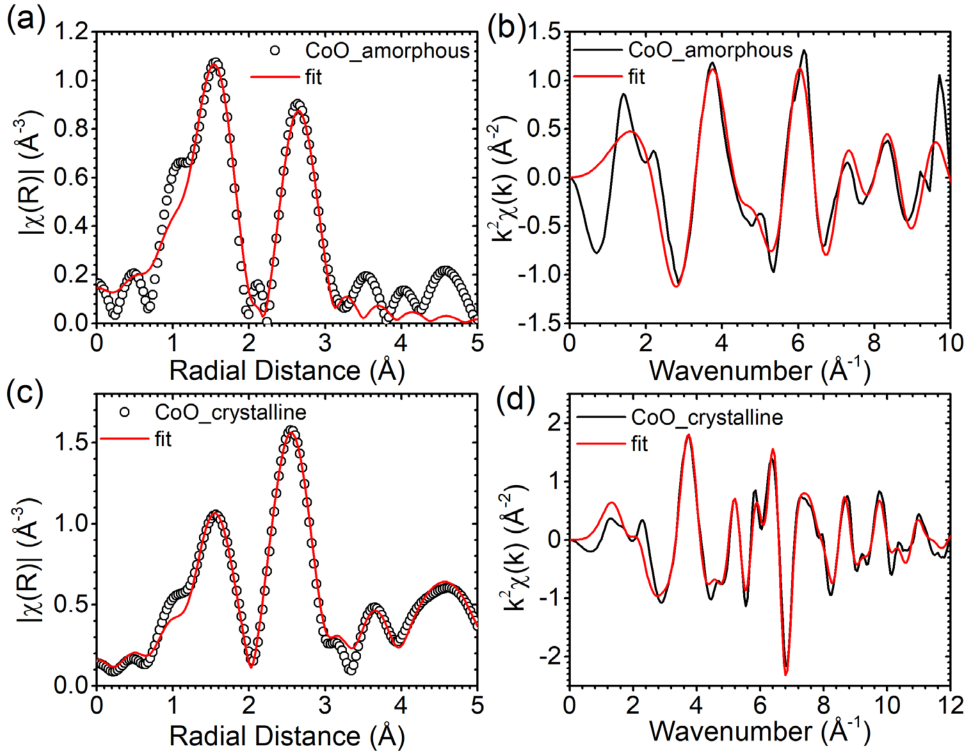

Figure 6.18 Model based EXAFS fitting of amorphous CoO_x (a) R-space (b) K-space, and crystalline CoO (c) R-space (d) k-space.

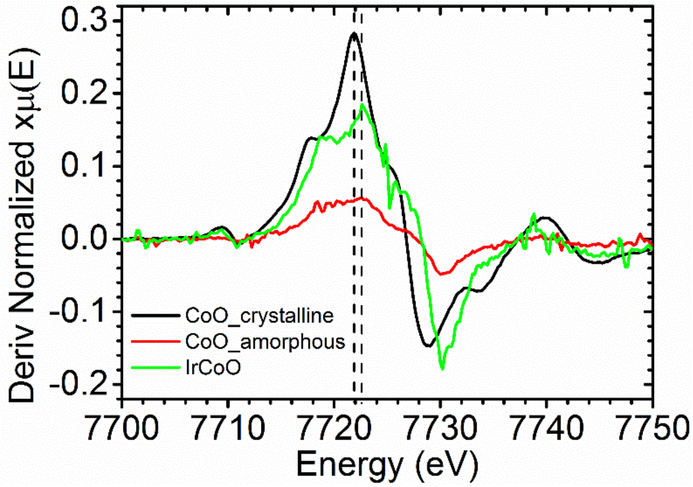

Figure 6.19 XAS results of Ir1Co13.3O20.1 and CoOx ANSs. Ex-situ Co K-edge first derivative XANES

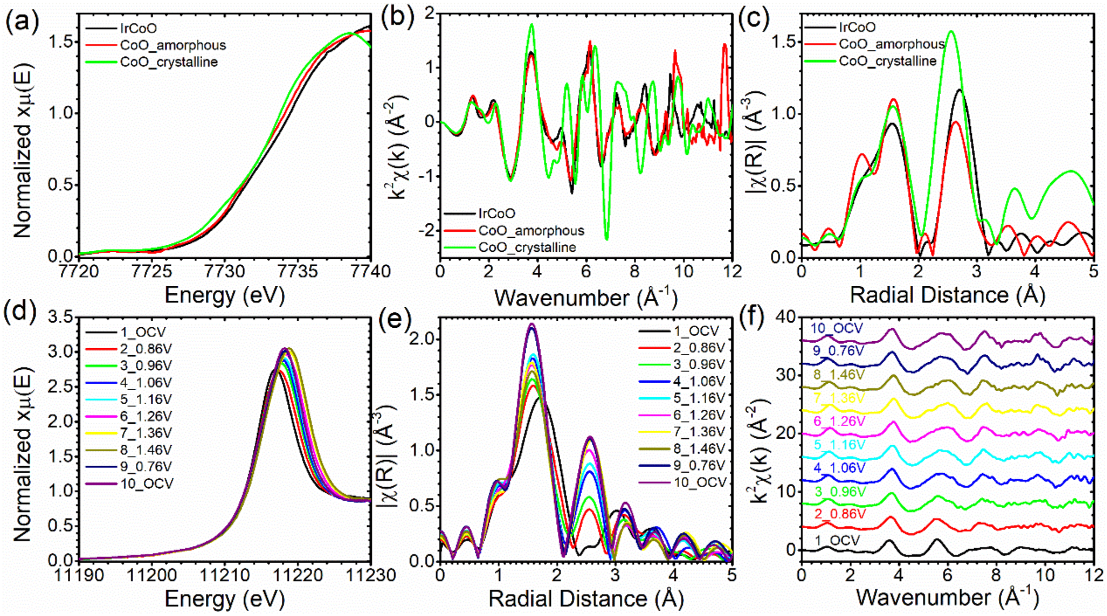

Figure 6.20 XAS results of $Ir_1Co_{13.3}O_{20.1}$ and CoOx ANSs. ex-situ Co K-edge (a) XANES, Fourier Transfer EXAFS (b) k-space and (c) R-space; in-situ Ir L-edge (d) XANES, Fourier Transfer EXAFS (e) R-space and (f) k-space.

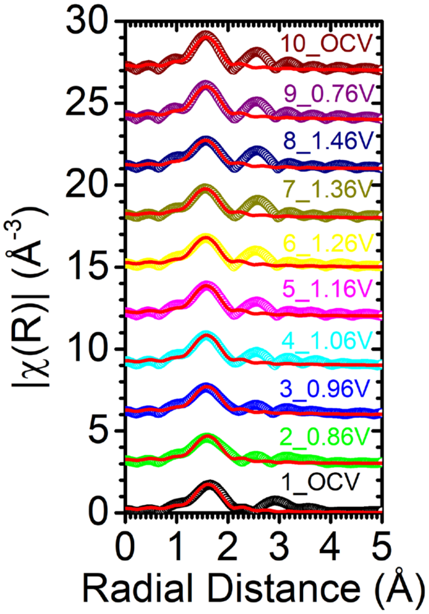

Figure 6.21 Magnitudes of EXAFS Fourier transforms and fits to the first-shell of in-situ $Ir_1Co_{13.3}O_{20.1}$ R-space.

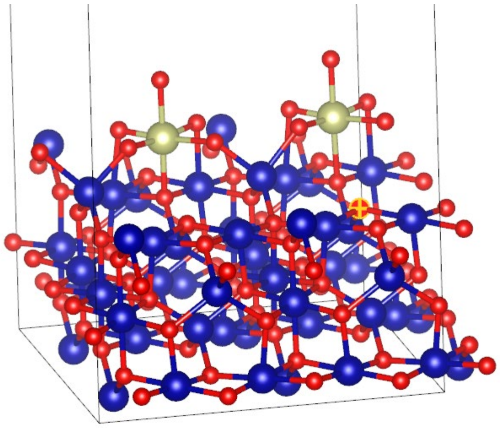

Figure 6.22 Model used for XANES analysis. Ir-Co_3O_4.

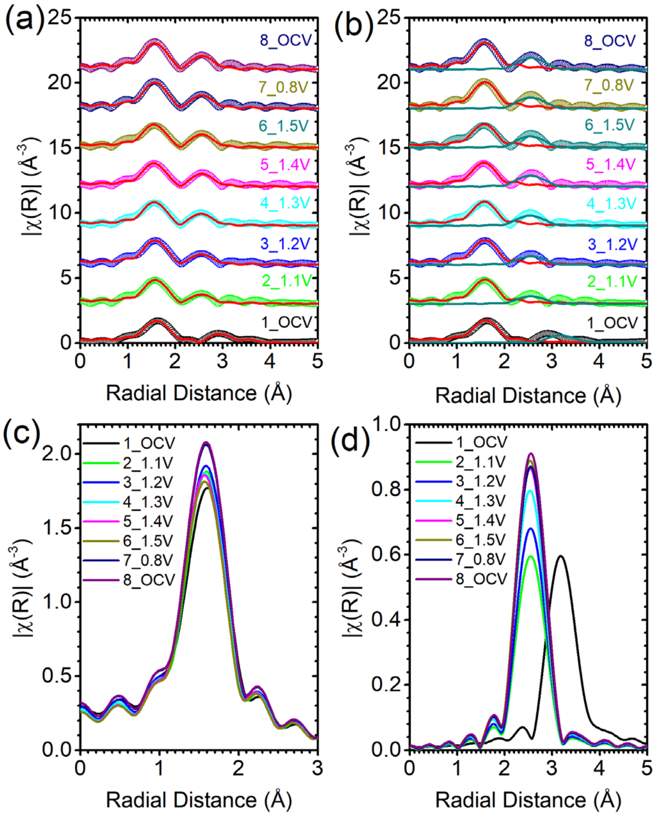

Figure 6.23 (a) Magnitudes of EXAFS Fourier transforms and fits of in-situ $Ir_1Co_{13.3}O_{20.1}$; (b) EXAFS R-space raw data with fitting scattering path (the red solid line is Ir-O scattering path and the dark cyan solid line is Ir-Co scattering path); Magnitudes of (c) Ir-O and (d) Ir-Co scattering path of in-situ $Ir_1Co_{13.3}O_{20.1}$ R-space.

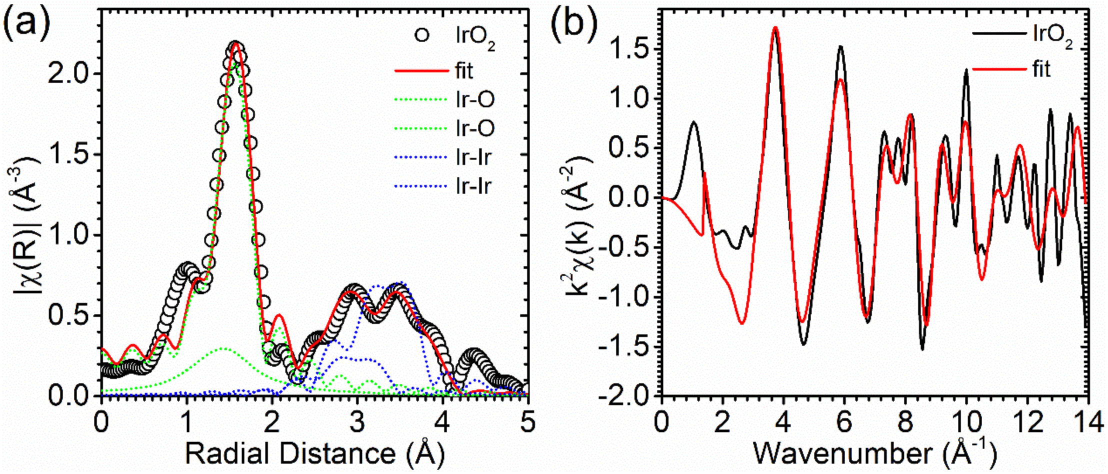

Figure 6.24 Magnitudes of EXAFS Fourier transforms and fits of IrO_2 standard (a) R-space with Ir-O and Ir-Ir scattering path (b) K-space

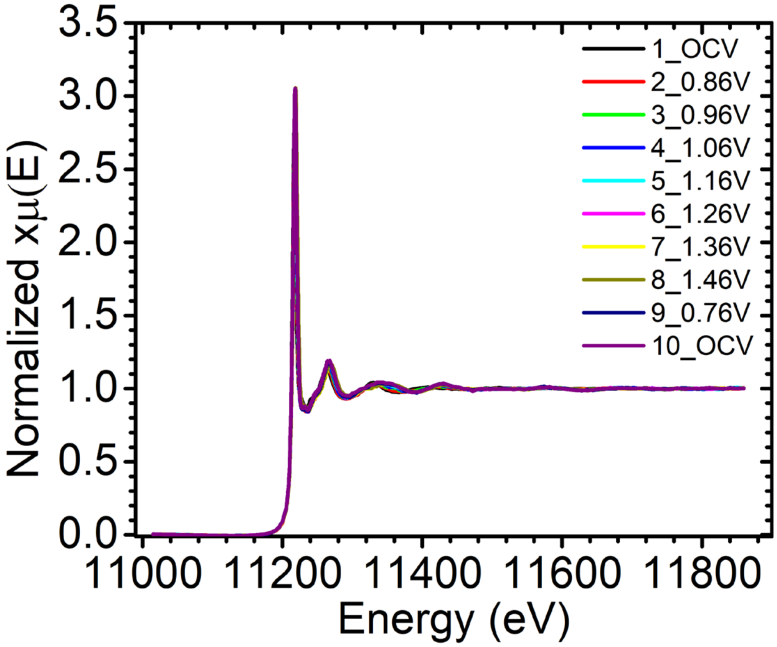

Figure 6.25 Normalized Ir L-edge XAS for $Ir_1Co_{13.3}O_{20.1}$.

Table 6.4 Fitting parameters of the EXAFS spectra of crystalline CoO (c-CoO) and CoO_x ANSs (a-CoO) (CN: coordination number; R: distance; σ^2 : mean-square disorder; E_0: energy shift, S_0^2: amplitude reduction factor). The numbers in parentheses for CN are the full errors.

	Scattering Path	CN	R (Å)	error	E_0 (eV)	error	σ^2(Å^2)	error	S_0^2	error	R-factor
c-CoO	**Co-O**	**6**	**2.092**	**0.012**	**-2.05**	**0.94**	**0.0075**	**0.0021**	**0.71**	**0.08**	**0.011**
	Co-Co	**12**	**3.006**	**0.009**			**0.0105**	**0.0013**			
a-CoO	**Co-O**	**6(1.3)**	**2.034**	**0.017**	**-4.37**	**1.89**	**0.0077**	**0.0031**	**0.71**	**0.15**	**0.015**
	Co-Co	**5.8(1.2)**	**3.069**	**0.018**			**0.0089**	**0.0024**			

Table 6.5 Fitting parameters of the EXAFS spectra of $Ir_1Co_{13.3}O_{20.1}$ pristine at OCV. The single digit numbers in parentheses are the last digit errors.

Scattering Path	CN	R (Å)	error	σ^2(Å^2)	error	E_0 (eV)	S_0^2	R-factor
Ir-O	**6.0(4)**	**2.03**	**0.01**	**0.0064**	**0.0010**	**10.1(1)**	**1.05(7)**	**0.015**
Ir-O-O	**6.0(4)**	**2.98**	**0.07**	**0.0021**	**0.0047**			
Ir-O	**1.5(4)**	**3.09**	**0.07**	**0.0021**	**0.0047**			
Ir-O-O	**3.0(4)**	**3.17**	**0.20**	**0.0007**	**0.0011**			
Ir-Co	**3.0(4)**	**3.56**	**0.09**	**0.0024**	**0.0018**			
Ir-O	**6.0(4)**	**3.70**	**0.23**	**0.0006**	**0.0011**			
Ir-O	**3.0(4)**	**3.81**	**0.46**	**0.0201**	**0.0011**			
Ir-O	**3.0(2)**	**3.99**	**0.33**	**0.0008**	**0.0011**			
Ir-O	**3.0(2)**	**4.12**	**0.11**	**0.0023**	**0.0352**			

Table 6.6 Fitting parameters of the co-refined EXAFS spectra of $Ir_1Co_{13.3}O_{20.1}$ at various reaction potential. The single digit numbers in parentheses are the last digit errors expect CNs. The numbers in parentheses for CNs are the full errors.

	Ir-O				Ir-Co					
	CN	R (Å)	σ^2(Å^2)	S_0^2	CN	R (Å)	σ^2(Å^2)	S_0^2	E_0 (eV)	R-factor
2_1.06V	5.4(0.4)	2.00(1)	0.005(1)	0.94(7)	3.8(0.9)	2.93(1)	0.009(2)	0.6(2)	11.1(5)	0.015
3_1.16V	5.4(0.4)	2.00(1)		0.95(7)	4.3(1.1)	2.93(2)		0.7(2)		
4_1.26V	5.2(0.3)	1.99(1)		0.91(6)	5.0(1.1)	2.91(1)		0.8(2)		
5_1.36V	5.1(0.3)	1.97(1)		0.89(6)	5.5(1.1)	2.92(1)		0.9(2)		
6_1.46V	5.0(0.5)	1.98(1)		0.88(9)	5.6(1.4)	2.92(1)		0.9(2)		
7_0.76V	5.8(0.4)	2.00(1)		1.02(7)	5.5(1.2)	2.93(1)		0.9(2)		
8_OCV	5.9(0.5)	2.00(1)		1.03(9)	5.8(1.5)	2.93(2)		1.0(3)		

Table 6.7 First-shell fitting parameters of the co-refined EXAFS spectra of $Ir_1Co_{13.3}O_{20.1}$ at various reaction potential. The single digit numbers in parentheses are the last digit errors.

	Ir-O					
	CN	R (Å)	σ^2(Å^2)	E_0 (eV)	S_0^2	R-factor
1_OCV	5.4(3)	2.03(1)	0.0052(7)	10(1)	0.94(6)	0.011
2_0.86	5.2(4)	2.02(1)			0.91(8)	
3_0.96	5.2(4)	2.01(1)			0.90(8)	
4_1.06	5.5(4)	2.00(1)			0.96(9)	
5_1.16	5.5(5)	2.00(1)			0.96(9)	
6_1.26	5.2 (4)	1.98(1)			0.92(6)	

7_1.36	**5.1(4)**	**1.97(1)**		**0.89(7)**	
8_1.46	**5.0(6)**	**1.97(1)**		**0.88(9)**	
9_0.76	**6.0(5)**	**2.00(1)**		**1.04(8)**	
10_OCV	**6.0(6)**	**2.00(1)**		**1.05(9)**	

Table 6.8 Fitting parameters of the EXAFS spectra of stand IrO_2. The single digit numbers in parentheses are the last digit errors. The number in parentheses for S_0^2 are the full digit errors.

Scattering Path	**CN**	**R (Å)**	**E_0 (eV)**	**σ^2(Å^2)**	**S_0^2**	**R-factor**
Ir-O	**2.0**	**1.86(7)**	**7(2)**	**0.0200(9)**	**1.05(0.11)**	**0.018**
Ir-O	**4.0**	**1.96(1)**		**0.0014(2)**		
Ir-Ir	**2.0**	**3.13(2)**		**0.0048(5)**		
Ir-Ir	**8.0**	**3.52(2)**		**0.0048(6)**		
Ir-O-Ir	**16.0**	**3.72(2)**		**0.0080(5)**		
Ir-O	**16.0**	**3.92(2)**		**0.0200(4)**		
Ir-O	**4.0**	**3.96(2)**		**0.0134(7)**		
Ir-O	**8.0**	**4.02(2)**		**0.0207(2)**		
Ir-O-O	**8.0**	**4.37(2)**		**0.0008(3)**		

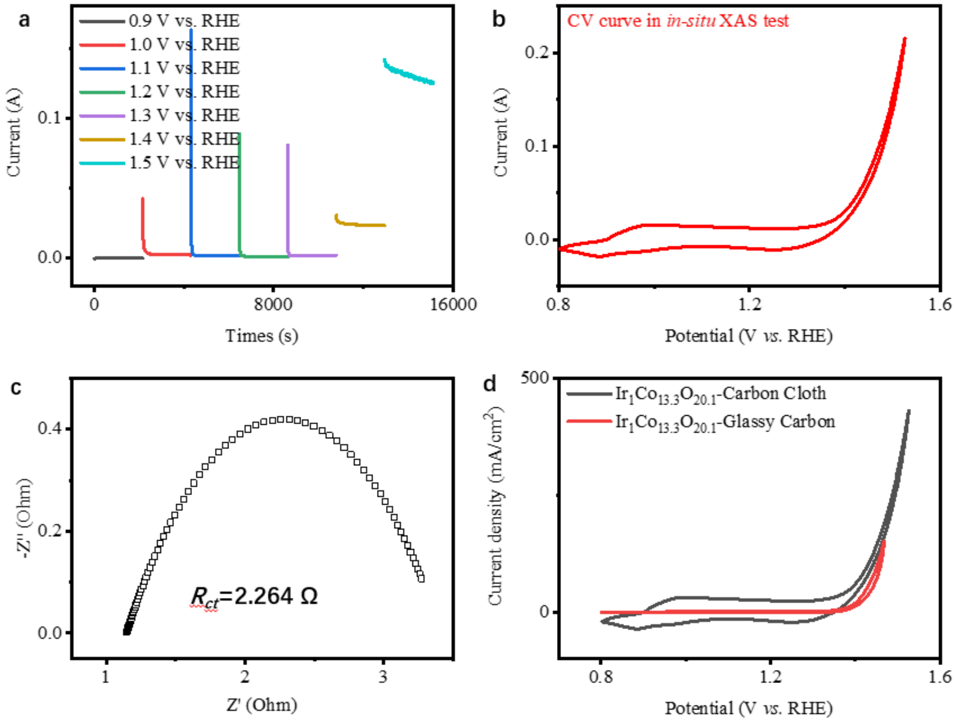

Figure 6.26 Electrochemical results of $Ir_1Co_{13.3}O_{20.1}$ ANSs during in-situ XAS. Current transients (a), cyclic voltammetry (b), impedance data (c), and cyclic voltammetry curve comparison.

The OER stability is decreased quickly at high potential of 1.5 V vs. RHE, more likely because of the catalysts shedding from hydrophobic Carbon Cloth, and thus leading to the OER activity loss. As shown in Figure R22d, the OER activity of $Ir_1Co_{13.3}O_{20.1}$-Carbon Cloth is similar with $Ir_1Co_{13.3}O_{20.1}$-Glassy Carbon. The larger CV integration area of $Ir_1Co_{13.3}O_{20.1}$-Carbon Cloth may be resulted by the giant double layer capacitance and lager ECSA, because lot of catalysts have been loaded onto Carbon Cloth.

Chapter 7. Conclusion and Future Work

We have built an *operando* XAS reaction cell to investigate the electrocatalyst during the ORR and OER. The Combination of the electrochemical tests, other lab-based characterizations such as XPS, XRD, and SEM, and DFT, we have built a systematic study of different types of electrocatalysts, including low-cost TMs and expensive noble metals. For moderate stable perovskite oxides, soft XAS results indicate that the ORR catalytic activity of Fe-substituted $LaCoO_3$ and the reaction mechanism are attributed to the optimized e_g filling numbers and the stronge hybridization of transition metal 3*d* and oxygen 2*p* bands. Combining with hard XAS, XRD, and DFT, the improved OER activity of Fe and Co co-substituted $LaCoO_3$ OER was also explained by the strong hybridization of transition metal 3*d* and oxygen 2*p* bands. For unstable electrocatalysts, the *operando* hard XAS and Raman spectroscopy suggested that Co_9S_8 ultimately converts to oxide cluster (CoO_x) containing six oxygen coordinated Co octahedra as the basic unit which is the true catalytic center to promote high OER activity. The density functional theory (DFT) calculations verify the *in-situ* generated CoO_x consisting of edge-sharing CoO_6 octahedron clusters as the actual active sites. Furthermore, we applied the *operando* hard XAS to study atomically dispersed Ir catalysts on amorphous CoO, which demonstrated that the *in-situ* formed Ir–O–Co bonding gets preferentially oxidized at a lower overpotential, magnifying the OER activity. By comparing all those materials together, we find that the edge-sharing octahedral structure is a unified unit in all those materials under the oxygen associated catalytic reaction conditions. Those unified unit also contains the previous proposed reaction units in table 5.2. Our collaborated work also indicates that Ru-O-TM and Ir-O-TM bonds would form in an edge-sharing octahedral unit, which acts as the catalytic active center.[82, 159]

Overall, we propose that the edge-sharing octahedral structure is the unified primary reaction units for ORR and OER. By altering the composition of edge-sharing octahedral units, we could alter the electronic structure and bonding covalency, which changes the absorption energy of the OH group to improve the catalytic activity. Our findings and strategy on identifying both TM X-ides and noble metal oxides active sites could aid future research in developing advanced electrocatalysts for energy conversion and storage systems.

In the future, we would like to perform studies on other types of ORR electrocatalysts (e.g., unstable perovskite oxides). Also, we will work with the theoretical group by using current summarized results to perform machine learning studies and find out ideal edge-sharing octahedral units. Following the guideline from the theoretical modeling, we would try to synthesize such materials to check both ORR and OER performance, promoting the development of a renewable energy system.

Bibliography

1. Weng, Z.; Wu, Y. S.; Wang, M. Y.; Jiang, J. B.; Yang, K.; Huo, S. J.; Wang, X. F.; Ma, Q.; Brudvig, G. W.; Batista, V. S.; Liang, Y. Y.; Feng, Z. X.; Wang, H. L., Active Sites of Copper-complex Catalytic Materials for Electrochemical Carbon Dioxide Reduction. *Nature Communications* **2018,** *9*, 415.
2. Weng, Z.; Jing, J. B.; Wu, Y. S.; Wu, Z. S.; Guo, X. T.; Materna, K. L.; Liu, W.; Batista, V. S.; Brudvig, G. W.; Wang, H. L., Electrochemical CO_2 Reduction to Hydrocarbons on a Heterogeneous Molecular Cu Catalyst in Aqueous Solution. *J Am Chem Soc* **2016,** *138* (26), 8076-8079.
3. Wu, Y. S.; Jiang, J. B.; Weng, Z.; Wang, M. Y.; Broere, D. L. J.; Zhong, Y. R.; Brudvig, G. W.; Feng, Z. X.; Wang, H. L., Electroreduction of CO_2 Catalyzed by a Heterogenized Zn-Porphyrin Complex with a Redox-Innocent Metal Center. *ACS Central Science* **2017,** *3* (8), 847-852.
4. Kornienko, N.; Zhao, Y. B.; Kiley, C. S.; Zhu, C. H.; Kim, D.; Lin, S.; Chang, C. J.; Yaghi, O. M.; Yang, P. D., Metal-Organic Frameworks for Electrocatalytic Reduction of Carbon Dioxide. *J Am Chem Soc* **2015,** *137* (44), 14129-14135.
5. Cheriti, M.; Kahoul, A., Double Perovskite Oxides Sr_2MMoO_6 (M = Fe and Co) as Cathode Materials for Oxygen Reduction in Alkaline Medium. *Mater Res Bull* **2012,** *47*, 135-141.
6. Suntivich, J.; Hong, W. T.; Lee, Y. L.; Rondinelli, J. M.; Yang, W. L.; Goodenough, J. B.; Dabrowski, B.; Freeland, J. W.; Shao-Horn, Y., Estimating Hybridization of Transition Metal and Oxygen States in Perovskites, from O K-edge X-ray Absorption Spectroscopy. *J Phys Chem C* **2014,** *118*, 1856-1863.
7. Diaz-Morales, O.; Raaijman, S.; Kortlever, R.; Kooyman, P. J.; Wezendonk, T.; Gascon, J.; Fu, W. T.; Koper, M. T. M., Iridium-based double perovskites for efficient water oxidation in acid media. *Nature Communications* **2016,** *7*, 12363.
8. Wygant, B. R.; Kawashima, K.; Mullins, C. B., Catalyst or Precatalyst? The Effect of Oxidation on Transition Metal Carbide, Pnictide, and Chalcogenide Oxygen Evolution Catalysts. *ACS Energy Lett* **2018,** *3* (12), 2956-2966.
9. Wei, C.; Feng, Z. X.; Scherer, G. G.; Barber, J.; Shao-Horn, Y.; Xu, Z. C. J., Cations in Octahedral Sites: A Descriptor for Oxygen Electrocatalysis on Transition-Metal Spinels. *Advanced Materials* **2017,** *29* (23).
10. Xie, X.; He, C.; Li, B.; He, Y.; Cullen, D. A.; Wegener, E. C.; Kropf, A. J.; Martinez, U.; Cheng, Y.; Engelhard, M. H.; Bowden, M. E.; Song, M.; Lemmon, T.; Li, X. S.; Nie, Z.; Liu, J.; Myers, D. J.; Zelenay, P.; Wang, G.; Wu, G.; Ramani, V.; Shao, Y., Performance enhancement and degradation mechanism identification of a single-atom Co–N–C catalyst for proton exchange membrane fuel cells. *Nat Catal* **2020,** *3* (12), 1044-1054.
11. Stamenkovic, V.; Mun, B. S.; Mayrhofer, K. J. J.; Ross, P. N.; Markovic, N. M.; Rossmeisl, J.; Greeley, J.; Norskov, J. K., Changing the activity of electrocatalysts for oxygen reduction by tuning the surface electronic structure. *Angew Chem Int Edit* **2006,** *45*, 2897-2901.
12. Duan, Y.; Sun, S. N.; Xi, S. B.; Ren, X.; Zhou, Y.; Zhang, G. L.; Yang, H. T.; Du, Y. H.; Xu, Z. C. J., Tailoring the Co 3d-O 2p Covalency in $LaCoO_3$ by Fe Substitution To Promote Oxygen Evolution Reaction. *Chemistry of Materials* **2017,** *29* (24), 10534-10541.
13. Zhang, H. G.; Hwang, S.; Wang, M. Y.; Feng, Z. X.; Karakalos, S.; Luo, L. L.; Qiao, Z.; Xie, X. H.; Wang, C. M.; Su, D.; Shao, Y. Y.; Wu, G., Single Atomic Iron Catalysts for

Oxygen Reduction in Acidic Media: Particle Size Control and Thermal Activation. *J Am Chem Soc* **2017,** *139* (40), 14143-14149.

14. Zhang, X.; Wu, Z. S.; Zhang, X.; Li, L. W.; Li, Y. Y.; Xu, H. M.; Li, X. X.; Yu, X. L.; Zhang, Z. S.; Liang, Y. Y.; Wang, H. L., Highly selective and active CO_2 reduction electro-catalysts based on cobalt phthalocyanine/carbon nanotube hybrid structures. *Nature Communications* **2017,** *8*, 14675.

15. Suntivich, J.; Gasteiger, H. A.; Yabuuchi, N.; Nakanishi, H.; Goodenough, J. B.; Shao-Horn, Y., Design Principles for Oxygen-Reduction Activity on Perovskite Oxide Catalysts for Fuel Cells and Metal-Air Batteries. *Nat Chem* **2011,** *3*, 647-647.

16. Suntivich, J.; May, K. J.; Gasteiger, H. A.; Goodenough, J. B.; Shao-Horn, Y., A Perovskite Oxide Optimized for Oxygen Evolution Catalysis from Molecular Orbital Principles. *Science* **2011,** *334* (6061), 1383.

17. Gong, X.; Wang, Z.; Zhao, L.; Zhang, S.; Wang, D.; Wang, M., Competition of Oxygen Evolution and Desulfurization for Bauxite Electrolysis. *Industrial & Engineering Chemistry Research* **2017,** *56*, 6036-6144.

18. Grimaud, A.; Demortière, A.; Saubanère, M.; Dachraoui, W.; Duchamp, M.; Doublet, M.-L.; Tarascon, J.-M., Activation of Surface Oxygen Sites on an Iridium-based Model Catalyst for the Oxygen Evolution Reaction. Nature Energy, **2016,** *2*, 16189.

19. Kim, J. G.; Kim, Y.; Noh, Y.; Lee, S.; Kim, Y.; Kim, W. B., Bifunctional Hybrid Catalysts with Perovskite LaCo0.8Fe0.2O3 Nanowires and Reduced Graphene Oxide Sheets for an Efficient LiO_2 Battery Cathode. *ACS Applied Materials & Interfaces* **2018,** *10* (6), 5429-5439.

20. Li, H.; Chen, S.; Jia, X.; Xu, B.; Lin, H.; Yang, H.; Song, L.; Wang, X., Amorphous nickel-cobalt complexes hybridized with 1T-phase molybdenum disulfide via hydrazine-induced phase transformation for water splitting. *Nature Communications* **2017,** *8*, 15377.

21. Wang, Z. L.; Xu, D.; Xu, J. J.; Zhang, X. B., Oxygen Electrocatalysts in Metal-air Batteries: from Aqueous to Nonaqueous Electrolytes. *Chem Soc Rev* **2014,** *43*, 7746-7786.

22. Wei, C.; Feng, Z.; Scherer, G. G.; Barber, J.; Shao-Horn, Y.; Xu, Z. J., Cations in Octahedral Sites: A Descriptor for Oxygen Electrocatalysis on Transition-Metal Spinels. *Adv. Mater.* **2017,** *29* (23), 0935-9648.

23. Wang, Y. F.; Sun, D.; Wang, M. Y.; Feng, Z. X.; Hall, A. S., Oxygen Reduction Electrocatalysis on Ordered Intermetallic Pd-Bi Electrodes Is Enhanced by a Low Coverage of Spectator Species. *J Phys Chem C* **2020,** *124* (9), 5220-5224.

24. Cai, C.; Wang, M. Y.; Han, S. B.; Wang, Q.; Zhang, Q.; Zhu, Y. M.; Yang, X. M.; Wu, D. J.; Zu, X. T.; Sterbinsky, G. E.; Feng, Z. X.; Gu, M., Ultrahigh Oxygen Evolution Reaction Activity Achieved Using Ir Single Atoms on Amorphous CoOx Nanosheets. *ACS Catalysis* **2021,** *11* (1), 123-130.

25. Cai, Z.; Zhou, D. J.; Wang, M. Y.; Bak, S. M.; Wu, Y. S.; Wu, Z. S.; Tian, Y.; Xiong, X. Y.; Li, Y. P.; Liu, W.; Siahrostami, S.; Kuang, Y.; Yang, X. Q.; Duan, H. H.; Feng, Z. X.; Wang, H. L.; Sun, X. M., Introducing Fe^{2+} into Nickel-Iron Layered Double Hydroxide: Local Structure Modulated Water Oxidation Activity. *Angew Chem Int Edit* **2018,** *57*, 9392-9396.

26. Bunker, G., Introduction to XAFS : a Practical Guide to X-ray Absorption Fine Structure Spectroscopy. **2010**.

27. Calvin, S., XAFS for Everyone. **2018**.

28. Schnohr, C. S.; Ridgway, M. C., *X-Ray Absorption Spectroscopy of Semiconductors*. 2015.

29. Koningsberger, D. C.; Prins, R., *X-ray absorption : principles, applications, techniques of EXAFS, SEXAFS, and XANES*. John Wiley & Sons: New York, 1988.

30. Rehr, J. J.; Albers, R. C., Theoretical approaches to x-ray absorption fine structure. *Rev Mod Phys* **2000,** *72* (3), 621-654.

31. Rehr, J. J.; Ankudinov, A. L., Progress in the theory and interpretation of XANES. *Coordin Chem Rev* **2005,** *249* (1-2), 131-140.

32. Boscherini, F., X-Ray Absorption Fine Structure in the Study of Semiconductor Heterostructures and Nanostructures. **2013**, 259-310.

33. McMorrow, D.; Als-Nielsen, J., Elements of modern x-ray physics. **2013**.

34. Rehr, J. J.; Kas, J. J.; Vila, F. D.; Prange, M. P.; Jorissen, K., Parameter-free calculations of X-ray spectra with FEFF9. *Phys Chem Chem Phys* **2010,** *12* (21), 5503-5513.

35. Wang, M. Y.; Arnadottir, L.; Xu, Z. C. J.; Feng, Z. X., In Situ X-ray Absorption Spectroscopy Studies of Nanoscale Electrocatalysts. *Nano-Micro Lett* **2019,** *11* (1), 47.

36. Seidler, G. T.; Mortensen, D. R.; Remesnik, A. J.; Pacold, J. I.; Ball, N. A.; Barry, N.; Styczinski, M.; Hoidn, O. R., A laboratory-based hard x-ray monochromator for high-resolution x-ray emission spectroscopy and x-ray absorption near edge structure measurements. *Rev Sci Instrum* **2014,** *85* (11), 3906.

37. Williams, A., Laboratory X-Ray Spectrometer for Exafs and Xanes Measurements. *Rev Sci Instrum* **1983,** *54* (2), 193-197.

38. Wang, D. N.; Zhou, J. G.; Hu, Y. F.; Yang, J. L.; Han, N.; Li, Y. G.; Sham, T. K., In Situ X-ray Absorption Near-Edge Structure Study of Advanced $NiFe(OH)_x$ Electrocatalyst on Carbon Paper for Water Oxidation. *J Phys Chem C* **2015,** *119* (34), 19573-19583.

39. Fottinger, K.; van Bokhoven, J. A.; Nachtegaal, M.; Rupprechter, G., Dynamic Structure of a Working Methanol Steam Reforming Catalyst: In Situ Quick-EXAFS on Pd/ZnO Nanoparticles. *J Phys Chem Lett* **2011,** *2* (5), 428-433.

40. Li, H. Y.; Sun, S. N.; Xi, S. B.; Chen, Y. B.; Wang, T.; Du, Y. H.; Sherburne, M.; Ager, J. W.; Fisher, A. C.; Xu, Z. C. J., Metal-Oxygen Hybridization Determined Activity in Spinel-Based Oxygen Evolution Catalysts: A Case Study of $ZnFe_{2-x}Cr_xO_4$. *Chemistry of Materials* **2018,** *30*, 6839-6848.

41. Fabbri, E.; Mohamed, R.; Levecque, P.; Conrad, O.; Kotz, R.; Schmidt, T. J., Composite Electrode Boosts the Activity of $Ba_{0.5}Sr_{0.5}Co_{0.8}Fe_{0.2}O_{3\text{-delta}}$ Perovskite and Carbon toward Oxygen Reduction in Alkaline Media. *ACS Catalysis* **2014,** *4*, 1061-1070.

42. Mueller, D. N.; Machala, M. L.; Bluhm, H.; Chueh, W. C., Redox Activity of Surface Oxygen Anions in Oxygen-deficient Perovskite Oxides during Electrochemical Reactions. *Nature Communications* **2015,** *6*, 6097.

43. Hwang, J.; Rao, R. R.; Giordano, L.; Katayama, Y.; Yu, Y.; Shao-Horn, Y., Perovskites in catalysis and electrocatalysis. *Science* **2017,** *358*, 751-756.

44. Cho, S. A.; Jang, Y. J.; Lim, H. D.; Lee, J. E.; Jang, Y. H.; Nguyen, T. T. H.; Mota, F. M.; Fenning, D. P.; Kang, K.; Shao-Horn, Y.; Kim, D. H., Hierarchical Porous Carbonized Co3O4 Inverse Opals via Combined Block Copolymer and Colloid Templating as Bifunctional Electrocatalysts in LiO_2 Battery. *Adv Energy Mater* **2017,** *7*, 00391.

45. Duan, Y.; Sun, S. N.; Xi, S. B.; Ren, X.; Zhou, Y.; Zhang, G. L.; Yang, H. T.; Du, Y. H.; Xu, Z. C. J., Tailoring the Co 3d-O 2p Covalency in $LaCoO_3$ by Fe Substitution to Promote Oxygen Evolution Reaction. *Chemistry of Materials* **2017,** *29*, 10534-10541.

46. Deng, J.; Lo, Y. H.; Gallagher-Jones, M.; Chen, S.; Pryor, A.; Jin, Q.; Hong, Y. P.; Nashed, Y. S. G.; Vogt, S.; Miao, J.; Jacobsen, C., Correlative 3D x-ray Fluorescence and Ptychographic Tomography of Frozen-hydrated Green Algae. *Science Advances* **2018,** *4*, 4548.

47. Deng, J. J.; Vine, D. J.; Chen, S.; Nashed, Y. S. G.; Jin, Q. L.; Phillips, N. W.; Peterka, T.; Rossc, R.; Vogt, S.; Jacobsen, C. J., Simultaneous Cryo X-ray Ptychographic and Fluorescence Microscopy of Green Algae. *P Natl Acad Sci USA* **2015,** *112*, 2314-2319.

48. Pfeiffer, F., X-ray Ptychography. *Nat Photonics* **2018,** *12*, 9-17.

49. Sun, S. N.; Li, H. Y.; Xu, Z. C. J., Impact of Surface Area in Evaluation of Catalyst Activity. *Joule* **2018,** *2*, 1024-1027.

50. Wroblowa, H. S.; Pan, Y. C.; Razumney, G., Electroreduction of Oxygen - New Mechanistic Criterion. *J Electroanal Chem* **1976,** *69*, 195-201.

51. Haverkort, M. W.; Hu, Z.; Cezar, J. C.; Burnus, T.; Hartmann, H.; Reuther, M.; Zobel, C.; Lorenz, T.; Tanaka, A.; Brookes, N. B.; Hsieh, H. H.; Lin, H. J.; Chen, C. T.; Tjeng, L. H., Spin State Transition in $LaCoO_3$ Studied Using Soft X-ray Absorption Spectroscopy and Magnetic Circular Dichroism. *Phys Rev Lett* **2006,** *97*, 176405.

52. Kumagai, Y.; Ikeno, H.; Oba, F.; Matsunaga, K.; Tanaka, I., Effects of Crystal Structure on Co-L(2,3) X-ray Absorption Near-edge Structure and Electron-energy-loss Near-edge Structure of Trivalent Cobalt Oxides. *Phys Rev B* **2008,** *77*, 155124.

53. Hocking, R. K.; George, S. D.; Raymond, K. N.; Hodgson, K. O.; Hedman, B.; Solomon, E. I., Fe L-Edge X-ray Absorption Spectroscopy Determination of Differential Orbital Covalency of Siderophore Model Compounds: Electronic Structure Contributions to High Stability Constants. *J Am Chem Soc* **2010,** *132*, 4006-4015.

54. Anjum, G.; Kumar, R.; Mollah, S.; Thakur, P.; Gautam, S.; Chae, K. H., NEXAFS Studies of $La_{0.8}Bi_{0.2}Fe_{1-x}Mn_xO_3$(0.0 <= x <= 0.4) Multiferroic System Using X-ray Absorption Spectroscopy. *J Phys D Appl Phys* **2011,** *44*, 075403.

55. Toulemonde, O.; N'Guyen, N.; Studer, F.; Traverse, A., Spin State Transition in $LaCoO_3$ with Temperature or Strontium Doping as Seen by XAS. *J Solid State Chem* **2001,** *158*, 208-217.

56. Lafuerza, S.; Subias, G.; Garcia, J.; Di Matteo, S.; Blasco, J.; Cuartero, V.; Natoli, C. R., Origin of the Pre-peak Features in the Xxygen K-edge X-ray Absorption Spectra of $LaFeO_3$ and $LaMnO_3$ Studied by Ga Substitution of the Transition Metal Ion. *J Phys-Condens Mat* **2011,** *23*, 325601.

57. Mcintyre, N. S.; Zetaruk, D. G., X-Ray Photoelectron Spectroscopic Studies of Iron-Oxides. *Anal Chem* **1977,** *49*, 1521-1529.

58. Wang, K. X.; Niu, H. L.; Chen, J. S.; Song, J. M.; Mao, C. J.; Zhang, S. Y.; Zheng, S. J.; Liu, B. Z.; Chen, C. L., Facile Synthesis of CeO_2-$LaFeO_3$ Perovskite Composite and Its Application for 4-(Methylnitrosamino)-1-(3-Pyridyl)-1-Butanone (NNK) Degradation. *Materials* **2016,** *9*, 326.

59. Wasinger, E. C.; de Groot, F. M. F.; Hedman, B.; Hodgson, K. O.; Solomon, E. I., L-edge X-ray Absorption Spectroscopy of Non-heme Iron Sites: Experimental Determination of Differential Orbital Covalency. *J Am Chem Soc* **2003,** *125*, 12894-12906.

60. Miedema, P. S.; de Groot, F. M. F., The Iron L edges: Fe 2p X-ray Absorption and Electron Energy Loss Spectroscopy. *J Electron Spectrosc* **2013,** *187*, 32-48.

61. Zhu, Y. L.; Zhou, W.; Yu, J.; Chen, Y. B.; Liu, M. L.; Shao, Z. P., Enhancing Electrocatalytic Activity of Perovskite Oxides by Tuning Cation Deficiency for Oxygen Reduction and Evolution Reactions. *Chemistry of Materials* **2016,** *28* (6), 1691-1697.

62. Nashed, Y. S. G.; Vine, D. J.; Peterka, T.; Deng, J. J.; Ross, R.; Jacobsen, C., Parallel Ptychographic Reconstruction. *Opt Express* **2014,** *22*, 32082-32097.

63. Zhang, X.; Zhang, X.; Xu, H. M.; Wu, Z. S.; Wang, H. L.; Liang, Y. Y., Iron-Doped Cobalt Monophosphide Nanosheet/ Carbon Nanotube Hybrids as Active and Stable Electrocatalysts for Water Splitting. *Adv Funct Mater* **2017,** *27* (24), 06635.

64. De Silva, U.; Masud, J.; Zhang, N.; Hong, Y.; Liyanage, W. P. R.; Zaeem, M. A.; Nath, M., Nickel telluride as a bifunctional electrocatalyst for efficient water splitting in alkaline medium. *Journal of Materials Chemistry A* **2018,** *6* (17), 7608-7622.

65. Kim, J. H.; Kawashima, K.; Wygant, B. R.; Mabayoje, O.; Liu, Y.; Wang, J. H.; Mullins, C. B., Transformation of a Cobalt Carbide (Co_3C) Oxygen Evolution Precatalyst. *ACS Appl Energ Mater* **2018,** *1* (10), 5145-5150.

66. Zhang, Y. K.; Wu, C. Q.; Jiang, H. L.; Lin, Y. X.; Liu, H. J.; He, Q.; Chen, S. M.; Duan, T.; Song, L., Atomic Iridium Incorporated in Cobalt Hydroxide for Efficient Oxygen Evolution Catalysis in Neutral Electrolyte. *Advanced Materials* **2018,** *30* (18), 07522.

67. Li, P.; Wang, M.; Duan, X.; Zheng, L.; Cheng, X.; Zhang, Y.; Kuang, Y.; Li, Y.; Ma, Q.; Feng, Z.; Liu, W.; Sun, X., Boosting oxygen evolution of single-atomic ruthenium through electronic coupling with cobalt-iron layered double hydroxides. *Nature Communications* **2019,** *10* (1), 1711.

68. Zhu, Y. L.; Zhou, W.; Sunarso, J.; Zhong, Y. J.; Shao, Z. P., Phosphorus-Doped Perovskite Oxide as Highly Efficient Water Oxidation Electrocatalyst in Alkaline Solution. *Adv Funct Mater* **2016,** *26* (32), 5862-5872.

69. Zhang, W. H.; Zhou, W. L.; Zhang, Z. B.; Chen, Z. L.; Tan, S. Z.; Chen, D. J., Selective Partial Substitution of B-Site with Phosphorus in Perovskite Electrocatalysts for Highly Efficient Oxygen Evolution Reaction. *Chemnanomat* **2019,** *5* (3), 352-357.

70. Wang, M.; Feng, Z., Pitfalls in X-ray Absorption Spectroscopy Analysis and Interpretation: A Practical Guide for General Users. *Curr Opin Electroche* **2021**, 100803.

71. Tian, H. J.; Li, Z.; Feng, G. X.; Yang, Z. Z.; Fox, D.; Wang, M. Y.; Zhou, H.; Zhai, L.; Kushima, A.; Du, Y. G.; Feng, Z. X.; Shan, X. N.; Yang, Y., Stable, high-performance, dendrite-free, seawater-based aqueous batteries. *Nature Communications* **2021,** *12* (1), 237.

72. Timoshenko, J.; Cuenya, B. R., In Situ/Operando Electrocatalyst Characterization by X-ray Absorption Spectroscopy. *Chem Rev* **2021,** *121* (2), 882-961.

73. Xiao, Z.; Huang, Y.-C.; Dong, C.-L.; Xie, C.; Liu, Z.; Du, S.; Chen, W.; Yan, D.; Tao, L.; Shu, Z.; Zhang, G.; Duan, H.; Wang, Y.; Zou, Y.; Chen, R.; Wang, S., Operando Identification of the Dynamic Behavior of Oxygen Vacancy-Rich Co_3O_4 for Oxygen Evolution Reaction. *J Am Chem Soc* **2020,** *28* (142), 12087-12095.

74. May, K. J.; Carlton, C. E.; Stoerzinger, K. A.; Risch, M.; Suntivich, J.; Lee, Y. L.; Grimaud, A.; Shao-Horn, Y., Influence of Oxygen Evolution during Water Oxidation on the Surface of Perovskite Oxide Catalysts. *J Phys Chem Lett* **2012,** *3* (22), 3264-3270.

75. Frati, F.; Hunault, M. O. J. Y.; de Groot, F. M. F., Oxygen K-edge X-ray Absorption Spectra. *Chem Rev* **2020,** *120* (9), 4056-4110.

76. Sultan, K.; Ikram, M.; Gautam, S.; Lee, H.-K.; Chae, K. H.; Asokan, K., Electrical and magnetic properties of the pulsed laser deposited Ca doped $LaMnO_3$ thin films on Si (100) and their electronic structures. *Rsc Adv* **2015,** *5* (85), 69075-69085.

77. Wang, M. Y.; Han, B. H.; Deng, J. J.; Jiang, Y.; Zhou, M. Y.; Lucero, M.; Wang, Y.; Chen, Y. B.; Yang, Z. Z.; N'Diaye, A. T.; Wang, Q.; Xu, Z. C. J.; Feng, Z. X., Influence of Fe

Substitution into $LaCoO_3$ Electrocatalysts on Oxygen-Reduction Activity. *ACS Applied Materials & Interfaces* **2019,** *11* (6), 5682-5686.

78. Suntivich, J.; Hong, W. T.; Lee, Y.-L.; Rondinelli, J. M.; Yang, W.; Goodenough, J. B.; Dabrowski, B.; Freeland, J. W.; Shao-Horn, Y., Estimating Hybridization of Transition Metal and Oxygen States in Perovskites from O K-edge X-ray Absorption Spectroscopy. *The Journal of Physical Chemistry C* **2014,** *118* (4), 1856-1863.

79. Bockris, J. O. M.; Otagawa, T., The electrocatalysis of oxygen evolution on perovskites. *Journal of The Electrochemical Society* **1984,** *131* (2), 290.

80. Zhao, S.; Yan, L. T.; Luo, H. M.; Mustain, W.; Xu, H., Recent progress and perspectives of bifunctional oxygen reduction/evolution catalyst development for regenerative anion exchange membrane fuel cells. *Nano Energy* **2018,** *47*, 172-198.

81. Fabbri, E.; Habereder, A.; Waltar, K.; Kotz, R.; Schmidt, T. J., Developments and perspectives of oxide-based catalysts for the oxygen evolution reaction. *Catalysis Science & Technology* **2014,** *4* (11), 3800-3821.

82. Li, P. S.; Wang, M. Y.; Duan, X. X.; Zheng, L. R.; Cheng, X. P.; Zhang, Y. F.; Kuang, Y.; Li, Y. P.; Ma, Q.; Feng, Z. X.; Liu, W.; Sun, X. M., Boosting oxygen evolution of single-atomic ruthenium through electronic coupling with cobalt-iron layered double hydroxides. *Nature Communications* **2019,** *10*, 1711.

83. Norskov, J. K.; Bligaard, T.; Rossmeisl, J.; Christensen, C. H., Towards the computational design of solid catalysts. *Nat Chem* **2009,** *1* (1), 37-46.

84. Munnik, P.; de Jongh, P. E.; de Jong, K. P., Recent Developments in the Synthesis of Supported Catalysts. *Chem Rev* **2015,** *115* (14), 6687-6718.

85. Wang, M.; Feng, Z., Interfacial Processes in Electrochemical Energy Systems. *Chem Commun* **2021**, 1703.

86. Seitz, L. C.; Dickens, C. F.; Nishio, K.; Hikita, Y.; Montoya, J.; Doyle, A.; Kirk, C.; Vojvodic, A.; Hwang, H. Y.; Norskov, J. K.; Jaramillo, T. F., A highly active and stable $IrO_x/SrIrO_3$ catalyst for the oxygen evolution reaction. *Science* **2016,** *353* (6303), 1011-1014.

87. Bergmann, A.; Jones, T. E.; Moreno, E. M.; Teschner, D.; Chernev, P.; Gliech, M.; Reier, T.; Dau, H.; Strasser, P., Unified structural motifs of the catalytically active state of Co(oxyhydr)oxides during the electrochemical oxygen evolution reaction. *Nat Catal* **2018,** *1* (9), 711-719.

88. Kanan, M. W.; Yano, J.; Surendranath, Y.; Dinca, M.; Yachandra, V. K.; Nocera, D. G., Structure and Valency of a Cobalt-Phosphate Water Oxidation Catalyst Determined by in Situ X-ray Spectroscopy. *J Am Chem Soc* **2010,** *132* (39), 13692-13701.

89. Nilsson, A.; LaRue, J.; Oberg, H.; Ogasawara, H.; Dell'Angela, M.; Beye, M.; Ostrom, H.; Gladh, J.; Norskov, J. K.; Wurth, W.; Abild-Pedersen, F.; Pettersson, L. G. M., Catalysis in real time using X-ray lasers. *Chem Phys Lett* **2017,** *675*, 145-173.

90. Feng, Z. X.; Lu, J. L.; Feng, H.; Stair, P. C.; Elam, J. W.; Bedzyk, M. J., Catalysts Transform While Molecules React: An Atomic-Scale View. *J Phys Chem Lett* **2013,** *4* (2), 285-291.

91. Stoerzinger, K. A.; Hong, W. T.; Crumlin, E. J.; Bluhm, H.; Shao-Horn, Y., Insights into Electrochemical Reactions from Ambient Pressure Photoelectron Spectroscopy. *Accounts Chem Res* **2015,** *48* (11), 2976-2983.

92. Liu, X. S.; Yang, W. L.; Liu, Z., Recent Progress on Synchrotron-Based In-Situ Soft X-ray Spectroscopy for Energy Materials. *Advanced Materials* **2014,** *26* (46), 7710-7729.

93. Feng, Z. X.; Hong, W. T.; Fong, D. D.; Lee, Y. L.; Yacoby, Y.; Morgan, D.; Shao-Horn, Y., Catalytic Activity and Stability of Oxides: The Role of Near-Surface Atomic Structures and Compositions. *Accounts Chem Res* **2016,** *49* (5), 966-973.

94. Li, H.; Guo, Z.; Wang, X. W., Atomic-layer-deposited ultrathin Co_9S_8 on carbon nanotubes: an efficient bifunctional electrocatalyst for oxygen evolution/reduction reactions and rechargeable Zn-air batteries. *Journal of Materials Chemistry A* **2017,** *5* (40), 21353-21361.

95. Kim, M. H.; Smith, V. P.; Hong, T. K., 1st-Order and 2nd-Order Derivative Polarography Voltammetry for Reversible, Quasi-Reversible, and Irreversible Electrode Processes. *J Electrochem Soc* **1993,** *140* (3), 712-721.

96. Espinoza, E. M.; Clark, J. A.; Soliman, J.; Derr, J. B.; Morales, M.; Vullev, V. I., Practical Aspects of Cyclic Voltammetry: How to Estimate Reduction Potentials When Irreversibility Prevails. *J Electrochem Soc* **2019,** *166* (5), H3175-H3187.

97. Burke, M. S.; Kast, M. G.; Trotochaud, L.; Smith, A. M.; Boettcher, S. W., Cobalt-Iron (Oxy)hydroxide Oxygen Evolution Electrocatalysts: The Role of Structure and Composition on Activity, Stability, and Mechanism. *J Am Chem Soc* **2015,** *137* (10), 3638-3648.

98. Liu, K. W.; Zhang, C. L.; Sun, Y. D.; Zhang, G. H.; Shen, X. C.; Zou, F.; Zhang, H. C.; Wu, Z. W.; Wegener, E. C.; Taubert, C. J.; Miller, J. T.; Peng, Z. M.; Zhu, Y., High-Performance Transition Metal Phosphide Alloy Catalyst for Oxygen Evolution Reaction. *ACS Nano* **2018,** *12* (1), 158-167.

99. Gerken, J. B.; McAlpin, J. G.; Chen, J. Y. C.; Rigsby, M. L.; Casey, W. H.; Britt, R. D.; Stahl, S. S., Electrochemical Water Oxidation with Cobalt-Based Electrocatalysts from pH 0–14: The Thermodynamic Basis for Catalyst Structure, Stability, and Activity. *J Am Chem Soc* **2011,** *133* (36), 14431-14442.

100. Moysiadou, A.; Lee, S.; Hsu, C.-S.; Chen, H. M.; Hu, X., Mechanism of Oxygen Evolution Catalyzed by Cobalt Oxyhydroxide: Cobalt Superoxide Species as a Key Intermediate and Dioxygen Release as a Rate-Determining Step. *J Am Chem Soc* **2020,** *142* (27), 11901-11914.

101. Rivas-Murias, B.; Salgueirino, V., Thermodynamic CoO-Co_3O_4 crossover using Raman spectroscopy in magnetic octahedron-shaped nanocrystals. *J Raman Spectrosc* **2017,** *48* (6), 837-841.

102. Liu, Y. C.; Koza, J. A.; Switzer, J. A., Conversion of electrodeposited $Co(OH)_2$ to CoOOH and Co_3O_4, and comparison of their catalytic activity for the oxygen evolution reaction. *Electrochim Acta* **2014,** *140*, 359-365.

103. Yeo, B. S.; Bell, A. T., Enhanced Activity of Gold-Supported Cobalt Oxide for the Electrochemical Evolution of Oxygen. *J Am Chem Soc* **2011,** *133* (14), 5587-5593.

104. Tang, C. W.; Wang, C. B.; Chien, S. H., Characterization of cobalt oxides studied by FT-IR, Raman, TPR and TG-MS. *Thermochim Acta* **2008,** *473* (1-2), 68-73.

105. Yang, J.; Liu, H. W.; Martens, W. N.; Frost, R. L., Synthesis and Characterization of Cobalt Hydroxide, Cobalt Oxyhydroxide, and Cobalt Oxide Nanodiscs. *J Phys Chem C* **2010,** *114* (1), 111-119.

106. Chivot, J.; Mendoza, L.; Mansour, C.; Pauporte, T.; Cassir, M., New insight in the behaviour of Co-H_2Osystem at 25-150 degrees C, based on revised Pourbaix diagrams. *Corros Sci* **2008,** *50* (1), 62-69.

107. Pauporte, T.; Mendoza, L.; Cassir, M.; Bernard, M. C.; Chivot, J., Direct low-temperature deposition of crystallized CoOOH films by potentiostatic electrolysis. *J Electrochem Soc* **2005,** *152* (2), C49-C53.

108. Bergmann, A.; Martinez-Moreno, E.; Teschner, D.; Chernev, P.; Gliech, M.; de Araujo, J. F.; Reier, T.; Dau, H.; Strasser, P., Reversible amorphization and the catalytically active state of crystalline Co_3O_4 during oxygen evolution. *Nature Communications* **2015,** *6*, 8625.

109. Frenkel, A. I., Solving the structure of nanoparticles by multiple-scattering EXAFS analysis. *J Synchrotron Radiat* **1999,** *6*, 293-295.

110. Frenkel, A. I.; Yevick, A.; Cooper, C.; Vasic, R., Modeling the Structure and Composition of Nanoparticles by Extended X-Ray Absorption Fine-Structure Spectroscopy. *Annu Rev Anal Chem* **2011,** *4*, 23-39.

111. Zhou, Y.; Sun, S. N.; Wei, C.; Sun, Y. M.; Xi, P. X.; Feng, Z. X.; Xu, Z. C. J., Significance of Engineering the Octahedral Units to Promote the Oxygen Evolution Reaction of Spinel Oxides. *Advanced Materials* **2019,** *31*, 1902509.

112. Plaisance, C. P.; van Santen, R. A., Structure Sensitivity of the Oxygen Evolution Reaction Catalyzed by Cobalt(II,III) Oxide. *J. Am. Chem. Soc.* **2015,** *137* (46), 14660-14672.

113. Govind Rajan, A.; Martirez, J. M. P.; Carter, E. A., Facet-Independent Oxygen Evolution Activity of Pure β-NiOOH: Different Chemistries Leading to Similar Overpotentials. *J. Am. Chem. Soc.* **2020,** *142* (7), 3600-3612.

114. Li, H.; Gao, Y. H.; Shao, Y. D.; Su, Y. T.; Wang, X. W., Vapor-Phase Atomic Layer Deposition of Co9S8 and Its Application for Supercapacitors. *Nano Lett* **2015,** *15* (10), 6689-6695.

115. Xiong, W.; Guo, Z.; Li, H.; Zhao, R.; Wang, X. W., Rational Bottom-Up Engineering of Electrocatalysts by Atomic Layer Deposition: A Case Study of $Fe_xCo_{1-x}S_y$-Based Catalysts for Electrochemical Hydrogen Evolution. *ACS Energy Letters* **2017,** *2* (12), 2778-2785.

116. Hammer, B.; Hansen, L. B.; Nørskov, J. K., Improved adsorption energetics within density-functional theory using revised Perdew-Burke-Ernzerhof functionals. *Phys. Rev. B* **1999,** *59* (11), 7413-7421.

117. Kresse, G.; Hafner, J., Ab initio molecular-dynamics for liquid-metals. *Phys. Rev. B* **1993,** *47* (1), 558-561.

118. Kresse, G.; Furthmuller, J., Efficient iterative schemes for ab initio total-energy calculations using a plane-wave basis set. *Phys. Rev. B* **1996,** *54* (16), 11169-11186.

119. Blochl, P. E., Projector augmented-wave method. *Phys. Rev. B* **1994,** *50* (24), 17953-17979.

120. Grimme, S.; Antony, J.; Ehrlich, S.; Krieg, H., A consistent and accurate ab initio parametrization of density functional dispersion correction (DFT-D) for the 94 elements H-Pu. *J. Chem. Phys.* **2010,** *132* (15), 154104.

121. Kanan, M. W.; Yano, J.; Surendranath, Y.; Dincă, M.; Yachandra, V. K.; Nocera, D. G., Structure and Valency of a Cobalt−Phosphate Water Oxidation Catalyst Determined by in Situ X-ray Spectroscopy. *J. Am. Chem. Soc.* **2010,** *132* (39), 13692-13701.

122. Peterson, A. A.; Abild-Pedersen, F.; Studt, F.; Rossmeisl, J.; Nørskov, J. K., How copper catalyzes the electroreduction of carbon dioxide into hydrocarbon fuels. *Energy Environ. Sci.* **2010,** *3* (9), 1311-1315.

123. Lee, C. H.; Jun, B.; Lee, S. U., Metal-Free Oxygen Evolution and Oxygen Reduction Reaction Bifunctional Electrocatalyst in Alkaline Media: From Mechanisms to Structure–Catalytic Activity Relationship. *ACS Sustainable Chemistry & Engineering* **2018,** *6* (4), 4973-4980.

124. Wang, J. M.; Cao, F.; Shen, C.; Li, G. Q.; Li, X.; Yang, X.; Li, S.; Qin, G. W., Nanoscale nickel-iron nitride-derived efficient electrochemical oxygen evolution catalysts. *Catal Sci Technol* **2020,** *10* (13), 4458-4466.

125. Zou, X. X.; Wu, Y. Y.; Liu, Y. P.; Liu, D. P.; Li, W.; Gu, L.; Liu, H.; Wang, P. W.; Sun, L.; Zhang, Y., In Situ Generation of Bifunctional, Efficient Fe-Based Catalysts from Mackinawite Iron Sulfide for Water Splitting. *Chem-Us* **2018,** *4* (5), 1139-1152.

126. Zhu, G. X.; Xie, X. L.; Li, X. Y.; Liu, Y. J.; Shen, X. P.; Xu, K. Q.; Chen, S. W., Nanocomposites Based on $CoSe_2$-Decorated $FeSe_2$ Nanoparticles Supported on Reduced Graphene Oxide as High-Performance Electrocatalysts toward Oxygen Evolution Reaction. *ACS Applied Materials & Interfaces* **2018,** *10* (22), 19258-19270.

127. Chen, P. Z.; Xu, K.; Fang, Z. W.; Tong, Y.; Wu, J. C.; Lu, X. L.; Peng, X.; Ding, H.; Wu, C. Z.; Xie, Y., Metallic Co4N Porous Nanowire Arrays Activated by Surface Oxidation as Electrocatalysts for the Oxygen Evolution Reaction. *Angew Chem Int Edit* **2015,** *54* (49), 14710-14714.

128. Chen, W.; Liu, Y. Y.; Li, Y. Z.; Sun, J.; Qiu, Y. C.; Liu, C.; Zhou, G. M.; Cui, Y., In Situ Electrochemically Derived Nanoporous Oxides from Transition Metal Dichalcogenides for Active Oxygen Evolution Catalysts. *Nano Lett* **2016,** *16* (12), 7588-7596.

129. Xu, K.; Ding, H.; Lv, H. F.; Chen, P. Z.; Lu, X. L.; Cheng, H.; Zhou, T. P.; Liu, S.; Wu, X. J.; Wu, C. Z.; Xie, Y., Dual Electrical-Behavior Regulation on Electrocatalysts Realizing Enhanced Electrochemical Water Oxidation. *Advanced Materials* **2016,** *28* (17), 3326-3332.

130. Xu, K.; Chen, P. Z.; Li, X. L.; Tong, Y.; Ding, H.; Wu, X. J.; Chu, W. S.; Peng, Z. M.; Wu, C. Z.; Xie, Y., Metallic Nickel Nitride Nanosheets Realizing Enhanced Electrochemical Water Oxidation. *J Am Chem Soc* **2015,** *137* (12), 4119-4125.

131. Sultana, U. K.; O'Mullane, A. P., Electrochemically Fabricated Ni-P, Ni-S and Ni-Se Materials for Overall Water Splitting: Investigating the Concept of Bifunctional Electrocatalysis. *Chemelectrochem* **2019,** *6* (10), 2630-2637.

132. Wang, Z. C.; Zhang, L. X., In situ growth of NiTe nanosheet film on nickel foam as electrocatalyst for oxygen evolution reaction. *Electrochem Commun* **2018,** *88*, 29-33.

133. Shamraiz, U.; Badshah, A.; Raza, B., Ultrafine alpha-CoOOH Nanorods Activated with Iron for Exceptional Oxygen Evolution Reaction. *Langmuir* **2020,** *36* (9), 2223-2230.

134. Friebel, D.; Louie, M. W.; Bajdich, M.; Sanwald, K. E.; Cai, Y.; Wise, A. M.; Cheng, M. J.; Sokaras, D.; Weng, T. C.; Alonso-Mori, R.; Davis, R. C.; Bargar, J. R.; Norskov, J. K.; Nilsson, A.; Bell, A. T., Identification of Highly Active Fe Sites in (Ni,Fe)OOH for Electrocatalytic Water Splitting. *J Am Chem Soc* **2015,** *137* (3), 1305-1313.

135. Hu, J.; Li, S. W.; Chu, J. Y.; Niu, S. Q.; Wang, J.; Du, Y. C.; Li, Z. H.; Han, X. J.; Xu, P., Understanding the Phase-Induced Electrocatalytic Oxygen Evolution Reaction Activity on FeOOH Nanostructures. *ACS Catalysis* **2019,** *9* (12), 10705-10711.

136. Mattioli, G.; Giannozzi, P.; Bonapasta, A. A.; Guidonili, L., Reaction Pathways for Oxygen Evolution Promoted by Cobalt Catalyst. *J Am Chem Soc* **2013,** *135* (41), 15353-15363.

137. Risch, M.; Khare, V.; Zaharieva, I.; Gerencser, L.; Chernev, P.; Dau, H., Cobalt-Oxo Core of a Water-Oxidizing Catalyst Film. *J Am Chem Soc* **2009,** *131* (20), 6936-+.

138. Risch, M.; Ringleb, F.; Kohlhoff, M.; Bogdanoff, P.; Chernev, P.; Zaharieva, I.; Dau, H., Water oxidation by amorphous cobalt-based oxides: in situ tracking of redox transitions and mode of catalysis. *Energ Environ Sci* **2015,** *8* (2), 661-674.

139. Moysiadou, A.; Lee, S.; Hsu, C. S.; Chen, H. M.; Hu, X. L., Mechanism of Oxygen Evolution Catalyzed by Cobalt Oxyhydroxide: Cobalt Superoxide Species as a Key Intermediate and Dioxygen Release as a Rate-Determining Step. *J Am Chem Soc* **2020,** *142* (27), 11901-11914.

140. Meng, C.; Lin, M. C.; Sun, X. C.; Chen, X. D.; Chen, X. M.; Du, X. W.; Zhou, Y., Laser synthesis of oxygen vacancy-modified CoOOH for highly efficient oxygen evolution. *Chem Commun* **2019,** *55* (20), 2904-2907.

141. Rajan, A. G.; Martirez, J. M. P.; Carter, E. A., Facet-Independent Oxygen Evolution Activity of Pure beta-NiOOH: Different Chemistries Leading to Similar Overpotentials. *J Am Chem Soc* **2020,** *142* (7), 3600-3612.

142. Kim, B.; Oh, A.; Kabiraz, M. K.; Hong, Y.; Joo, J.; Baik, H.; Choi, S. I.; Lee, K., NiOOH Exfoliation-Free Nickel Octahedra as Highly Active and Durable Electrocatalysts Toward the Oxygen Evolution Reaction in an Alkaline Electrolyte. *ACS Applied Materials & Interfaces* **2018,** *10* (12), 10115-10122.

143. Huang, J.; Li, Y.; Zhang, Y.; Rao, G.; Wu, C.; Hu, Y.; Wang, X.; Lu, R.; Li, Y.; Xiong, J., Identification of Key Reversible Intermediates in Self-Reconstructed Nickel-Based Hybrid Electrocatalysts for Oxygen Evolution. *Angew Chem Int Edit* **2019,** *58* (48), 17458-17464.

144. Wang, H. Y.; Hsu, Y. Y.; Chen, R.; Chan, T. S.; Chen, H. M.; Liu, B., Ni3+-Induced Formation of Active NiOOH on the Spinel Ni-Co Oxide Surface for Efficient Oxygen Evolution Reaction. *Adv Energy Mater* **2015,** *5* (10).

145. Zhou, Y. C.; Lopez, N., The Role of Fe Species on NiOOH in Oxygen Evolution Reactions. *ACS Catalysis* **2020,** *10* (11), 6254-6261.

146. Bediako, D. K.; Lassalle-Kaiser, B.; Surendranath, Y.; Yano, J.; Yachandra, V. K.; Nocera, D. G., Structure-Activity Correlations in a Nickel-Borate Oxygen Evolution Catalyst. *J Am Chem Soc* **2012,** *134* (15), 6801-6809.

147. Li, L. F.; Li, Y. F.; Liu, Z. P., Oxygen Evolution Activity on NiOOH Catalysts: Four-Coordinated Ni Cation as the Active Site and the Hydroperoxide Mechanism. *ACS Catalysis* **2020,** *10* (4), 2581-2590.

148. Huang, J.; Chen, J.; Yao, T.; He, J.; Jiang, S.; Sun, Z.; Liu, Q.; Cheng, W.; Hu, F.; Jiang, Y.; Pan, Z.; Wei, S., CoOOH Nanosheets with High Mass Activity for Water Oxidation. *Angewandte Chemie* **2015,** *54* (30), 8722-7.

149. Kwak, I. H.; Im, H. S.; Jang, D. M.; Kim, Y. W.; Park, K.; Lim, Y. R.; Cha, E. H.; Park, J., $CoSe_2$ and $NiSe_2$ Nanocrystals as Superior Bifunctional Catalysts for Electrochemical and Photoelectrochemical Water Splitting. *ACS applied materials & interfaces* **2016,** *8* (8), 5327-34.

150. Zhuang, Z.; Sheng, W.; Yan, Y., Synthesis of Monodispere Au@Co_3O_4 Core-Shell Nanocrystals and Their Enhanced Catalytic Activity for Oxygen Evolution Reaction. *Advanced Materials* **2014,** *26* (23), 3950-3955.

151. Yin, J.; Li, Y.; Lv, F.; Fan, Q.; Zhao, Y.-Q.; Zhang, Q.; Wang, W.; Cheng, F.; Xi, P.; Guo, S., NiO/CoN Porous Nanowires as Efficient Bifunctional Catalysts for Zn-Air Batteries. *ACS nano* **2017,** *11* (2), 2275-2283.

152. Gao, M. R.; Cao, X.; Gao, Q.; Xu, Y. F.; Zheng, Y. R.; Jiang, J.; Yu, S. H., Nitrogen-doped graphene supported $CoSe_2$ nanobelt composite catalyst for efficient water oxidation. *ACS nano* **2014,** *8* (4), 3970-8.

153. Liu, Y.; Jin, Z.; Li, P.; Tian, X.; Chen, X.; Xiao, D., Boron- and Iron-Incorporated α-$Co(OH)_2$

Ultrathin Nanosheets as an Efficient Oxygen Evolution Catalyst. *ChemElectroChem* **2018,** *5* (4), 593-597.

154. Xiao, X.; He, C.-T.; Zhao, S.; Li, J.; Lin, W.; Yuan, Z.; Zhang, Q.; Wang, S.; Dai, L.; Yu, D., A general approach to cobalt-based homobimetallic phosphide ultrathin nanosheets for

highly efficient oxygen evolution in alkaline media. *Energy & Environmental Science* **2017,** *10* (4), 893-899.

155. Li, J.; Zhou, Q.; Zhong, C.; Li, S.; Shen, Z.; Pu, J.; Liu, J.; Zhou, Y.; Zhang, H.; Ma, H., $(Co/Fe)_4O_4$ Cubane-Containing Nanorings Fabricated by Phosphorylating Cobalt Ferrite for Highly Efficient Oxygen Evolution Reaction. *ACS Catalysis* **2019,** *9* (5), 3878-3887.

156. Li, G. L.; Zhang, X. B.; Zhang, H.; Liao, C. Y.; Jiang, G. B., Bottom-up MOF-intermediated synthesis of 3D hierarchical flower-like cobalt-based homobimetallic phophide composed of ultrathin nanosheets for highly efficient oxygen evolution reaction. *Applied Catalysis B-Environmental* **2019,** *249*, 147-154.

157. Babu, D. D.; Huang, Y.; Anandhababu, G.; Wang, X.; Si, R.; Wu, M.; Li, Q.; Wang, Y.; Yao, J., Atomic iridium@cobalt nanosheets for dinuclear tandem water oxidation. *Journal of Materials Chemistry A* **2019,** *7* (14), 8376-8383.

158. Ouyang, T.; Ye, Y. Q.; Wu, C. Y.; Xiao, K.; Liu, Z. Q., Heterostructures Composed of N-Doped Carbon Nanotubes Encapsulating Cobalt and beta-Mo_2C Nanoparticles as Bifunctional Electrodes for Water Splitting. *Angewandte Chemie* **2019,** *58* (15), 4923-4928.

159. Wang, Q.; Huang, X.; Zhao, Z. L.; Wang, M.; Xiang, B.; Li, J.; Feng, Z.; Xu, H.; Gu, M., Ultrahigh-Loading of Ir Single Atoms on NiO Matrix to Dramatically Enhance Oxygen Evolution Reaction. *J Am Chem Soc* **2020,** *142* (16), 7425-7433.

Appendices

Electrochemical Data Analysis

To extract the useful electrochemical data from the measured cyclic voltammetry or linear sweep voltammetry data, the following data analysis need to be done. Since we use the different reference electrode for the different systems (e.g. Ag/AgCl for the acid electrolyte and Hg/HgO for the alkaline electrolyte), we need to convert the reference electrode to the reversible hydrogen electrode (RHE) using Equation 1.

$$\text{Equation 1: } E_{RHE} = E_0 + 0.059 * pH + E_{applied}\ (at\ 25°\text{C})$$

E_0 is the reference standard potential at 25°C in the selected solutions. For example, E_0 is the 0.1971V for the Ag/AgCl in the saturated KCl solutions. $E_{applied}$ is the applied potential in the potentiostat software.

However, the E_0 may vary with time usage or due to different production method. Hence, it is recommended to convert the measured potential to RHE by using the experimental calibration (roughly once a year or half a year) (Equation 2).

$$\text{Equation 2: } E_{RHE} = E_{applied} - E_{calibrated}$$

$E_{calibrated}$ is an experimentally determined conversion factor, which is measured by cyclic voltammetry.

$E_{calibrated}$ can be estimated using the Pt disk electrode in hydrogen saturated electrolyte (same as the electrolyte used for the designated reaction) at rotation speed of 1600 rpm. Once the hydrogen evolution and oxidation reaction (HER/HOR) happen, it would have two potentials at zero current, and $E_{calibrated}$ is the average value of those two potentials. For example, in Figure A.1, the $E_{calibrated}$ of Ag/AgCl (saturated KCl) in 0.1M KOH is the 0.936 V (average of -0.951 V and -0.921 V), which is slightly off from the calculated value -0.9641 V by equation 1.

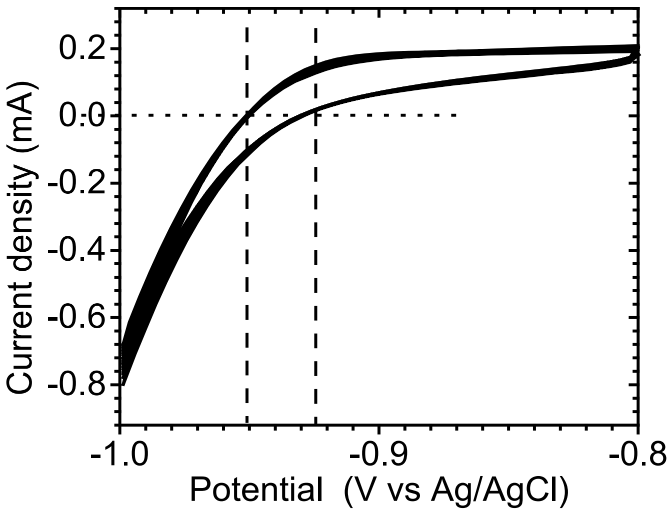

Figure A.1: Cyclic voltammetry of HER/HOR in 0.1M KOH

After convert to the RHE, it is necessary to correct the potential lost caused by the whole system resistance (Equation 3).

Equation 3: $E = E_{RHE} - I_{measured}R$

$I_{measured}$ is the measured current without any process, and the R is the uncompensated resistance determined by electrochemical impedance spectroscopy or the soft-induced resistance estimation program (Figure A.2). E is the final potential we got for the data demonstration.

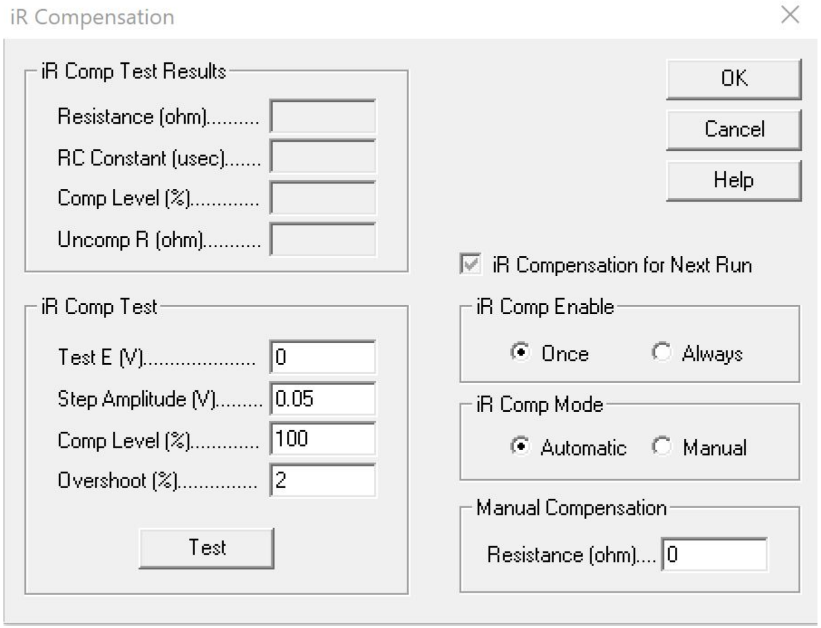

iR Comp Test Results

Resistance (ohm)..........	
RC Constant (usec).......	
Comp Level (%)............	
Uncomp R (ohm)...........	

iR Comp Test

Test E (V)....................	0
Step Amplitude (V).........	0.05
Comp Level (%)............	100
Overshoot (%)..............	2

☑ iR Compensation for Next Run

iR Comp Enable: ● Once ○ Always

iR Comp Mode: ● Automatic ○ Manual

Manual Compensation

Resistance (ohm).... 0

Figure A.2: Built-in resistance estimation function in chi760E

For the current analysis, it should be separated in two different cases for oxygen evolution reaction (OER) and oxygen reduction reaction (ORR). For OER, it only needs to be normalized by the surface area (Equation 4).

$$\text{Equation 4: } I = \frac{I_{measured}}{A}$$

A is the surface area, which be the geometry area of the disk, electrochemically active surface area, or the Brunauer–Emmett–Teller (BET) measured surface area.

For ORR current, it needs to be corrected by the background correction (blue region in Figure A3) to subtract the double layer capacitance current (Equation 5) and followed by the limit current correction (green region in Figure A3) due to the diffusion limit of gas involved reaction (Equation 6).

$$\text{Equation 5: } I_{subtracted} = I_{measured} - I_{background}$$

$$\text{Equation 6: } \frac{1}{I_{subtracted}} = \frac{1}{I_{limit}} + \frac{1}{I_{corrected}}$$

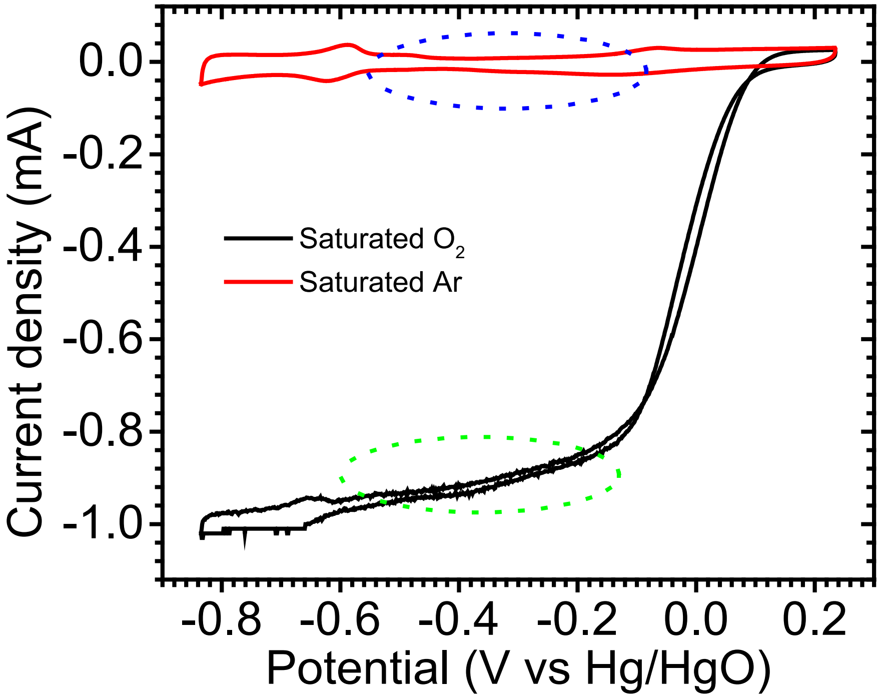

Figure A.3: ORR current in saturated O_2 and background current in saturated Ar, the bule circle is the double layer capacitance current, and the green circle is the limit current

$I_{background}$ is the background current measured in the Ar saturated electrolyte (same as the electrolyte used for the designated reaction) at 0rpm with applied the same potential as ORR. I_{limit} is the maximum current the ORR can achieve at selected rotation speed. The corrected current $I_{corrected}$ was called kinetic current, which can be used in equation to replace $I_{measured}$ in equation 4 to calculate the normalized ORR kinetic current.

XAS Sample Preparation

For general *ex-situ* XAS samples preparation, there are two different methods. One is uniformed dispersed materials on the scotch tape surface, which works for most materials no matter concentrated or diluted. The scotch tape contains some Ti inside, so the Katpon tape would be an alternative for samples containing Ti. Another method is making a pellet, which works best for the concentrated and homogenous samples. It is used to be measured in transmission mode. To make a pellet, we use the Hephaestus XAS software by running the Formulas function to estimate how many samples you need (Figure A4). To get a good transmission data, it is necessary to make sure that the edge step is not exceed 1.5. The edge step calculation is based on Equation 7. For example, when we prepare a CuO pellet, the software will indicate that 4.465 mg CuO is need in 1cm^2 area with 1 absorption length equal to 7.1 micron, and the unit step length at Cu K-edge is 8.3 micron, so the edge step will be around 0.86, which would be good. In addition, the materials would need to be mixed with boron nitride to make a thick pellet. Usually, total 20 or 30 mg materials including both samples and BN to make a good pellet.

$$\text{Equation 6: } Edge\ Step = \frac{Absorption\ length}{Unit\ edge\ step\ length}$$

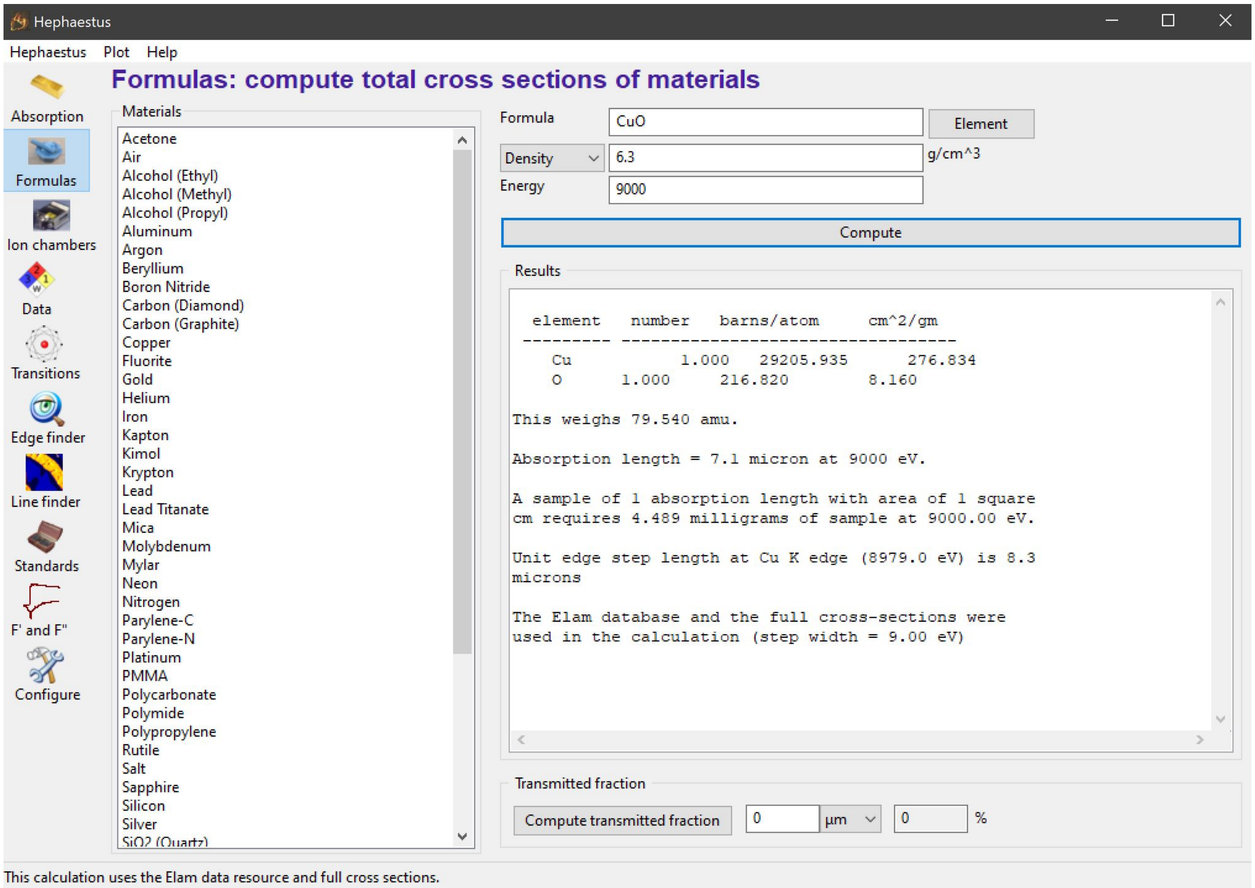

Formula: CuO

Density: 6.3 g/cm^3

Energy: 9000

```
 element   number   barns/atom     cm^2/gm
--------- ----------------------------------
   Cu          1.000   29205.935      276.834
   O      1.000     216.820        8.160

This weighs 79.540 amu.

Absorption length = 7.1 micron at 9000 eV.

A sample of 1 absorption length with area of 1 square
cm requires 4.489 milligrams of sample at 9000.00 eV.

Unit edge step length at Cu K edge (8979.0 eV) is 8.3
microns

The Elam database and the full cross-sections were
used in the calculation (step width = 9.00 eV)
```

Transmitted fraction: 0 µm, 0 %

This calculation uses the Elam data resource and full cross sections.

Figure A.4: Formulas function in Hephaestus to calculate the amount of samples needed for pellet making: example of CuO

For *in-situ* electrochemical XAS samples preparation, 20 mg measured materials will be mixed with 5mg conductive carbon. The mixture was dissolved into in a mixed solution of 3 ml isopropanol (or any other organic solvent), 0.92 ml deionized water, and 0.08 ml 5 wt% Nafion. 0.4 ml ink was deposited on the hydrophobicity carbon paper to form a 1*0.5 cm^2 area. The ink procedure can be changed depends on the materials themselves, but make sure at least 2mg measured materials in 1*0.5 cm^2 area. In addition, the amount should be increased based on the measured elements loading for singly atomic dispersed materials.